UNIVERSITÉ DU QUÉBEC À CHICOUTIMI

MÉMOIRE PRÉSENTÉ À
L'UNIVERSITÉ DU QUÉBEC A CHICOUTIMI
COMME EXIGENCE PARTIELLE
DE LA MAÎTRISE EN INGÉNIERIE

PAR
XIAOJIN LI

A STUDY OF HOT-TEARING DURING SOLIDIFICATION OF ALUMINUM ALLOYS VIA THE ACOUSTIC EMISSION METHOD

MAI 2000

Bibliothèque
Paul-Émile-Boulet

UQAC
Université du Québec
à Chicoutimi

Mise en garde/Advice

Afin de rendre accessible au plus grand nombre le résultat des travaux de recherche menés par ses étudiants gradués et dans l'esprit des règles qui régissent le dépôt et la diffusion des mémoires et thèses produits dans cette Institution, **l'Université du Québec à Chicoutimi (UQAC)** est fière de rendre accessible une version complète et gratuite de cette œuvre.

Motivated by a desire to make the results of its graduate students' research accessible to all, and in accordance with the rules governing the acceptation and diffusion of dissertations and theses in this Institution, the **Université du Québec à Chicoutimi (UQAC)** is proud to make a complete version of this work available at no cost to the reader.

L'auteur conserve néanmoins la propriété du droit d'auteur qui protège ce mémoire ou cette thèse. Ni le mémoire ou la thèse ni des extraits substantiels de ceux-ci ne peuvent être imprimés ou autrement reproduits sans son autorisation.

The author retains ownership of the copyright of this dissertation or thesis. Neither the dissertation or thesis, nor substantial extracts from it, may be printed or otherwise reproduced without the author's permission.

Résumé

La fissuration à chaud entraîne des défauts communs et importants, elle résulte des contraintes en traction qui augmentent lors de la solidification des alliages d'aluminium. Par la technique des émissions acoustiques, il est possible de détecter efficacement le phénomène de fissuration à chaud lors de la solidification du métal.

Dans cet ouvrage, la sensibilité à la fissuration à chaud de l'alliage d'aluminium AA1050 fut étudiée à l'aide d'un moule en forme d'anneau et de la méthode des émissions acoustiques. Lors de la solidification, le signal acoustique est détecté par une sonde piézoélectrique placée près de la zone de fin de solidification, et le changement de température par un thermocouple. Ces mesures ont permis d'établir une relation entre la température du métal et les caractéristiques du signal acoustique. Ainsi, une technique d'analyse du signal acoustique, combinée à une analyse thermique, a été développée.

Des expériences ont été faites pour l'alliage AA1050 avec ou sans affineur de grain afin d'étudier les effets de l'affinage sur la fissuration à chaud. Les résultats démontrent que l'affinage du grain peut diminuer la tendance à la fissuration à chaud de l'alliage AA1050.

Une analyse des surfaces de rupture de tous les échantillons a été réalisée à l'aide du microscope électronique à balayage, les surfaces typiques de fissuration à chaud ont été observées.

Abstract

Hot-tearing is a common and serious casting defect which is caused by tensile stresses developed during solidification of aluminum alloys. The acoustic emission (AE) technique is a really in-situ measurement to study hot-tearing during the solidification of metal.

In this study, the hot-tearing tendency during solidification of AA1050 aluminum alloy with the ring test casting was investigated by the acoustic emission method. AE signals were sampled simultaneously with thermal monitoring by the use of a wave guide and thermocouple in the final freezing zone. These measurements provided a defined time frame for solidification and defect formation events and a time definition for AE signal characterization. A technique of AE signal analysis combined with thermal analysis was developed.

Grain refinement was of an AA1050 aluminum alloy that was dove to compare the effects with and without grain refinement on hot-tearing tendency. The experimental results show that grain refinement can reduce hot-tearing tendency in AA1050 alloy.

The fracture surface analysis was conducted for all samples under a scanning electron microscope. The typical torn surfaces were observed.

Acknowledgments

The author wishes to gratefully acknowledge the financial assistance of Alcan Internatinal Ltd., Natural Sciences and Engineering Research Council of Canada and of the Foundation of the University of Quebec in Chicoutimi.

The author also wishes to express her sincere gratitude to her director Dr. Mihriban Ö. Pekgüleryüz, director of Alcan-UQAC Chair in Solidification and Metallurgy of Aluminum, and co-director Dr. Michel Bouchard, director of the Department of Applied Science, for their excellent teaching and supervision.

The author also wishes to acknowledge Mr. A. B. Innus, Arvida Research and Development Center of Alcan International Ltd., for their active support.

The author is grateful to Mr. Celil Aliravci and Mr. Lin Zhang for their helpful advice and recommendations.

The author also wishes to acknowledge Mr. Gilles Lemire for his helpful and excellent work in the laboratory.

Finally, the author would like to acknowledge the encouragement and cooperation of a number of the colleagues and the friends, and her family.

Table of Contents

List of Figures

List of Tables

Chapter I

Introduction

It is well known that aluminum alloys exhibit a tendency to hot-tearing during casting. A tear in casting results due to a concentration of stresses rendering the cast part unusable and once a tear forms in casting the part cannot be salvaged for further processing. Hot-tearing may cause considerable economic loss and quality problems in the casting industry. Minimization and elimination of hot-tears are therefore very important.

Hot-tearing is a casting defect developed at high temperatures during the cooling of the casting from the pouring temperature. Molten metal in a mold cools and contracts in the liquid state; as the temperature falls, freezing progresses, contraction continues, until the metal has completely frozen. During the later stages of solidification, sufficient solid metal exists so that a coherent network of the solidified metal is developed with the existing liquid metal surrounding the solid interconnected grains. When the contraction of the solidifying castings is excessively restrained by the strength of mold or cores, the tears, (i.e., separation of solid grains) may occur. Hot-tearing occurs at near-solidus temperatures at which point solidification is essentially complete except for liquid films surrounding the dendrites. When films are thinner and the contraction stresses in the films increase greatly, interdendritic fracture or hot-tearing occurs. Hence, the tears propagate along the dendrite

or grain boundaries.

Because hot-tearing defects are caused by a number of complex inter-related variables, evaluation of the principal factors is very difficult. A few theories have been developed mainly to address simple binary alloy systems. However, these fail to describe this complex phenomenon especially in multicomponent alloys. Over the past several years, "**Acoustic Emission**", an effective method to measure and study hot-tearing in-situ during solidification of metals has been developed. This method may help investigate the factors influencing hot-tearing in complex alloy systems.

We know that when a solid is subjected to stress at certain levels, discrete acoustic wave packets are generated which can be detected. The phenomenon of sound generation in materials under stress is termed Acoustic Emission. Listening to Acoustic Emission (AE) is a method for observing rapid dynamic material processes. With the AE technique, we can detect plastic deformation and crack propagation in any material in real-time.

In the summer of 1996, in the Alcan-UQAC Chair in Solidification and Metallurgy of Aluminum, a study was initiated that used AE to study hot-tearing in solidifying alloy casting. A series of AE signals were obtained by using a new AE equipment (MISTRAS-2001) during solidification of aluminum alloys. Through these studies, the use of AE and the experimental method was proven to be feasible.

The purpose of the present study is: (1) to develop and perfect the test method for the in-situ detection of hot-tearing in solidifying aluminum alloys by the AE technique; (2) to find an optimum method that both the thermal monitoring system and AE signals detecting system can be used at the same time during the solidification process, to distinguish a hot-tearing event from other solidification events by superposition of the AE signals and the cooling/solidification curves; (3) to investigate the hot-tearing tendency in AA1050 alloy and the effects of grain-refining.

This thesis consists of four principal sections: the first deals with the theoretical background and literature review concerning hot-tearing and the acoustic emission technique; the second deals with a detailed narrative of experimental method, set-up and procedure; the third section gives an exhaustive discussion involving experimental results and analysis; the last chapter is the conclusion of the present research, and recommendations for future work.

Chapter II

Theoretical Background and Literature Review

2.1 Description of Hot-Tearing

Hot-Tearing is one of the most common and serious defects encountered in castings. The defect is easily recognized from one or more of a number of characteristics as Table 2.1 shows:

Table 2-1 Summary of hot-tearing description

Hot-tearing	Characteristics
the visual appearance	● a ragged, branching crack; ● the main tear and its numerous minor offshoots generally following intergranular paths.
the fracture surface (as seen via micrographs)	● reveals a free dendritic morphology
the time	● when the material is still somewhat incoherent and liquid metal is present; ● the material has minimal strength due to the presence of the liquid metal ● close to completion of solidification
the location	● often at a hot spot, ● where contraction strain from adjoining extensive thinner sections may be concentrated
the temperature	● at or just above solidus temperatures

Fig. 2.1 shows the typical microstructure of a hot-tear showing the multi-branched intergranular cracks [1]. And Fig. 2.2 shows a scanning electron microscope view of the surface of a hot-tearing in AA1050 alloy (Test 1003 of this study) revealing a free dendritic morphology.

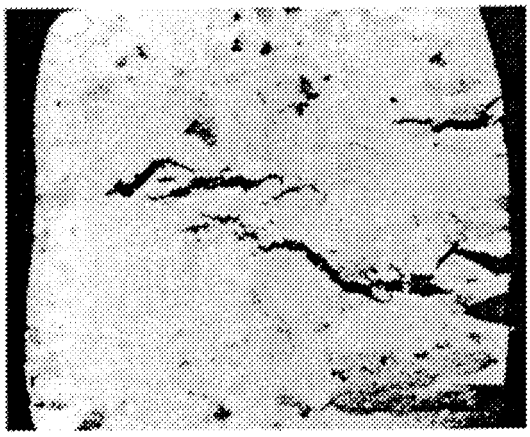

Fig. 2.1 The typical microstructure of a hot-tear showing the multi-branched inter-granular cracks [1].

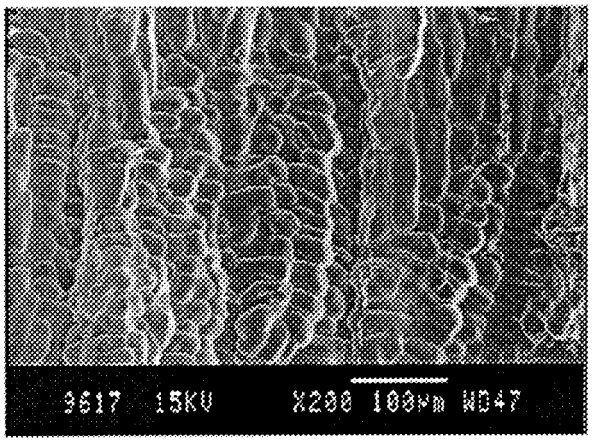

Fig. 2.2 A scanning electron microscope view of the surface of a hot-tear in AA1050 alloy revealing a free dendritic morphology.

It is an accepted fact that hot tears occur when the contraction of the solidifying castings is excessively restrained by the mold or cores and that the tears occur in weak areas where the strain resulting from the contraction is concentrated. These weak areas are localized hot spots such as gate and riser contacts, re-entrant angles or abrupt enlargements in the sections of castings.

Most of the early studies on hot-tearing led to empirical results which identified a

temperature interval around a solidus where hot-tearing is likely to occur. Hot-tearing was identified as a casting defect developed at high temperatures during cooling of the casting from the pouring temperature [2]. It was established that hot tearing occurs at near solidus temperatures at which state solidification is essentially complete except for liquid films surrounding the grains [3]. Fig. 2.3 illustrates that hot-tearing occurs at what is called an "effective crystallization region" of the alloy.

Singer et al [4] conducted elevated temperature tensile tests on several aluminum-silicon alloys, and found that the alloys possessed finite strengths but no ductility. Tensile strengths were taken at the upper limits of a "hot shortness range", lower limits were the solidus temperatures (Fig. 2.4). Pellini and his co-workers [5] used a radiographic method to obtain the data of hot-tearing temperature range in steels as related to the Fe-C phase diagram, shown in Fig. 2.5.

2.2 Theories of Hot-Tearing

2.2.1 Strain Theory

It was Pellini [5] in 1952 who drew attention to the strain concentration which could occur at a hot spot in a casting. If the length of the casting is L, and if it has a coefficient of thermal expansion α, during its cooling by ΔT from the liquidus temperature it will contract by an amount $\alpha \Delta T L$. If all of this contraction is concentrated

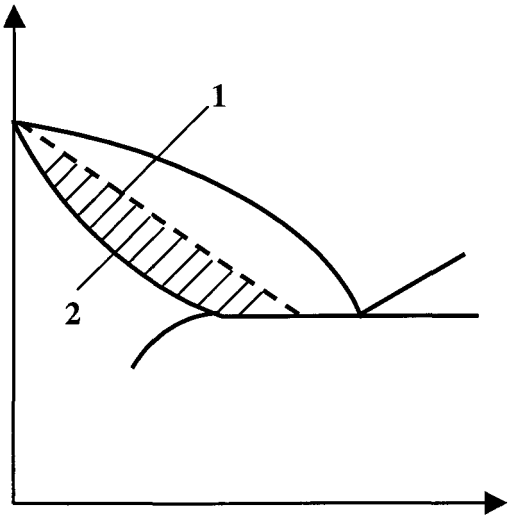

Fig. 2.3 a) Effective crystallization region for alloy: 1 – upper limits of the effective crystallization region; 2 – lower limits of the effective crystallization region.

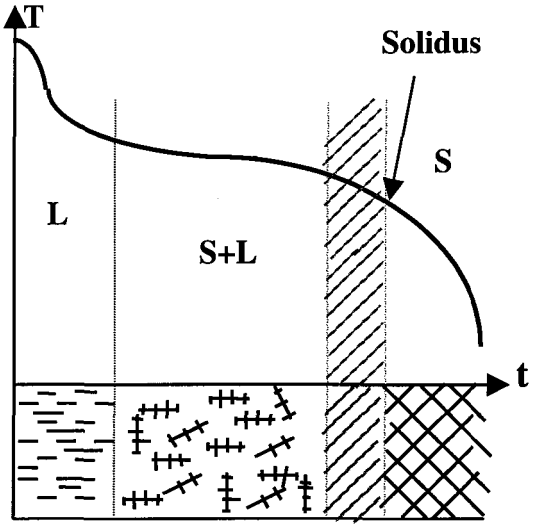

Fig. 2.3 b) The cooling curve and solidification states.

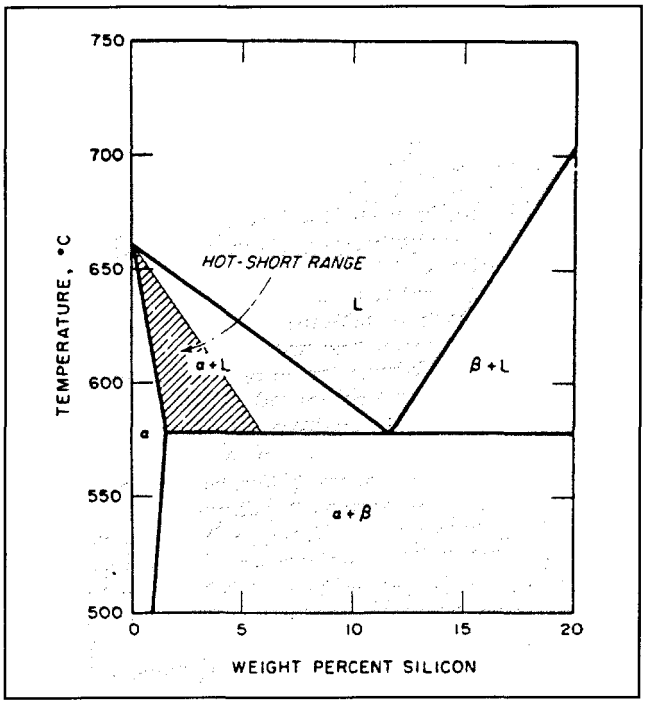

Fig. 2.4 Range of hot shortness for aluminum – silicon system.

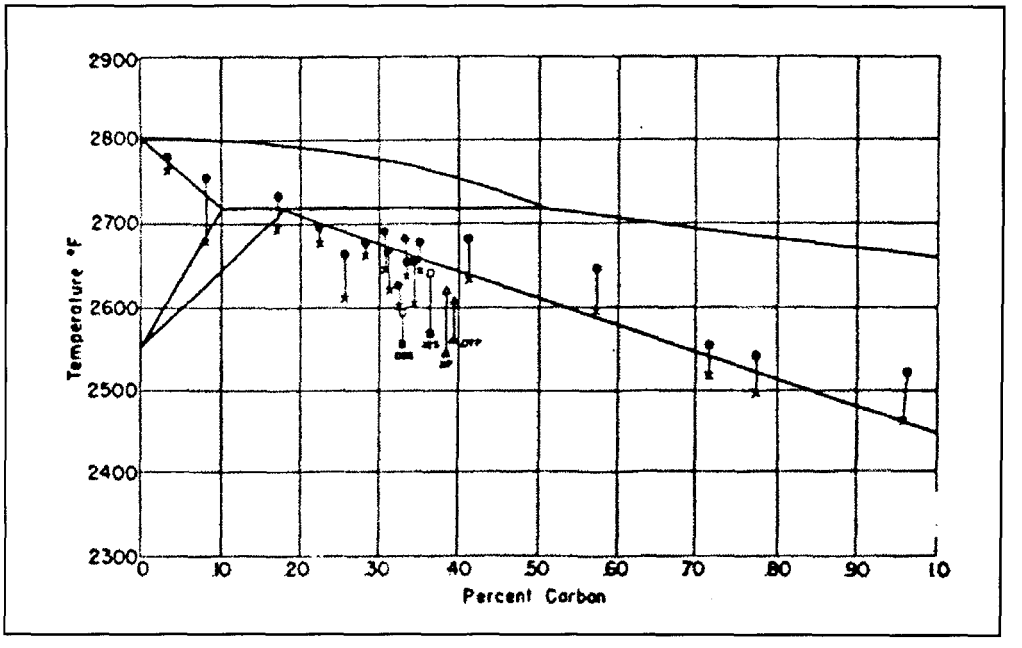

Fig. 2.5 Summary data indicating hot-tearing temperature range in steels as related to the Fe-C constitution diagram [5].

in a hot spot of length l, then the strain in the hot spot is given by:

$$\varepsilon = \alpha \, \Delta TL / l \qquad \textbf{(2.1)}$$

In addition to the consideration of the amount of strain concentrated into the hot spot, it is also necessary to consider how many grain boundaries the hot spot will contain. If the grain size is coarse, the hot spot may contain only one boundary, with almost certain disastrous consequences, because all the strain will be concentrated in that one liquid film. If the hot spot contains fine grains, and thus many boundaries, then the strain is more widely distributed. We may quantify this, since the number of grains in the length l of the

hot spot is *l/a* for grains of diameter *a*. Hence if we divide the strain in the hot spot (Equation 2.1) by the number of boundaries in it, then the strain per boundary can be obtained as:

$$\varepsilon_b = \alpha \Delta T L a / l^2 \qquad \textbf{(2.2)}$$

It is clear that reduced temperature differences, smaller overall lengths between hot spots, and finer grain size all help to reduce the strain which is trying to open up the individual grain boundaries. However, Equation 2.2 reveals for the first time that the most important parameter is the length *l* of the hot spot; as this is halved, the grain boundary strain is increased four times.

One of the early theories of hot-tearing was the strain theory. The strain theory of hot-tearing was developed based on a concept of liquid films existing at grain boundaries at temperatures above or in the region of the solidus. When the metal is in the liquid-film stage, the films first developed as the metal falls to a temperature within the liquid-film region are relatively thick and capable of absorbing strains imposed by the contraction of any part of the casting that may be solid. At a later stage the films are thinner and the strain concentration in the films increases greatly; this is when hot-tearing is likely to occur. Fig. 2.6 illustrates schematically the mechanism of film-stage tearing.

The strain theory provides a generalized explanation of the mechanism of hot-tearing in terms of the time-rate of the extension developed in the liquid film regions. Fig. 2.7

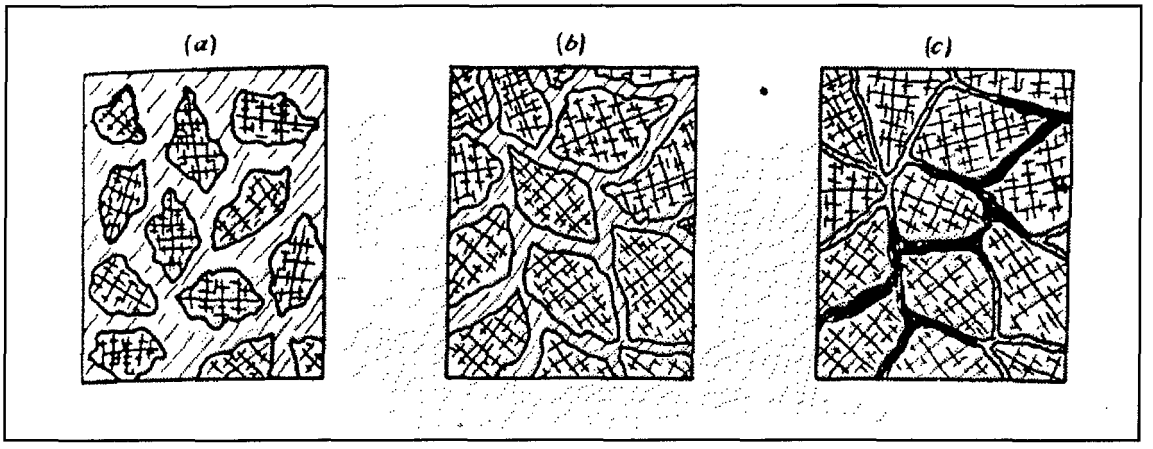

Fig. 2.6 Mechanism of film-stage tearing [1]. Schematic representation of the solidification of a hot-spot under conditions of hindered contraction.

a) Solid nuclei together with considerable liquid metal. Hot-tearing is not possible at this stage;
b) Crystals separated by thick liquid films. The stage when the possibility of a "build-up" of strain in the hot-spot is approaching.
c) Stage just before complete solidification. Crystals are separated by thin liquid films. The developed strain concentration has been sufficient to cause hot-tearing.

illustrates the effects of strain rate and time of film life to hot-tearing by Pellini [5]. The strain accumulated within the hot spot is a function of the strain rate and time duration in which the metal passed through the film stage. From figure 2.7, it can be seen that the amount and rate of strain concentration in the liquid film determines the development of hot-tearing in castings. The rate of extension of the film regions may vary widely due to a number of factors including cooling rate and length of regions undergoing contraction and width of the hot spot undergoing contraction. The longer the region undergoing contraction and faster its cooling, the greater the contraction developed for each unit of time. The narrower the hot spot the greater will be the unit extension developed in unit time for a given rate of contraction of the colder regions.

Fig. 2.8 illustrates the nature of strain distributions (extension and contraction)

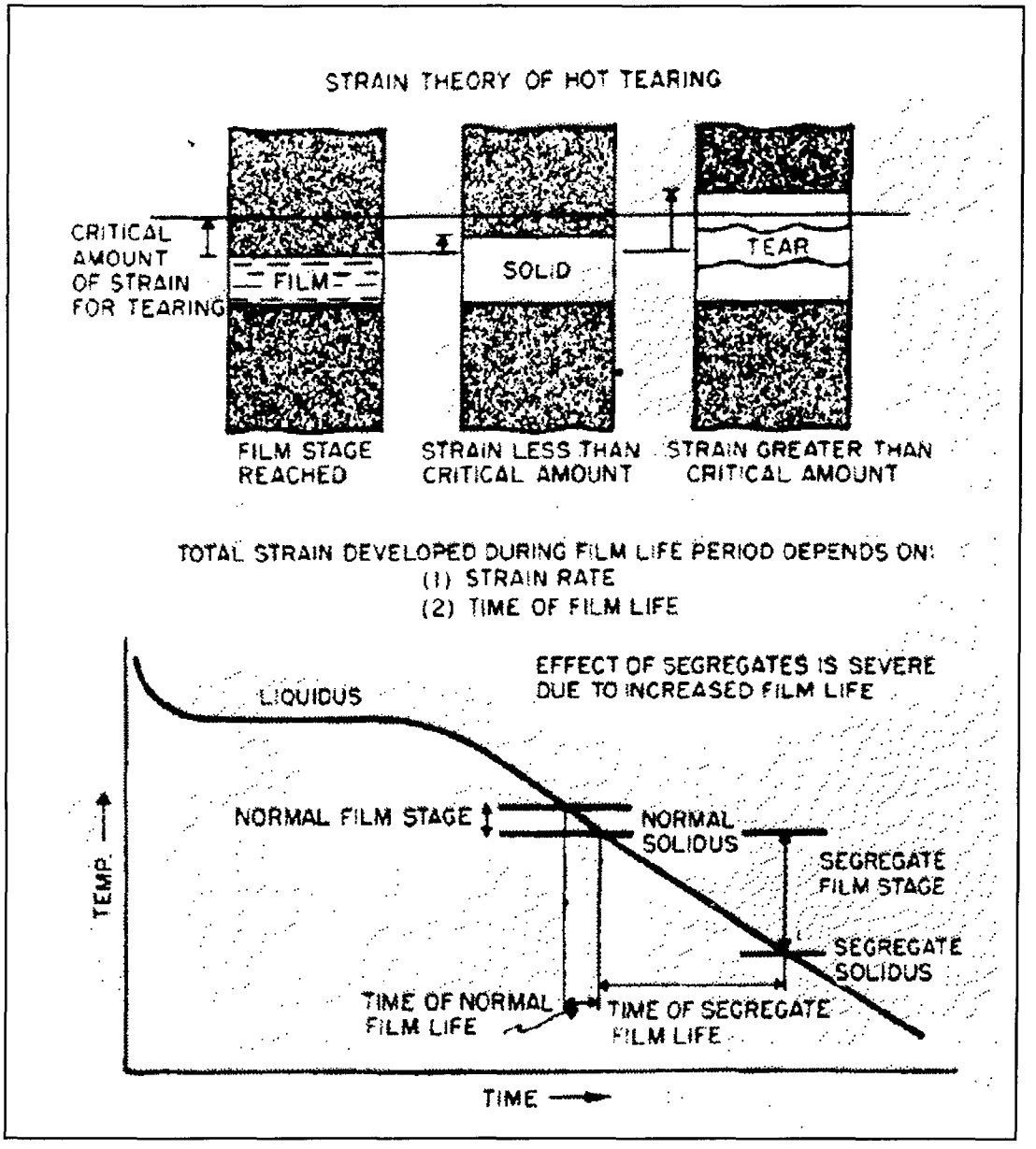

Fig. 2.7 Illustrating basic concepts of the process by which total amount and rate of strain (extension imposed on hot spot zone) concentrated to the liquid films determines the development of hot-tearing in casting [5].

which exist during various stages of solidification in a casting system containing a hot spot [4]. While the metal is in the mushy condition which exists at temperatures considerably above the solidus (Fig. 2.8 A), the extension of the hot zone is distributed relatively

uniformly since the interdendritic liquid areas are relatively wide and mass flow of the mushy mass results. The low unit strains are insufficient to cause a separation. Fig. 2.8 B illustrates the high value of unit strains developed in these regions at this time at the liquid-film stage which comes later. At this time certain additional factors need to be considered. The width of the overall hot zone in a casting must be considered as a determining factor if tearing will occur. If the hot zone is narrow and only a few films exist, each film must accommodate a great amount of extension; a wide overall hot zone will have many films and the extension per film will be less. However, the high unit strains may be sufficient to cause separation. In Fig. 2.8 C, hot zone is depicted in solid stage. Now, the strains in the hot spot area are distributed in a relatively uniform fashion throughout the coherent and ductile solid metal. Stresses will build up in the casting as cooling continues until the low yield point of the hot metal is exceeded after which time creep flow occurs. Tears which occur during the critical film stage enlarge primarily in width as the casting contracts further on cooling below the solidus temperature due to stressing across the notch area created by one tear. Enlargement of tears in a true hot tearing fashion does not occur at temperatures below the true solidus. The enlargement in width is due to plastic yielding at the end points of the tear.

2.2.2 Tear Initiation and Growth

Until 1981, it was assumed that the tear was a simple growth phenomenon; the nucleation of a tear was not widely appreciated as a problem. In order to have insight into the problem of tear initiation, Hunt and Durrans [6] constructed a transparent cell on a

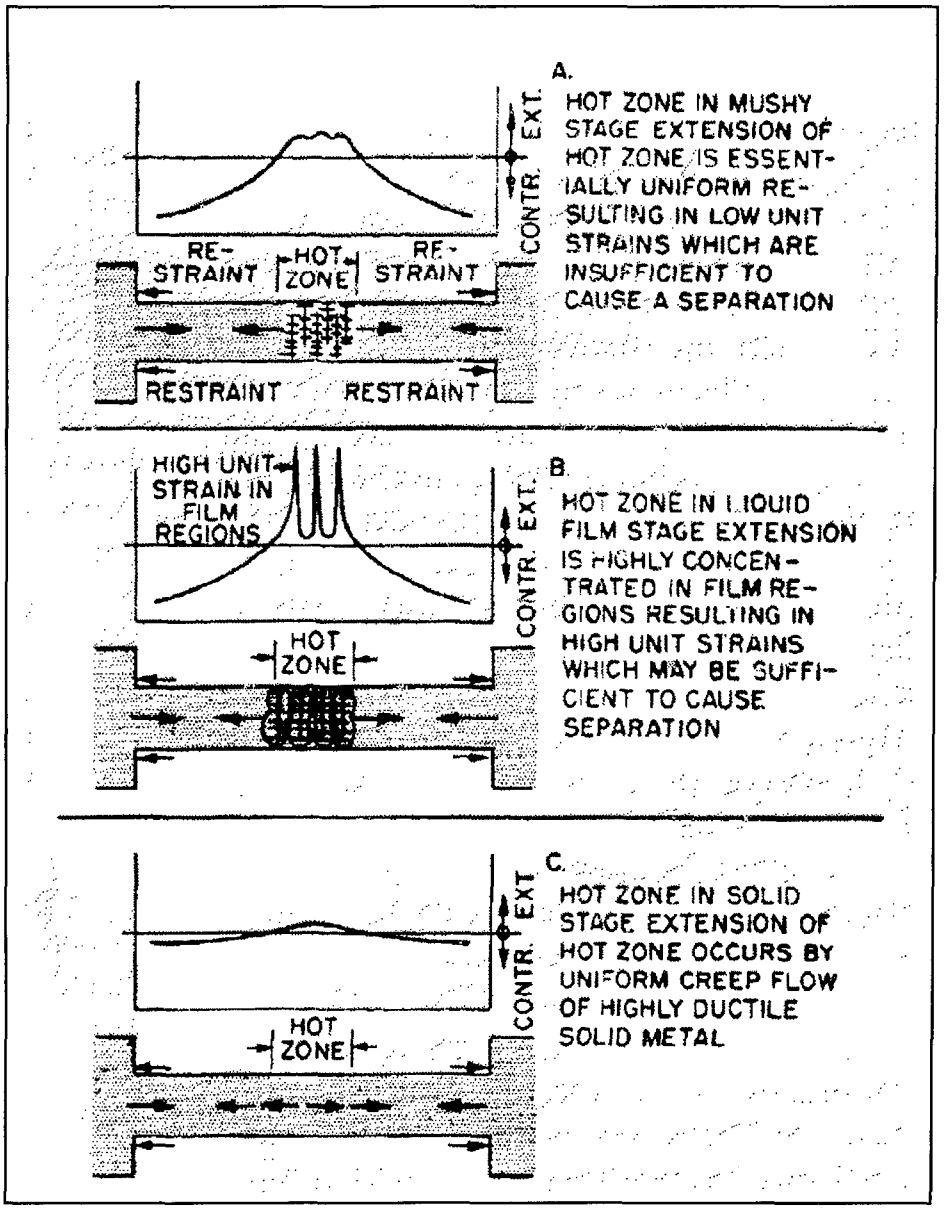

Fig. 2.8 Illustrating nature of strain distributions (extension and contraction) which exist during various stages of solidification in a casting system containing a hot spot [5].

microscope slide, which enabled them to study the solidification of a transparent analogue of a metal. The cell was shaped to provide a sharp corner around which the solidifying material could be stretched. The idea was to watch the formation of the hot-tearing at the sharp corner. The outcome of this study was that no matter how much the material was stretched against the corner, it was not possible to start a hot tear in clean material: the

freezing mixture continuing to stretch indefinitely, the dendrites continuing simply to move about and rearrange themselves. However, in the presence of a small inclusion or bubble near the corner, a tear opened up immediately, spreading away from the corner. In their system, hot-tearing was demonstrated to be a process dependent on nucleation. In the absence of a nucleus (e.g. inclusion) a hot tear cannot occur. This fact explains much of the scattered nature of the results of hot-tearing work in castings: apparently identical conditions do not give identical tears, or at times even any tears at all.

However, even at the surface of a casting in an alloy which does not form a surface film, the initiation of a tear may not be straightforward. It is likely that the tear will only be able to start at grain boundaries, not within grains. This is because the dendrites composing the grain itself will be interconnected, all having grown from a single nucleation site. Dendrites from neighboring grains will, however, have no such links, and in fact the growing together dendrite arms has not been observed in studies of the freezing of transparent models. The arms are seen to approach, but final contact seems to be prevented by the flow of residual liquid through the gap. Thus if a grain boundary is not sited conveniently at a hot spot where strain is concentrated, then a tear will be difficult to start. This will be more common in large-grained equiaxed casting, as suggested by Warrington and Mccartney (1989) [7].

Even if a grain boundary is favorably sited, it may open along its length. However, on meeting the next grain (which will have some other orientation) further progress may be restrained. Thus a tear may be limited to the depth of a single grain. For the case of

columnar grains, the boundaries at right angles to the tensile stress direction will provide conditions for easy initiation of a tear along such favorably oriented grain boundaries. For fine-grained equiaxed material where the grain diameter can be as small as 0.1-0.2 mm or even smaller, the dispersion of the problem as a large number of fine tears, all one grain deep is effectively to say that the problem might be solved.

Nevertheless it is fair to emphasize that the problem of the nucleation of tears has been very much overlooked in most previous studies. Nucleation difficulties would help to explain much of the apparent scatter in the experimental observations. By chance positioning of a suitable grain boundary containing, by chance, a suitable nucleus, such as a folded oxide film, would allow a tear to open easily. By chance, its absence from the hot spot would allow the casting to freeze without defect; the hot spot would simply deform, elongating to accommodate the imposed strain.

On the studies of tear growth, the easy growth in columnar grains where the direction of tensile stress is at right angles to the grain boundaries was mentioned. Spittle and Cushway [8] observed that the linear boundary formed between columnar crystals growing together from two different directions was an especially easy growth route for a spreading tear.

2.2.3 Hot-Tearing Criteria (Cracking Susceptibility Coefficient)

Even so, tensile stress has been considered to be one of the most important parameters in fracture [9]. Mechanisms of failure in solid-liquid systems, indicate the

existence of a critical tensile stress for the nucleation of holes and growth of cavities. It is likely that both shear and tensile stresses play a role since there is evidence that localized plastic flow by shear is required to initiate cracks which are then propagated by tensile stresses [9]. In solid-liquid mixtures, for example, considerable movement of solid due to shear may be required before sufficient solid-solid contacts develop to raise the tensile stresses up to a critical level.

It is known that conditions which lead to dendrite separation or fracture can be represented using mechanical terms alone; this is not sufficient to describe hot-tearing susceptibility. Inter-dendritic fluid flow characteristics determine the ability of the liquid to "fill in" incipient hot tears and heal hot-tears dynamically.

When feeding is adequate, liquid may "fill in" incipient hot tears. This leaves behind a channel of macro-segregation instead of an open hot tear. Criteria have been proposed to predict the back filling. Feurer's hot tearing criterion [10] states that if shrinkage rate exceeds feeding rate then it is possible to develop open hot tears. The shrinkage rate (Vs) is defined as,

$$\mathbf{Vs = (1/V)\ dv/dt\ = -\ (1/\rho)\ \ (d\rho/dt)\ (cm^3/sec)/cm^3} \qquad \mathbf{(2.3)}$$

where,

$\mathbf{V}$ = volume of solidifying element with constant mass.

ρ = average density of the element

= $\rho_L f_L + \rho_S f_S$

$\mathbf{f_S}$, $\mathbf{f_L}$ = volume fraction of solid and liquid phases respectively

The shrinkage rate for a given alloy system can be derived from the above equation, with the alloy and casting parameters taken into account.

Feeding is assumed to take place through the inter-dendritic channels. Based upon theories of fluid flow through porous media, an expression for the feeding rate is derived as:

$$\mathbf{V_F = (f_L^2\, d^2\, P_S) / (24\, \pi\, C^3\, \mu\, L^2)} \qquad \textbf{(2.4)}$$

Where,

d = secondaty dendrite arm spacing

$\mathbf{P_S}$ = effective feeding pressure,

L, C = length and tortuosity of the dendritic network,

μ = viscosity of the liquid

Thus, according to this criterion, hot tears form if V_S exceeds V_F. Correlation between this criterion and experimental results on Al-Si and Al-Cu-Fe alloys were found to be good [11].

Clyne and Davies [12] have proposed an index of hot-tearing or **cracking – susceptibility coefficient (CSC)**, defined as,

$$CSC = t_s / t_f \qquad \textbf{(2.5)}$$

Where t_f is the time available for stress-relaxation processes such as liquid and mass flow (feeding time available), and t_s is the vulnerable time period when cracks can propagate between grains (inter-dendritic separation time available).

Inter-dendritic separation is assumed to occur when liquid content is between 1-10% and flow is restricted due to narrow inter-dendritic channels. It is further assumed that if liquid content is between 10-60%, flow is possible for feeding incipient tears. Variation of the cracking susceptibility, as calculated by the above method, compared well with experimental observations on Al-Mg and Al-Si alloys. Comparisons were, however, not good for Al-Zn alloys.

It has been felt in the research community that a hot-tearing criterion should in fact take into account both mechanical and fluid flow factors. To combine the cracking-susceptibility coefficient with Equation 2.2 derived above for strain per boundary in the hot spot, the modified CSC_b is:

$$CSC_b = \alpha \Delta t \, L \, a \, t_s / l^2 \, t_f \qquad (2.6)$$

Where,

l = the length of the hot spot,

L = the length of the casting,

α = coefficient of thermal expansion,

Δt = time of cooling from the liquidus temperature

a = diameter of grain

2.3 Techniques of Hot-Tearing Investigations

Because hot-tearing defects are caused by a number of complex inter-related

variables, evaluation of the principal factors is very difficult. A number of researchers have adopted different techniques to study hot-tearing; some researchers monitored the stresses developed in the casting during solidification [13, 14]; some used a radiographic method to obtain a visual image of tear initiation in the steel casting during solidification [4]; and some monitored the extent of deformation of the hot tear zone and the total contraction [15]. In these experiments, the contraction of the test casting was restrained by special a mold design. This could cause a visible tear in the test casting.

There are two groups of molds commonly used to detect hot-tearing. The various I-beam (sometimes known as "dog bone") tests and the ring mold test. These various molds have been used to assess hot-tearing susceptibility of different alloys.

The I-beam has many variants. One of the most common is the arrangement of various lengths of rod castings from a single runner. Each of the rods has a T-shaped end to provide a restriction to its contraction. When the metal is poured, the contraction of the rods will take place with various degrees of constraint, those rods greater than a critical length failing by tearing at the hot spot, which is located at the joint between the runner and the rod. From such a test, therefore, only one result is obtained, and its accuracy is limited by the increments by which the rods increase in length. Other sorts of I-beam tests yield a potentially more discriminating result by measuring the lengths of cracks in the hot-spot region. However, even in this case the actual test volume of material is limited and the stress and strain distribution in the hot spot is far from uniform.

The Ring Casting (RC) mold is normally carried out using a die. It consists of two parts: concentric core and an outer ring mold with an annular space between them. The molten metal is poured into the annular space between the outer ring mold and the core. As the metal cools, it contracts onto the inner steel core. The core also expands slightly as it heats up. The resulting constraint on the casting is severe, opening up transverse tears all around the ring in a susceptible alloy during the solidification process. The RC mold is one of the most simple and classic hot-tearing test molds developed fifty years ago by Singer and Jennings [16]. The hot-tearing sensitivity in a RC test is assessed by measuring the total length of cracks on all surfaces of the rings, and it is a function of the processing variables such as composition, mold and pouring temperatures. It is known that the RC mold was adopted for various research projects over the years for ferrous or non-ferrous alloys.

There are other tests using visual techniques to detect hot-tearing which are listed below:

- Flanged Bar Test [17];
- Cylindrical Bar Casting Test [18];
- Ball - Bar Casting Test [19];
- Chilled - Casting Test [20];
- "U" Casting [21].

Because the inter-surface hot-tearing cannot be observed using visual methods, over

the past years, a few physical methods have been used to investigate hot-tearing susceptibility. These are:

- The Electrical Resistance Test; and
- The Acoustic Emission Technique.

Since the 1970s, an effective method has been under development to measure and study hot-tearing in-situ during the solidification of metal. It is the "Acoustic Emission" method. This method may help investigate the factors influencing hot-tearing in complex alloy systems. Plastic deformation and crack propagation in any material is associated with the generation of acoustic waves in the ultrasonic range. In the acoustic emission technique, these waves are detected in real time. Hence the dynamic crack growth condition could be monitored by this technique.

2.4 Acoustic Emission Technique

2.4.1 Introduction

It is well known that when a solid is subjected to stress at certain levels, discrete acoustic wave packets are generated which can be detected. The phenomenon of sound generation in materials under stress is termed Acoustic Emission (AE). AE are the high frequency stress waves generated by the rapid release of energy that occurs within a material during crack growth, plastic deformation, or phase transformation. AE is a method for observing rapid dynamic material processes with elastic waves.

Early observations of acoustic emission in metals were made by tinsmiths who noted

"tin cry", or twinning, during deformation of tin (twinning deformations in general are active generators of acoustic emissions). Audible sounds or clicks noted during heat treatment of steel were related to martensitic transformations. In fact, later studies showed that martensitic transformations in general are prolific sources of acoustic emission. Joseph Kaiser and his coworkers [22] in Germany in the early 1950s are generally credited for initiating the present effort in acoustic emission. Kaiser was the first to use electronic instrumentation to detect audible sounds produced by metals during deformation. He reported that all metals examined, including zinc, steel, aluminum, copper, and lead, exhibited the emission phenomena. Kaiser also observed that acoustic emission activity was irreversible, that is, acoustic emissions were not generated during the reloading of material until the stress exceeded its previous level. The irreversible phenomenon has come to be known as the «**Kaiser effect**» and has proven to be very useful in acoustic emission studies.

Several years after Kaiser's work, investigators in the United States became interested in acoustic emission phenomena. Schofield [23] and Tatro [24] initiated research in the mid-1950s and did much to improve the instrumentation and to clarify the sources of acoustic emission. They found that emissions from metals were primarily due to dislocation motion accompanying plastic deformation [25, 26, 27, 28] rather than being entirely due to grain boundary sliding as proposed by Kaiser.

In the decade of the 1960s, many engineers and scientists became interested in acoustic emission and utilized this technique in studies relating to materials research,

materials characterization and evaluation, nondestructive testing [29], and structural evaluation [30].

In the 1970s, extensive improvement in instrumentation made possible many advances in acoustic emission technology. Acoustic emission technology was mainly used in material research and structural integrity inspection.

Application of Acoustic Emission in Materials Research. Acoustic emission is well suited to studies of deformation in materials. In addition to the work on single crystals, considerable work has been conducted on polycrystalline tension specimens [31, 32, 33, 34]. Acoustic emissions generated during phase transformations have also been studied [35], and martensitic transformations were found to be particularly copious sources of acoustic emissions. Materials studies have included work in fracture mechanics on flawed specimens. Acoustic emission has been utilized in the detection of "pop-in" [36, 37] during rising load fracture toughness tests.

Plastic deformation, which results in acoustic emission, occurs at crack tips and other highly stressed regions when a material is loaded; hence, acoustic techniques have been used advantageously for flaw detection. Acoustic emission has been used to study growing cracks, such as those occurring during hydrogen embrittlement [38, 39], stress corrosion cracking [40], and low cycle fatigue [41]. Fatigue crack growth produced by fluctuating loads can be detected by continuous monitoring of acoustic emission. Hartbower et al [40] investigated the acoustic emission during low cycle fatigue from D6Ac steel with various

heat treatments and reported that it was possible to detect the growth of fatigue cracks by continuous monitoring. Also, the amount of crack growth per cycle can be directly determined from acoustic emission data.

Application of Acoustic Emission Technology in Structural Integrity. The presence of cracks in structures alters the load at which plastic deformation begins, thus altering the acoustic emission. This has been used in assessing structural integrity [42, 43, 44, 45,] of machined parts by acoustic monitoring of the initial proof test. The acoustic emission record can determine if flaws are present and assess their severity. Acoustic emissions for assessment of structural integrity have been applied to a wide variety of structures, including pressure vessels for nuclear and petroleum industries [38-40], rocket motor cases [37], and bridges, buildings, and wooden beams [46]. Techniques are also available to detect, during service, the degradation of structural integrity due to subcritical flaw growth. In some cases, this can be accomplished by continuous monitoring to detect the emissions produced as the crack extends under constant load; work on hydrogen embrittlement and stress corrosion cracking has illustrated the feasibility of using acoustic emission for the detection of growing cracks. Periodical overload while monitoring for acoustic emission is another technique devised to assess growing cracks.

In the 1980s, the computer became a basic component for both instrumentation and data analysis, and today it has sparked a resurgence of opportunities for research and development. Today, waveform-based acoustic emission analysis has become commonplace and there is a shift in acoustic emission activities with more emphasis on

applications than on research. With the acoustic emission technique, we can detect plastic deformation and crack propagation in any material in real-time.

2.4.2 Acoustic Emission Sources

Studies of the sources of acoustic emission should lead to applications of acoustic emission techniques in dislocation dynamics and deformation of materials. Fig. 2.9 illustrates the primitive wave released at the acoustic emission source. The displacement waveform is basically a steplike function corresponding to the permanent change associated with the source process. The corresponding velocity and stress waveforms are basically pulse-like and the width and height of the primitive pulse depend on the dynamics of the source process. Source processes such as microscopic crack jumps and

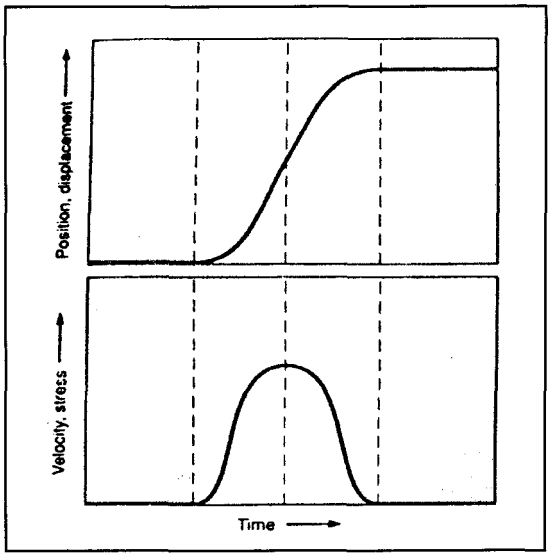

Fig. 2.9. Primitive acoustic emission wave released at a source. The primitive Wave is essentially stress pulse coresponding to a permanent displacement of the material.

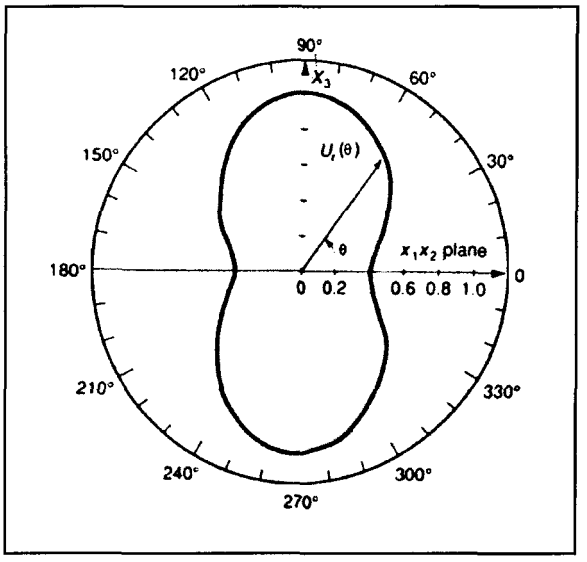

Fig. 2.10. Angular dependence of acoustic emission radiated from a growing microcrack. Most of the energy is directed in the 90 and 270° direction, perpendicular to the crack surfaces.

precipitate fractures are often completed in a few microseconds or fractions of a microsecond. So the primitive pulse has a correspondingly short duration. The amplitude and energy of the primitive pulse vary over an enormous range from submicroscopic dislocation movements to gross crack jumps.

The primitive wave radiates from the source in all directions, often having a strong directionality depending on the nature of the source process, as shown in Fig. 2.10. Most of the energy is directed in the 90° and 270° directions, perpendicular to the crack surface.

Acoustic emissions are only generated during transient changes in the local stress and strain fields within a material. Such changes accompany deformation, fracture, or phase-transformation processes. Mechanisms that produce acoustic emission in metals include the movement and multiplication of dislocations; slip; twinning; fracture; inclusions, and surface layers; some corrosion processes; microcrack jumps; and frictional processes during crack closure and opening.

The amount of acoustic emission energy released depends primarily on the size and speed of the local deformation process. The formation and movement of a single dislocation does produce an acoustic emission stress wave, but it is not a large enough process to be detected in isolation. However, when millions of dislocations are forming and moving at the same time during yielding of a tensile specimen, the individual stress waves overlap and superimpose to give a detectable result. The result is a continuous excitation of the specimen and sensor that is detectable as soon as the voltage it produces

becomes comparable with the background noise. The higher the strain rate and the larger the specimen, the larger this signal becomes.

Wadley et al.[47] proposed a model for acoustic emission sources which can be broadly classified into two general types. One type considers the source as a generator of elastic radiation energy and uses macroscopic parameters such as bulk stress and strain to obtain a static solution to the problem. This approach ignores how the source relaxation is related to the deformation process itself. The other, and in many ways more difficult, approach involves using the local time-varying stress and strain fields in the vicinity of the source to calculate the dynamic changes associated with operation of the source.

Static-source models. This approach considers an energy partition process at the source as explained by Birchon [48] (Fig. 2.11). The stored energy, available to a source for generating elastic waves, is not totally converted into acoustic emission radiation: some is converted into surface energy (owing to the creation of new crack faces and/or surface slip steps), some into the energy of a dislocation network, and some into heat as a result of plastic deformation. Only a fraction of the available energy is radiated as transient elastic waves which constitute acoustic emission, and which, ultimately, are converted to thermal energy. If the energy of the acoustic emission could be measured and the partition function determined, then it might be possible to estimate the energy of the source event. But it is rather difficult in practice.

Dynamic-source models. Pollock [49] has developed a more dynamic-source model based

on a mass supported between two springs. When the spring constant of one spring was

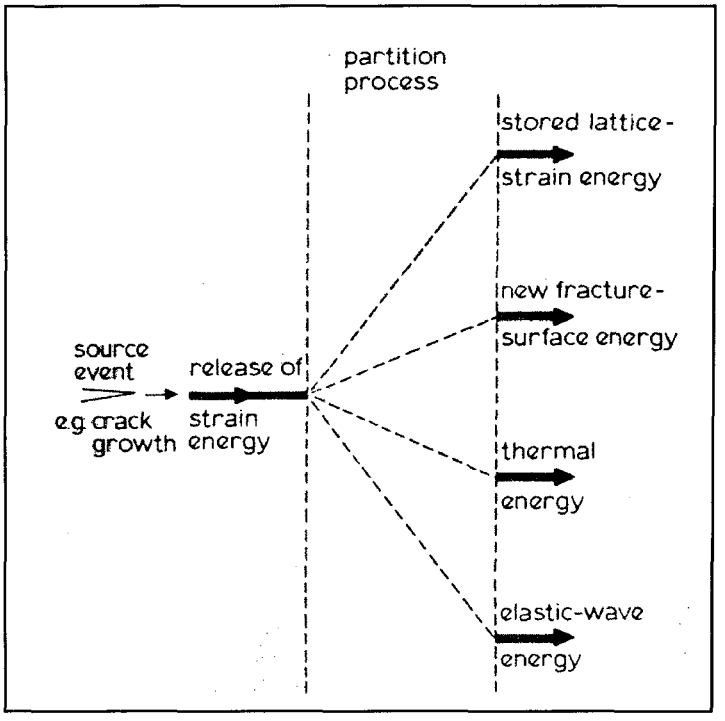

Fig. 2.11. Illustration of partition of elastic energy during a crack-growth event: stored elastic-strain energy is released in the form of new surface energy, thermal energy, and the transient elastic waveform called acoustic emission (Birchon).

instantaneously changed, the resulting shift to the new equilibrium was considered as the emission generating process. While his model serves to emphasize that acoustic emissions are generated by relaxation processes, it is much too simplified for modeling the source functions for deformation or fracture processes in metals. A more fundamental approach to modeling dislocation sources of acoustic emission has been attempted by Kiesewetter and Schiller [50] and by Mirabile, [51] who apply the work of Eshelby [52] on dislocation motion. Eshelby treats the radiation from moving dislocations in an analogous manner to the electromagnetic radiation from an accelerating electric charge, and calculates the

acoustic energy radiated from an oscillating kink into the surrounding medium as a function of dislocation parameters. Kiesewetter and Schiller apply the result to the Frank-Read source, for observations. However, it is not clear how justified they are in their simplifying assumptions about oscillation frequency in this particular application.

A recent approach is also worthy of note. The simplest model [53] for an acoustic emission source is the point-force monopole, whose time variation is a Heaviside function. The physical picture of such a source function is the final, rapid fracture of a tensile specimen, when the force on a very small area perpendicular to the force direction suddenly falls from some approximately constant value to zero. The important advantage of such a model is that it is possible to evaluate the surface displacements of the specimen due to the operation of the source.

2.4.3 Acoustic Emission Wave Propagation

During the operation of a source, elastic waves are generated and it is important to understand their propagation behaviour within a solid. Pekeris and Lifson [52] have calculated both the vertical and horizontal components of the surface displacements at various positions on the surface of a half-space, for a monopole source with Heaviside-function time dependence. Their analysis shows that the initial vertical displacement at the epicentre (the position on the surface vertically above the source, Fig. 2.12.) consists of a step function which has the same time dependence as the source. It arrives at a time h/v_L, where h is the depth of the source and v_L the longitudinal-wave speed, and has an amplitude d related to the source-force magnitude F by

$$d = k \frac{F}{\mu h} \tag{2.7}$$

where μ is the shear modulus and k can be calculated from the material elastic constants.

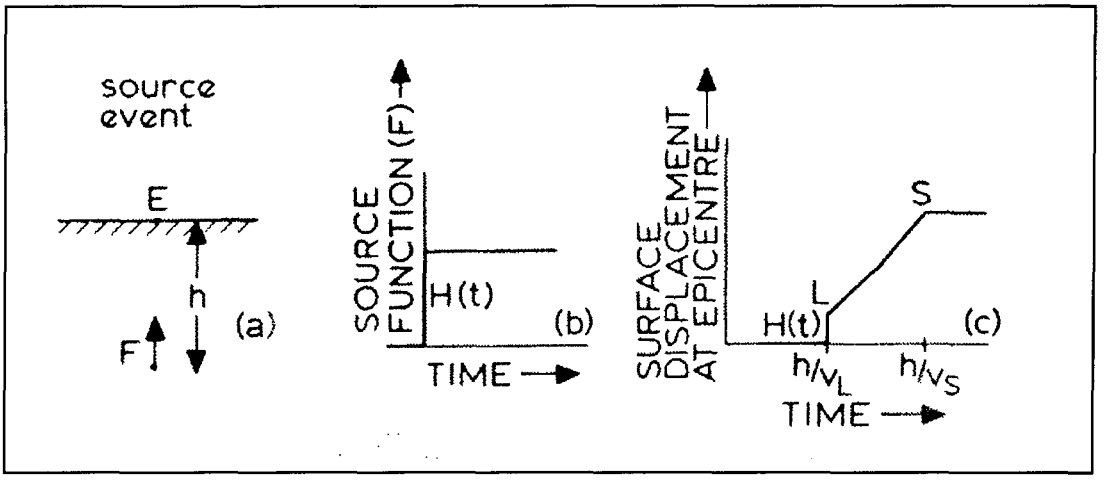

Fig. 2.12. Model used by Pekeris and Lifson [52] to calculate surface displacements consisted of (*a*) a force monopole F at vertical depth h with (*b*) $H(t)$ time variation; (*c*) at epicentre E vertical component of surface displacement consisted of a sharply rising wave step caused by arrival of compressional wave at h/v_L, followed at h/v_S by shear wave leading to a constant, finite displacement in the direction of F.

Following the longitudinal-wave arrival, the surface continues to rise until the time h/v_s when the shear wave reduces the velocity of the surface eventually to zero, to give a permanent displacement. This important result shows that it is possible to relate the time variation of a surface-displacement waveform (i.e. and acoustic emission signal) to the time dependence of the force relaxation of the source event. A second feature of Pekeris and Lifson's calculation is that the shape of the surface-displacement waveform is very sensitive to the distance of the observation position from the epicentre, Fig. 2.13. When this distance is large, the surface-displacement waveform is dominated by surface waves and it is not clear, at present, if the measurement of these can give information about the

source. An additional effect arises through the necessity for using practical specimens. In semi-infinite specimens, the wavefront from a source reaches the surface at the epicentre

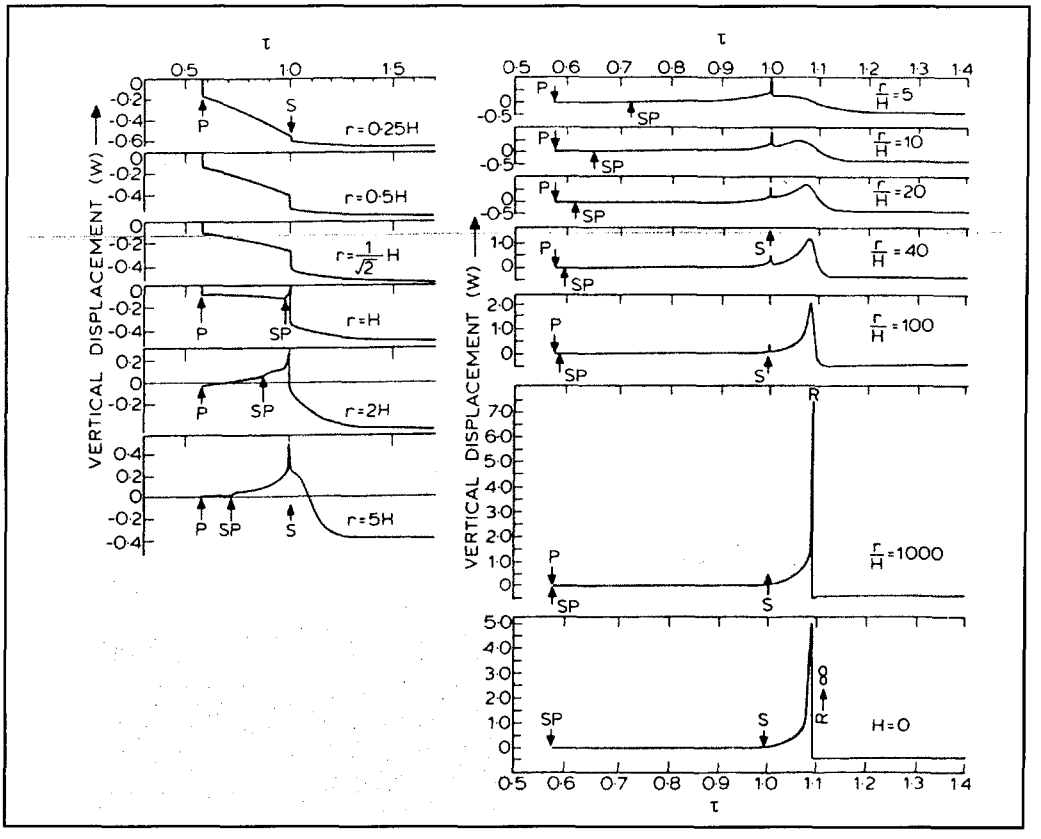

Fig. 2.13. Vertical displacement W at surface for different epicentral distances r : H is depth of source, τ is $ct / (r^2 + R^2)^{1/2}$, c is shear velocity; P, S, and R indicate arrival of compressional, shear, and rayleigh waves, respectively; SP indicates a diffracted wave which starts as S and is converted into P wave at surface; by Pekeris and Lifson [52].

in a form closely related to that generated by the source, Fig. 2.14. In a bounded specimen, however, the initial wavefronts reaching a point on the surface may have undergone multiple reflections, interference, and mode conversions (Fig. 2.15), so that the surface-displacement waveform bears little resemblance to the waveform generated by the source.

2.5 Acoustic Emission Method to Study Hot-Tearing

2.5.1 Acoustic Emission Techniques and Systems

2.5.1.1 Signal Processing and Test Systems

As explained earlier acoustic emissions are high-frequency stress waves generated by the rapid release of energy that occurs within a material during crack growth, plastic deformation, or phase transformation. The process of generation and detection is illustrated in Fig. 2.16. Sudden movement at the source produces a stress wave, which radiates out into the structure and excites a sensitive piezoelectric transducer. As the stress

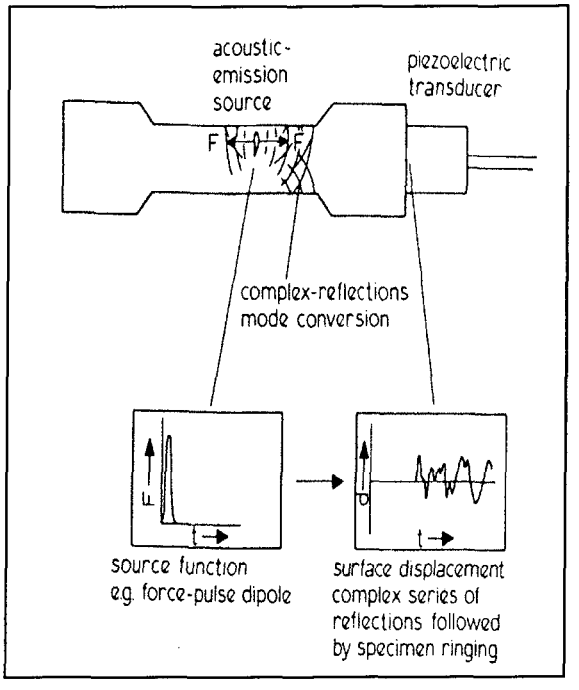

Fig. 2.14. Semi-infinite specimen: arrival of elastic waves from source cause epicentral surface displace ments at epicentre closely related to source.

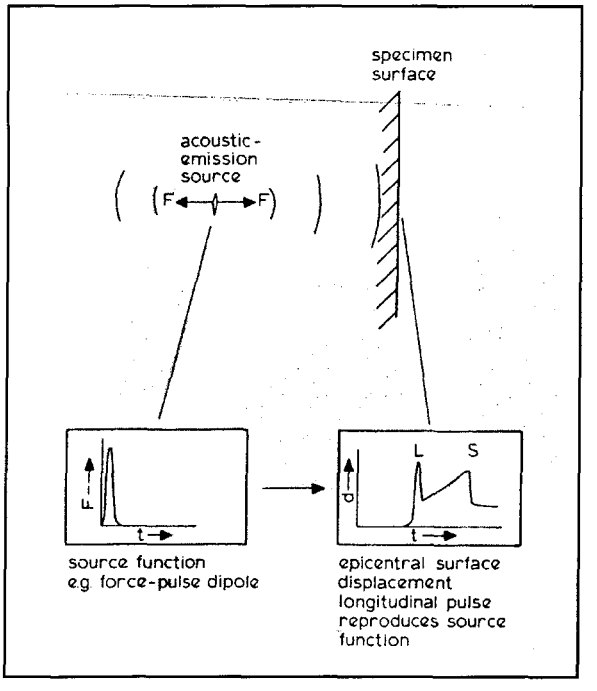

Fig. 2.15. Conventional specimen geometry modifies elastic waveform source by converting energy into normal modes of specimen; it is then extremely difficult to recover original source information.

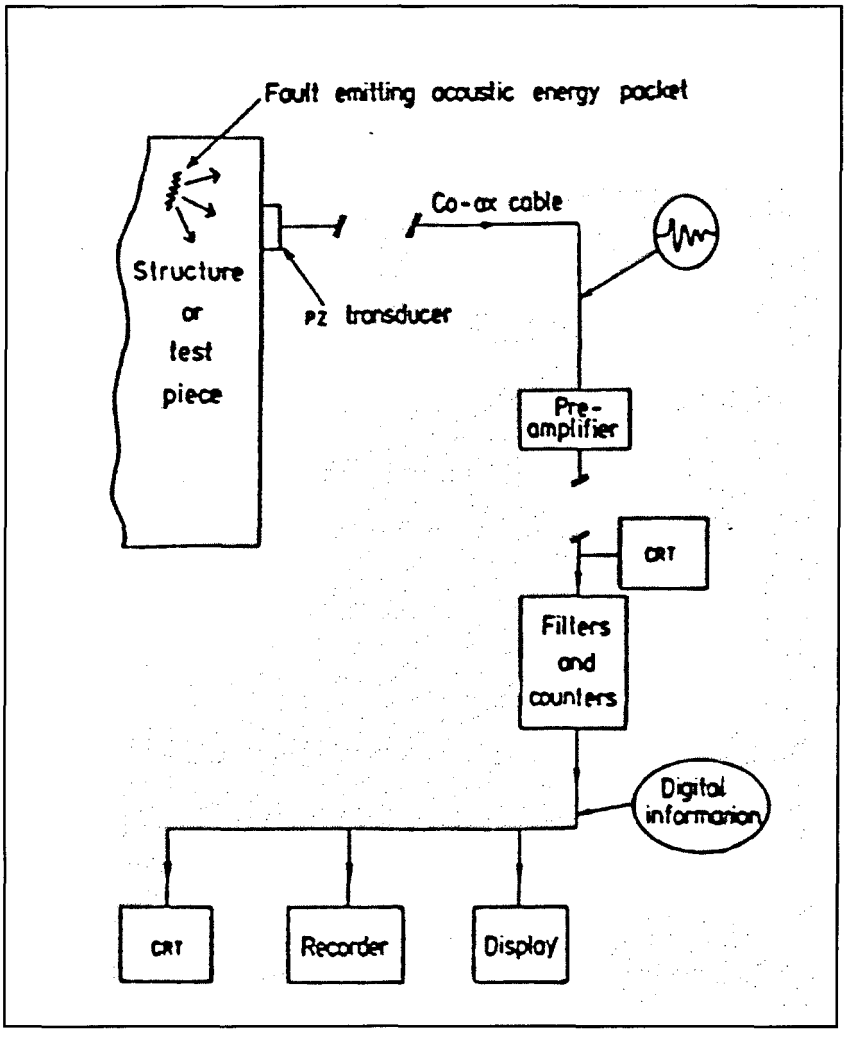

Fig. 2.16 Diagram of a simple acoustic emission detection system.

in the material is raised, many of these emissions are generated. The signals from sensor are amplified and measured to produce data for display and interpretation. The equipment, which will be described in detail below, comprises the sensor, which is sensitive piezoelectric transducer, firmly attached to the surface of the material under test, signal leads, whose design is connected to electronic signal conditioners, counters and recorders.

All the common materials used in structures (metallic alloys, glasses, polymers, ceramics and cements) exhibit acoustic emission. The transducer usually picks up a series of pulses of elastic energy rather than a continuous wave. This type of signal has a fast rise time and a slower decay. The energy and the frequency spectra of the elastic wave packets coming from the defect depend on the material, the nature of the deformation process, the local stresses at the defect, and often on the environment in which the material is placed. If there is a high rate of occurrence, the individual burst-type signals combine to form a continuous emission.

After sensing and pre-amplification, the signal is transmitted to the main instrument, where it is further amplified and filtered. With setting the threshold level, the digital pulses are output when the acoustic emission signal exceeds a fixed threshold voltage. This is a key variable that determines test sensitivity. Depending on instrument design, sensitivity may also be controlled by adjusting the amplifier gain.

2.5.1.2 Signal Measurement Parameters

1. Counts and Count Rate

The simplest way of characterizing a pulse or series of pulses produced in an acoustic emission experiment is called «ring-down» count. Fig. 2.17 shows the time-amplitude trace of a pair of typical signal bursts at the transducer. Counting the number of times per second the amplitude exceeds a preset voltage gives a simple number characteristic of the signal. An experienced operator can use this number to make observations concerning the severity of the rate of growth of a defect under study.

It will be noted that this simple approach relies on pulse counting, or in some cases, the measurement of an averaged signal amplitude. More sophisticated equipment, now generally preferred, adds energy analysis to simple counting because:

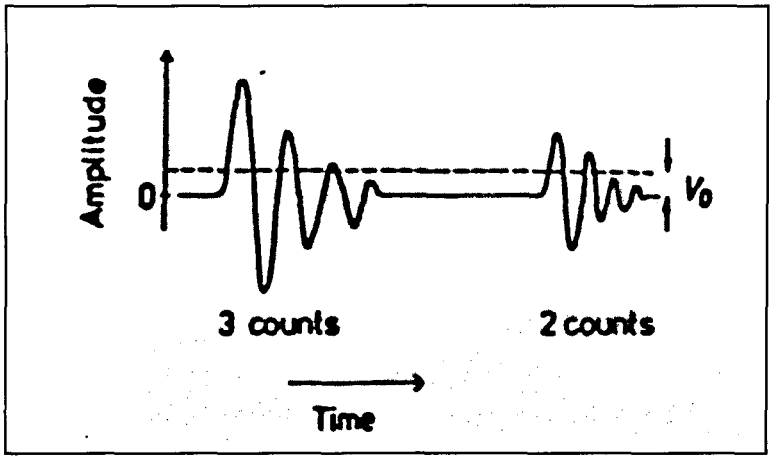

Fig. 2.17 Typical acoustic emission signal bursts; V_0 is threshold for counter.

(1) a «ring-down» count is a function of signal frequency;

(2) the count is only indirectly dependent upon amplitude because a large amplitude signal will often last longer than a low amplitude signal, i.e. the count is biased towards large amplitude pulses.

2. *Frequency Spectral Distribution*

Frequency analysis can yield information about source rise time and fracture type. The most commonly employed method of extracting frequency information from emission is a digital one in which the emission waveform after amplification is passed into a transient recorder to digitize the waveform for subsequent access into a small computer. Standard

Fourier transform routines then permit frequency analyses.

3. Energy Analysis (Energy Counts and True Energy)

The measurement of the energy in a signal by means of electronic processing is, in principle, simple. The signal voltage is first squared, and then the area under the curve of voltage squared against time is measured. This area is proportional to the signal energy with the constants of proportionality being the amplifier gain and input impedance.

$$E = \frac{1}{R}\int_0^{\infty} V^2(t)\,dt \qquad \textbf{(2.8)}$$

where

R = input impedance

V(t) = signal voltage.

Energy analysis can mean any of the following:

(1) the square of the initial pulse amplitude is measured for each burst;

(2) the area under the envelope of the amplitude-time curve is measured for each burst;

(3) the area under the actual amplitude-time curve is measured for each burst.

The electronic equipment normally used can then present a statistical analysis of the energy parameters measured on the individual bursts.

4. Amplitude and Amplitude Distribution

This is a very important parameter because it is the highest peak voltage attained by an acoustic emission waveform. Acoustic emission amplitudes are directly related to the

magnitude of the source event, and they vary over an extremely wide range from microvolts to volts. So it is expressed on a decibel (dB) scale (logarithmic), in which 1 μV at the transducer is defined as 0dBAE, 10 μV is 20dBAE, 100 μV is 40 dBAE, and so on.

5. Rise time

Rise time is the elapsed time from the first threshold crossing to the signal peak (Fig. 2.18). Governed by wave propagation processes between source and sensor, this

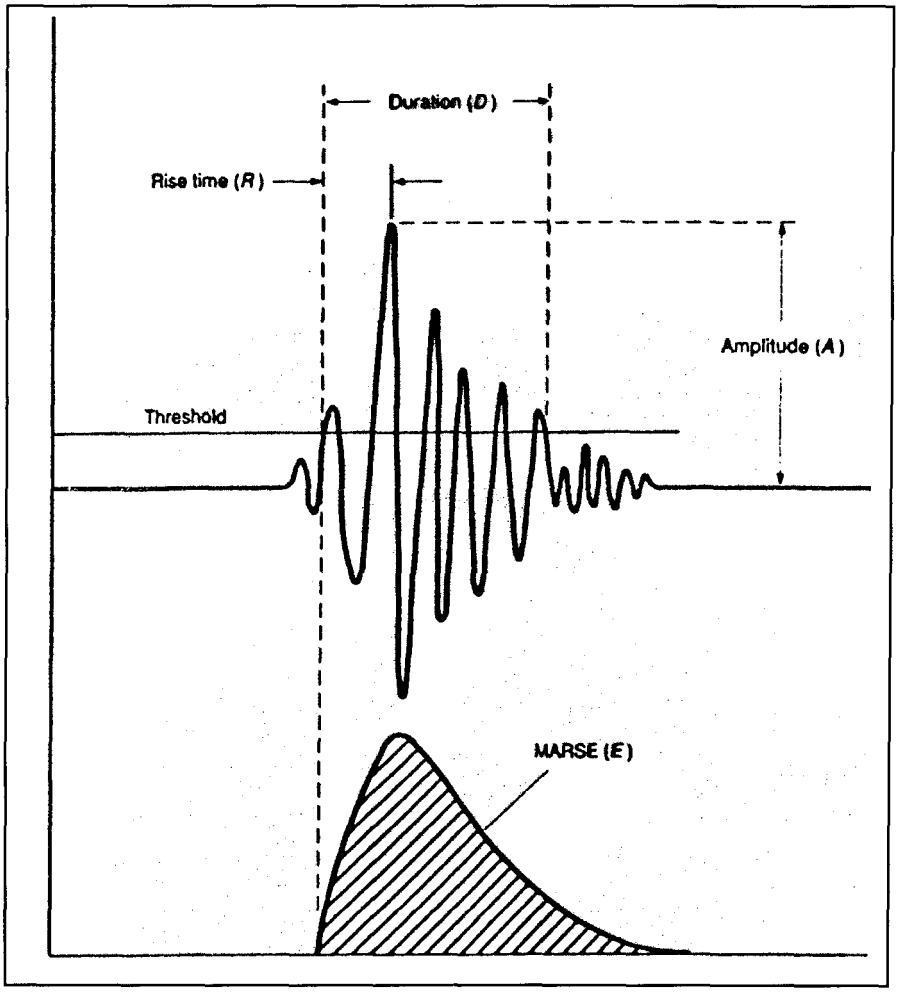

Fig. 2.18 Generally measured parameters of a burst-type acoustic emission signal

parameter can be used for several types of signal qualification and noise rejection.

6. Duration

This parameter is the elapsed time from the first threshold crossing to the last (Fig. 2.18). Directly measured in microseconds, it depends on source magnitude, structural acoustics, and reverberation in much the same way as counts. It is valuable for recognizing certain long-duration source processes such as delamination in composite materials, and it can be useful for noise filtering and other types of signal qualification.

7. RMS (Root-Mean-Square) Voltage

RMS voltage value is the most important parameter. This value is a measure of the energy content of acoustic emission signals. It can be expressed as follows:

$$V_{RMS} = \left[\frac{1}{\Delta t} \int_0^{\Delta t} V^2(t)\, dt \right]^{1/2} \qquad \textbf{(2.9)}$$

where

V(t) = the signal function, output voltage,

Δt = averaging time (time period).

The advantage of using the RMS voltage measurement is that it gives a continuous measurement of a parameter of the emission, which can be standardized and used for comparative experiments. To compare the equations 2.8 and 2.9, it is clear that RMS is different from the value of energy. RMS, meaning Root Mean Square, indicates the output voltage of one cycle; its value of voltage is generally approximately 0.707 of the peak value.

2.5.1.3 Transducers

Transducer characteristics are an important feature of the specification of acoustic emission equipment. We know, piezoelectric crystal can convert movement into an electrical voltage. Acoustic emission transducer(sensor), consists of the piezoelectric crystal. The sensor is excited by the stress waves impinging on its face, and it delivers an electrical signal to a nearby pre-amplifier and then to the main signal-processing equipment. The most important properties in an acoustic emission sensor is high sensitivity and resonant frequency. High fidelity and flat frequency response sensors are available. These sensors have one or more preferred frequencies of oscillation, governed by crystal size and shape. These preferred frequencies actually dominate the waveform and spectrum of the observed

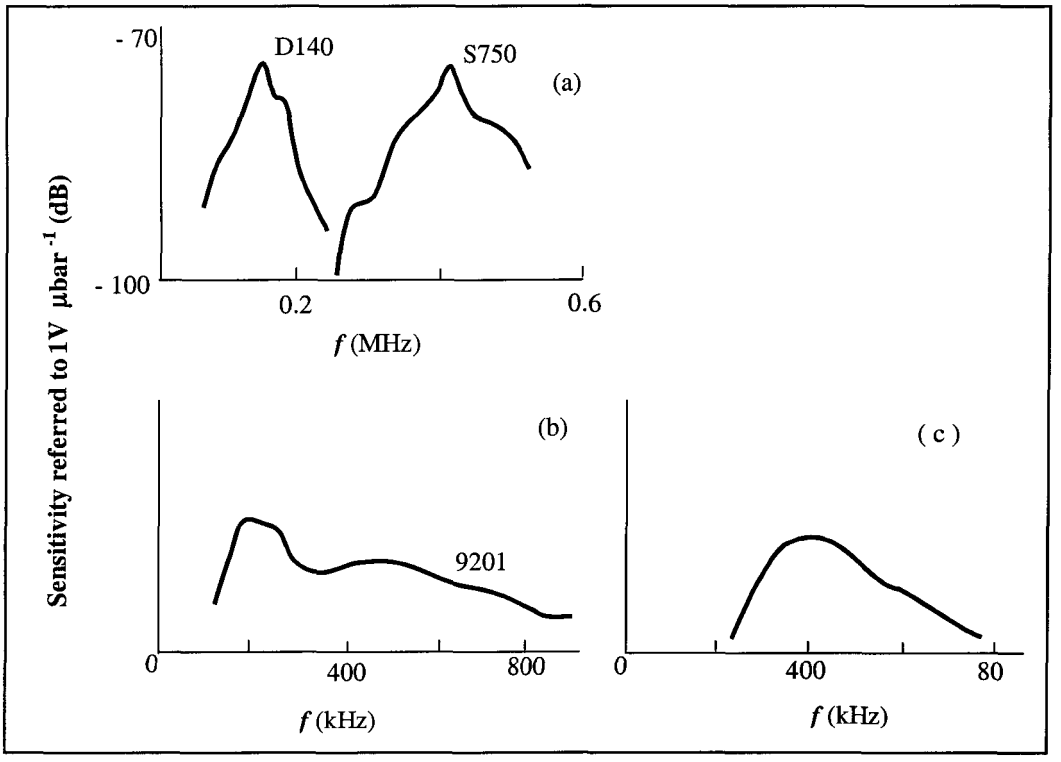

Fig. 2.19 Frequency response of acoustic emission transducers: (a) Typical, (b) Wide-band, (c) Noisy environment.

signal in typical acoustic emission testing. The sensitivity calibration of acoustic emission sensors was the subject of a substantial developmental program at the National Bureau of Standards (NBS) through the late 1970s. This program has led to the routine availability of NBS-traceable plots showing the absolute sensitivity of acoustic emission sensors in volts per unit velocity as a function of frequency [54]. Here, the frequency response of two general purpose transducers are shown in Fig. 2.19, both having a peak sensitivity of -75 dB referred to $1V\mu bar^{-1}$.

2.5.2 Study of Hot-Tearing with Acoustic Emission Techniques

With acoustic emission techniques, we can «listen» to the «talk» of materials when they are in trouble; we can also «listen» to the sounds of hot-tear formation. Therefore, we can utilize acoustic emission techniques in the metal casting processes. The acoustic emission signals generated during solidification could be used to provide information concerning the solidification phase change, as well as to identify certain casting defects generated during or immediately following the solidification process. Plastic deformation and crack propagation in any material is associated with generation of acoustic waves in the ultrasonic range. With acoustic emission techniques, these waves can be detected in real time. The hot-tearing process could be dynamically monitored with this technique.

Over the past several years, only a few researchers have used acoustic emission to study hot-tearing in solidifying alloy casting. These studies obtained AE signals during the occurrence of hot-tearing in casting. In 1985, Kuman and Prabhakar [55] reported results for an Al-Si eutectic alloy, as well as results from hot-tearing in an Al-4%Cu alloy.

Ohtaki et al.[56, 57] and Sharma et al [58] also reported on hot-tearing in aluminum alloys and have indicated that the presence of a tearing defect resulted in an increase in the acoustic emission activity during the formation of the tear. Tensi [59] postulated that the generation of acoustic emission signals could arise from the frictional noise occurring at the interface between solid crystals as the material contracts during solidification. Purvis and Kannatey-Asibu [60, 61] worked on characterizing the differences in the acoustic emission signals obtained during solidification and formation of defects to establish identifiable features that will distinguish specific signals from one another.

In the summer of 1996, in the Alcan-UQAC Chair in Solidification and Metallurgy of Aluminum (CSMA), a study was initiated that used AE in solidifying alloy castings to study hot-tearing by C. Aliravci. Tremblay & Lessard [62] used new AE equipment (MISTRAS) to obtain a series of AE signals during solidification of two aluminum alloys. This study investigated aluminum alloys that solidified with and without hot-tears. In castings that exhibited hot-tears, an acoustic emission signal with a characteristic frequency greater than 130 kHz was detected. This signal was always absent in castings that had no hot-tearing. Further work was carried out in the summer of 1997 by Marie-Eve Larouche & Xiaojin Li. They continued experiments, measuring AE signals and Cooling Curves of the aluminum alloys AA3105 and AA1050. Through these experiments, the use of AE as an experimental method was proven to be feasible.

A summary of the above mentioned investigations, on the use of AE in hot-tearing studies is shown in Table 2.2:

Table 2-2 Summary of previous AE investigations.

	Parameters measured	Materials used	Test mold type
Prasanna Kumar T.S. and Prabhakea, O.	i) RMS voltage ii) Event Rate and Event Count iii) Peak Amplitude Volt iv) Rise Time Distribution v) Temperature of Cooling	Al-11.6%Si alloy Al-4%Cu alloy	Cast iron dies (200mm)
Sharma, D.G.R. Et al	i) RMS voltage ii) AE energy iii) Temperature of Cooling iv) Deformation of the hot-tear zone v) Contraction of free end	Al-Cu Alloy: Al-3.0%Cu Al-4.0%Cu Purity Al	Cylindrical bar (by Van Eephom and De Sy [14]) CO_2-Core moulds
Ohtaki et al	i) The peak voltage ii) Ring-down rate iii) Temperature of Cooling	Al-7%Si Alloy	Three types of molds: i) Non directionally and uniformly solidifying castings ii) A load was applied to the solidifying test bar, in order to produce fracture of the casting in the solid-liquid state iii) I-beam test mold
Purvis, A.L.	i) RMS voltage ii) The cumulative ring-down counts iii) AE events iv) Burst duration v) Peak Amplitude	Al alloy 319 (6%Si, 3.5%Cu)	Restrained bar (by Rosenburg, Flemings and Taylor [17]) Test casting in both oven-dried and green molding sands
CSMA (University of Quebec in Chicoutimi	i) RMS voltage ii) Average frequency iii) AE events iv) Burst duration v) Peak Amplitude vi) Temperature of Cooling	AA1050 Alloy (0.4%Fe,0.25%Si, 0.05%Cu, 0.05%Mn 0.05%Mg, 99.5%Al) AA3105 Alloy (0.7%Fe, 0.6%Si, 0.3%Cu, 0.2-0.8%Mn 0.2-0.8%Mg, 0.2%Cr)	A steel, ring shaped permanent mold Characteristics AE Signals for hot-tearing were found to be of frequency higher than 130 kHz

Chapter III

Experimental Method

3.1 Materials

The commercial aluminum alloy used in this study was AA1050. In the first set of examples standard commercial AA1050 alloys were used. Then, experiments were carried out on specially prepared AA1050 and in-house grain-refined AA1050 alloys. Non-grain refined and grain-refined AA1050 alloys were used for repeated experiments. The standard chemical composition of the commercial AA1050 alloy is given in Table 3-1. The composition of the actual AA1050 alloy samples studied is shown in Table 3-2. The composition of special non-grain refined and grain-refined AA1050 alloys are shown in Table 3-3. All alloys were supplied by Alcan International Inc.

It is known that iron and silicon are present in AA1050. During the solidification process such an alloy behaves mainly as a ternary Al-Fe-Si alloy, and at the end of the process, forms eutectic Al + Al_3Fe, and also exhibits a ternary reaction expressed as liq + $Al_3Fe \rightarrow Al_8Fe_2Si$ [62]. The related phase diagrams are shown in Figs 3.1 a) and b).

Table 3-1 Chemical compositions of commercial AA1050 alloy standard [63]

Alloy	Elements of Alloys (%)						
AA1050	Fe	Si	Cu	Mn	Mg	Other (each)	Al
	< 0.40	< 0.25	< 0.05	< 0.05	< 0.05	< 0.03	< 99.5

Table 3-2 Chemical compositions of the actual sample of AA1050 alloy

Test No.	Elements of Alloys (%)						
	Fe	Si	Ti	B	Cu	Mg	Mn
1002	0.32	0.12	0.002	0.00176	0.001	0.003	0.002
1003							
1005	0.30	0.11	0.002	0.00165	0.002	0.001	0.002
1010	0.22	0.11	0.002	0.00062	0.001	0.001	0.002
1011	0.22	0.13	0.002	0.0030	0.002	0.002	0.002
1013	0.21	0.11	0.002	0.0010	0.001	< 0.001	0.002
1014	0.16	0.11	0.001	0.00071	0.001	0.001	0.002
1016	0.16	0.11	0.002	0.0015	0.001	< 0.001	0.001
1017	0.14	0.10	0.001	0.0005	0.001	< 0.001	0.001
1018	0.068	0.06	0.002	0.0002	0.001	< 0.001	0.001
1019	0.064	0.056	0.002	0.0006	0.001	< 0.001	0.001
1020	0.063	0.058	0.002	0.0010	0.003	< 0.001	0.001
1021	0.065	0.056	0.002	0.0012	0.001	0.001	0.001
1022	0.064	0.057	0.002	0.0006	0.004	< 0.001	0.001
1023	0.068	0.060	0.002	0.0009	0.004	< 0.001	0.001
1025	0.055	0.058	0.002	0.0006	0.006	< 0.001	0.001
1026	0.059	0.062	0.002	0.0007	0.007	0.001	0.001
1027	0.067	0.068	0.002	0.0006	0.007	< 0.002	0.001
1028	0.064	0.066	0.002	0.0013	0.007	0.001	0.001
1029	0.053	0.059	0.002	0.0007	0.004	< 0.001	0.001
1030	0.060	0.063	0.002	0.0016	0.005	< 0.001	0.001
1032	0.052	0.060	0.002	0.0007	0.015	< 0.001	0.001
1033	0.059	0.064	0.002	0.0004	0.016	< 0.001	0.001
114	0.30	0.12	0.002	0.00098	0.001	0.005	0.006
116	0.31	0.14	0.002	0.00096	0.002	0.007	0.007

Table 3-3 Chemical compositions of grain-refined and with non-grain refined AA1050

Test No.	Elements of Alloys (%)						
	Fe	Si	Ti	B	Cu	Mg	Mn
1034	0.31	0.071	0.002	0.00023	0.001	<0.001	0.001
1035							
1040							
1041							
1042	0.29	0.089	0.002	0.00102	0.001	0.001	0.002
1043	0.32	0.099	0.004	0.00170	0.004	<0.001	0.001
1044							
1046							
1039	0.29	0.094	0.012	0.00328	0.002	<0.001	0.001
1045							
1047							
1036	0.30	0.067	0.034	0.00645	<0.001	<0.001	0.001
1037							

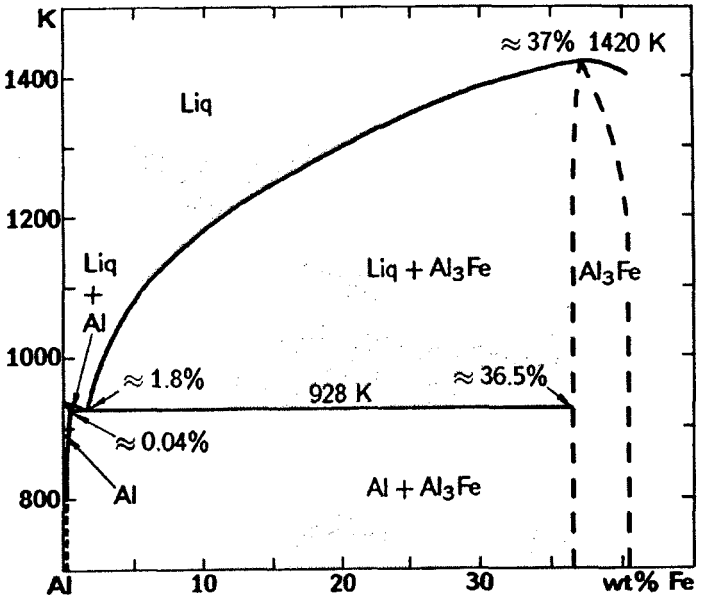

Fig. 3.1 a) The aluminum end of the aluminum-iron equilibrium diagram (by Lennart Backerud [62])

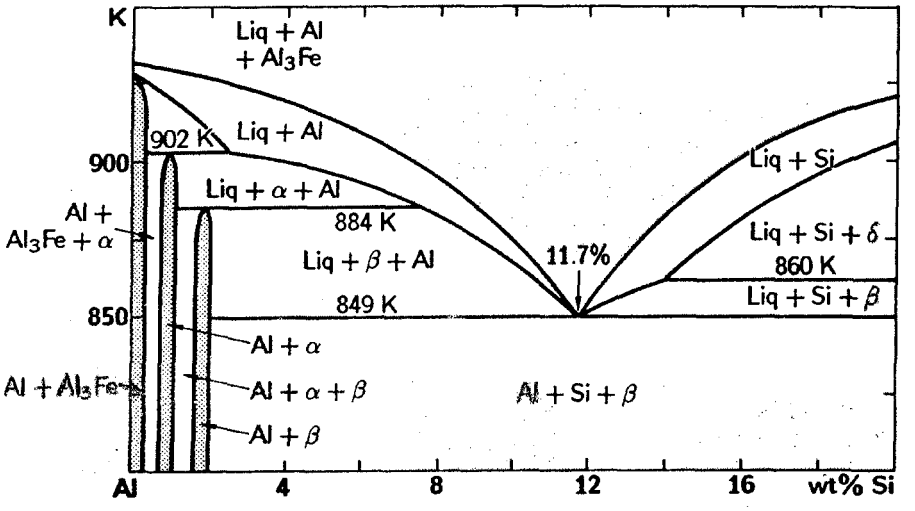

Fig. 3.1 b) Section of the aluminum-iron-silicon diagram with 0.7% Fe (by Lennart Backerud [62])

3.2 Mold

The permanent ring mold was chosen to produce hot-tear specimens for this study. The design and dimensions of the mold are shown in Figure 3.2. It consists of two parts: a concentric core and an outer ring mold, with an annular space between them. The metal is poured into the annular space between the outer ring mold and the core. The mold produces 70 gram alloy samples. The special ring mold causes a hot tear to occur in the casting during the solidification process when the contraction is radial excessively restrained by the mold or cores. The core is steel, and this material is chosen because it can resist the contraction of the metal when it is solidifying. The insulating material B3 is used for the outside of the mold because it has higher specific heat and lower conductivity so that the rate of heat extraction is not too high. This allows for sufficient solidification time

so that a complete cooling curve can be obtained during the experiment.

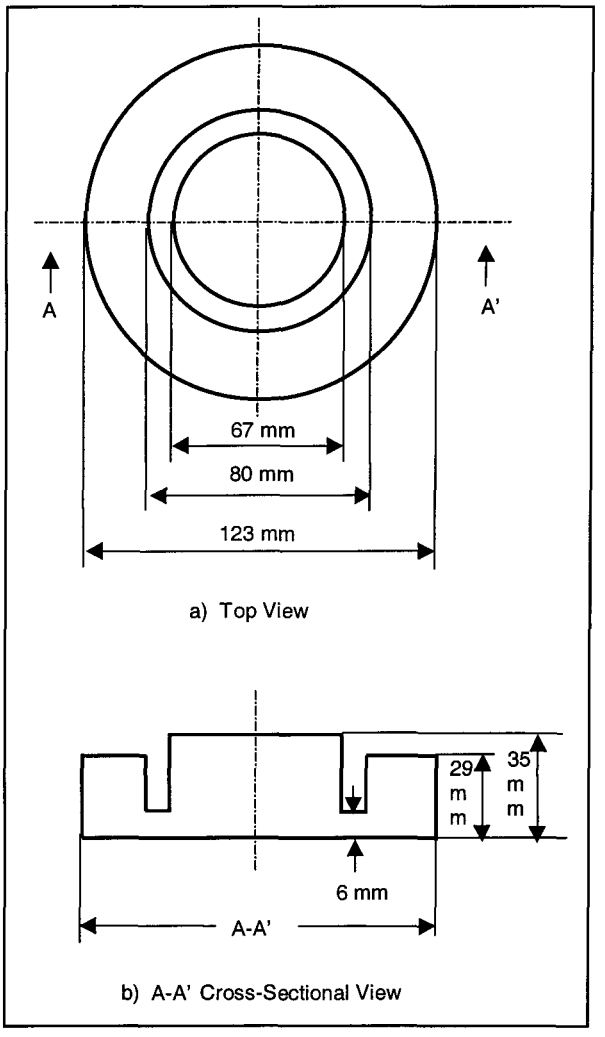

Fig. 3.2 Shape and dimension of ring mold for casting hot-tearing test.

3.3 Experimental Set-Up and Procedure

The experimental set-up is schematically illustrated in Fig. 3.3. It consists of (i) a ring casting mold, (ii) an acoustic emission system and (iii) a temperature-data acquisition

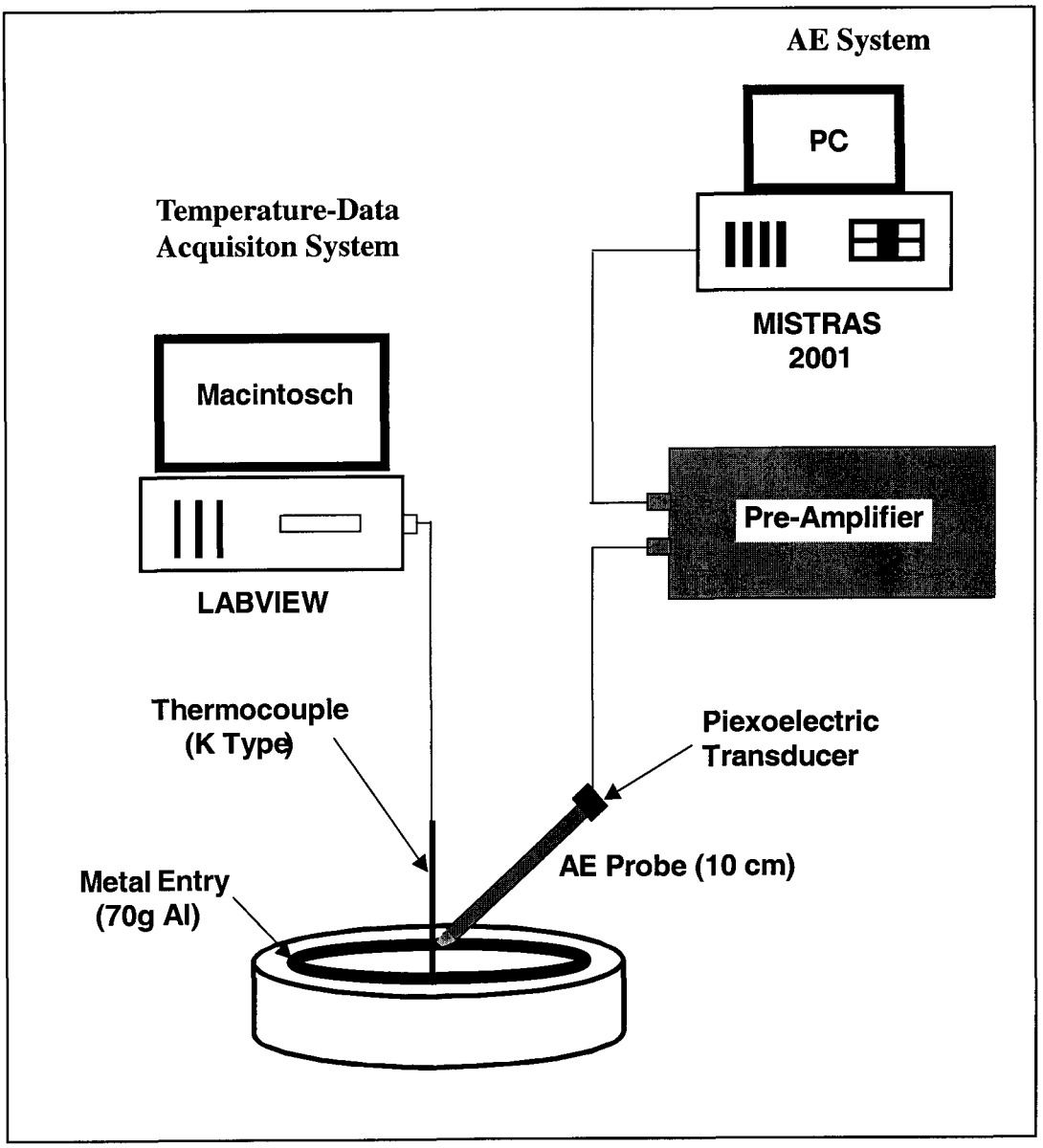

Fig. 3.3 Schematic experimental set-up.

and thermal analysis system. The acoustic emission system contains an acoustic emission wave-guide (AE probe) inserted into the ring mold. The AE probe (Fig. 3.4) is connected to the signal processing system of MISTRAS supplied by the Physical Acoustic Corporation. The piezoelectric transducer captures the AE signals generated by the hot

tearing and characteristic signals are output by the MISTRAS (Fig. 3.5). The thermocouple generates temperature-time data to give the cooling curve and the fraction solid evolution during solidification.

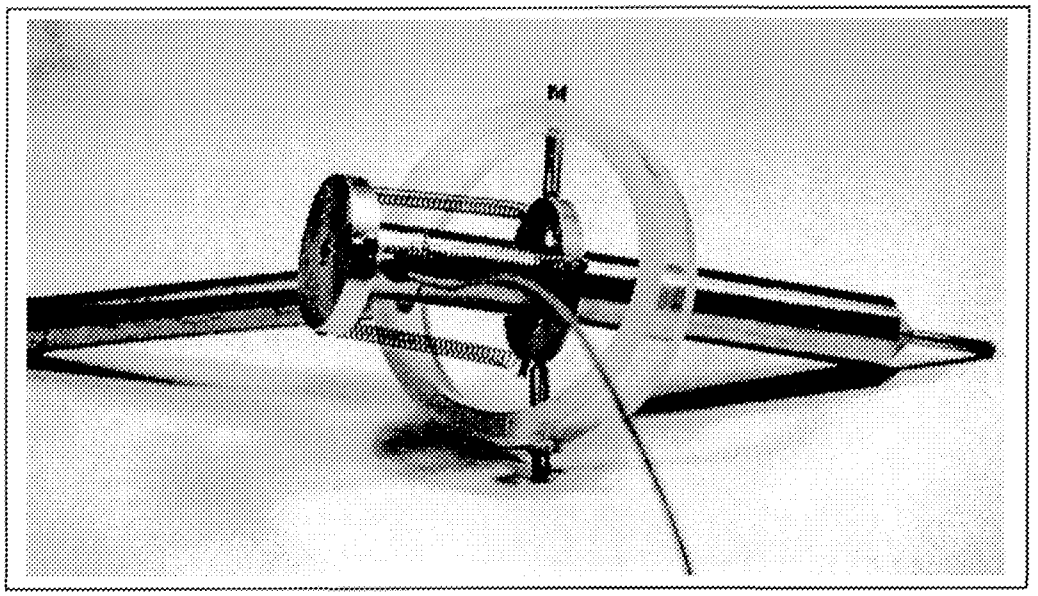

Fig. 3.4 The acoustic emission probe.

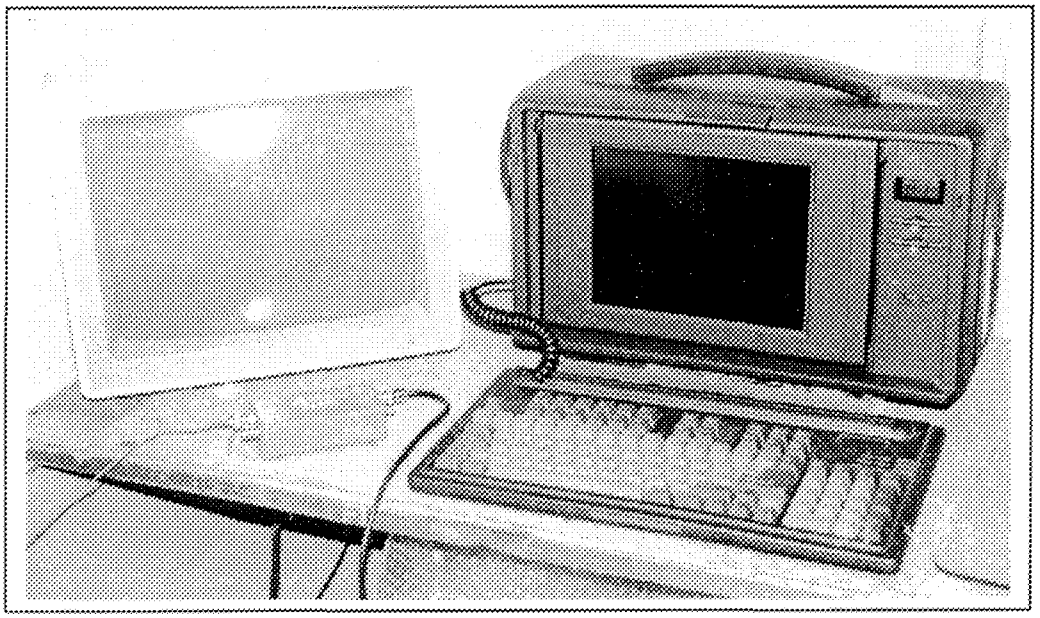

Fig. 3.5 The acoustic emission instrument MISTRAS-2001.

3.3.1 AE Information Equipment System

Fig. 3.6 shows a block diagram of the AE measurement system. The AE probe (steel) is inserted into the solidifying casting as shown in Fig. 3.7. It transmits the AE waves to the piezoelectric transducer with a resonant frequency of 154 kHz. The signals are then amplified to 60 dB (×1000) by a pre-amplifier, passed to a band pass filter with a 100-300 kHz band pass, and processed with an electronic AE signal processing unit. Finally, the data is displayed. The present AE instrument is called MISTRAS-2001, and it is manufactured by the Physical Acoustic Corporation.

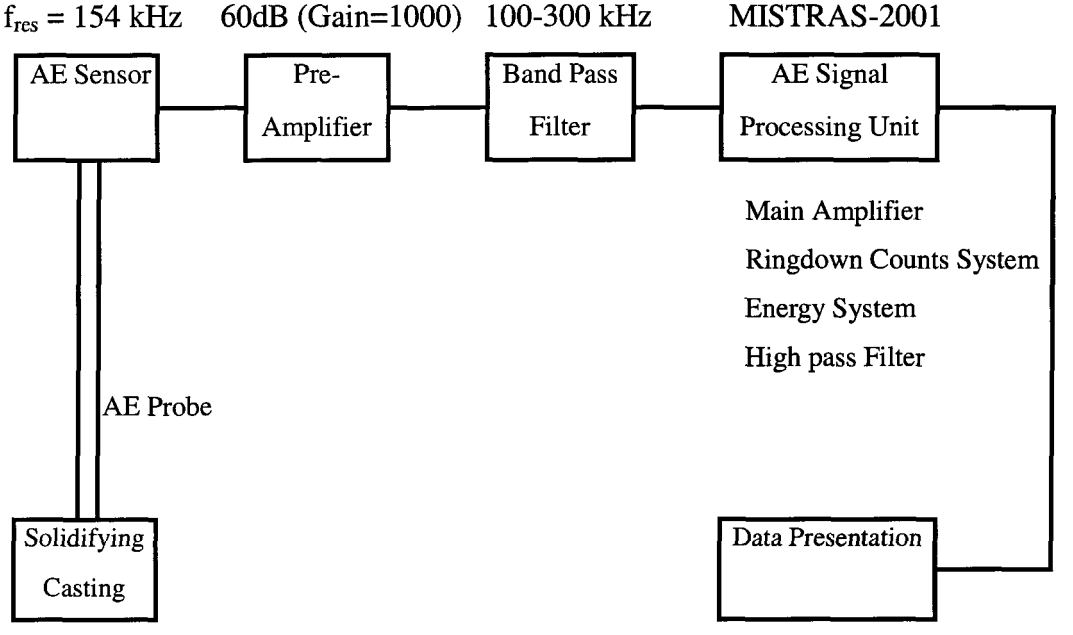

Fig. 3.6 Block diagram of the AE measurement system.

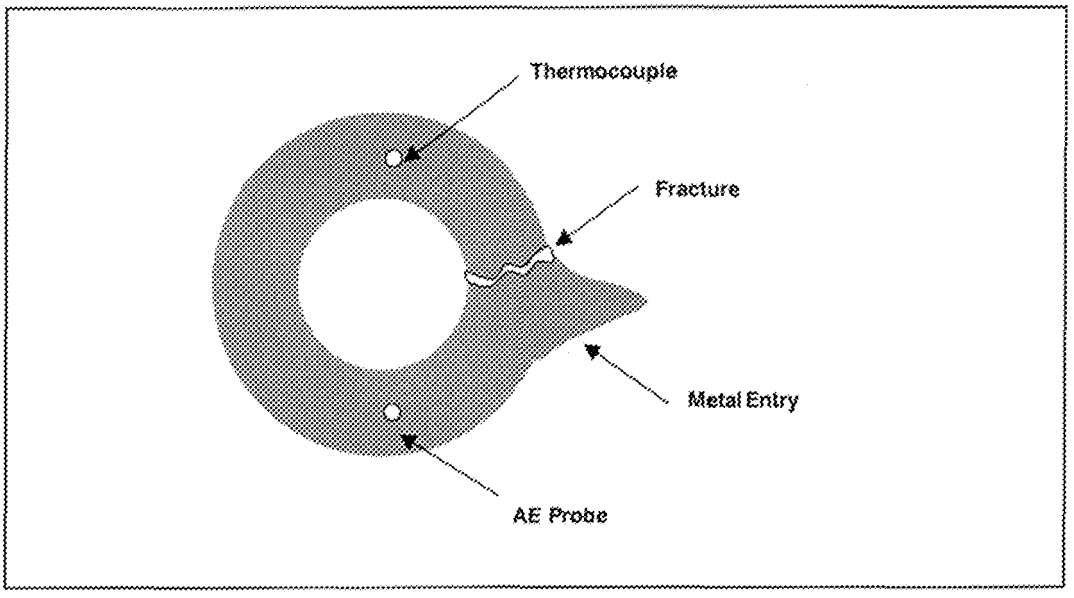

Fig. 3.7 a) The locations of AE probe and thermocouple in the casting.

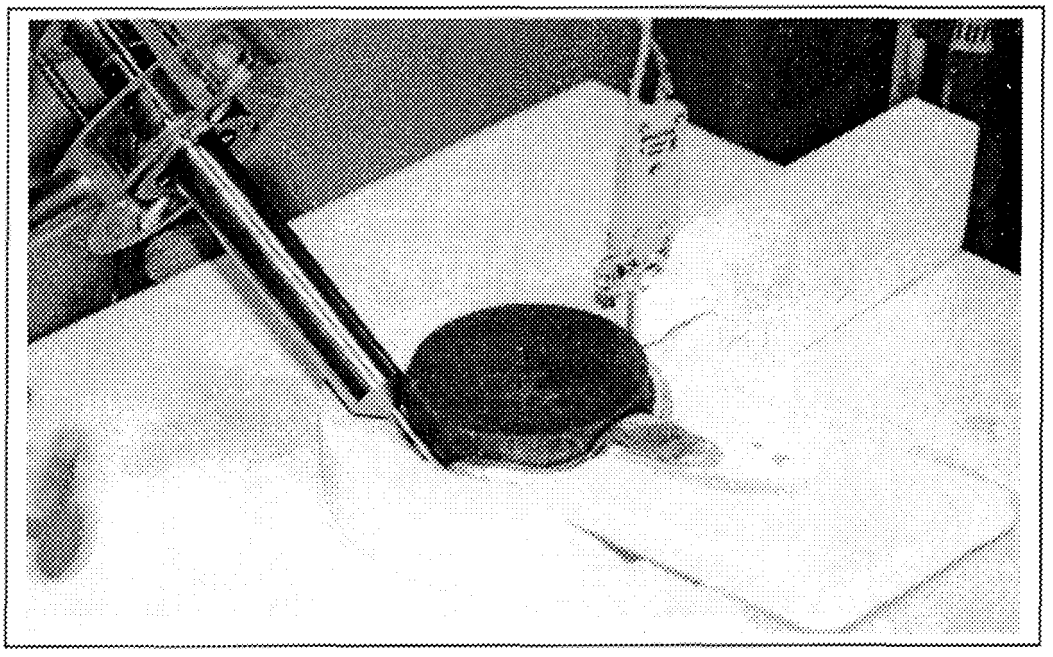

Fig. 3.7 b) The photograph shows the location of AE probe and thermocouple in the casting.

3.3.2 Thermocouple System

Temperature monitoring of the test casting provides information regarding events that occur during the solidification process. The information obtained from this thermal analysis can prove to be very useful in determining the likely sources of AE activity when they occur in the solidification process. The temperature of the test casting was detected using a 0.06-inch diameter, K type (alumel-chromel) thermocouple supplied by Omega. The thermocouple was inserted into the final freezing zone of the solidifying casting, the opposite side of the AE probe. The temperature-time history was recorded with a data acquisition system, "LABVIEW" supplied by National Instruments. The rate of data acquisition used was 72 Hz and the solidification rate was about 20—30 C/sec in our experiments. The use of an acquisition rate that is two-to-three times the solidification rate is the recommended practice in data acquisition.

3.3.3 Melting and Casting

Fig. 3.8 a) schematic and b) photograph show the method of melting and casting. A resistance-type electric furnace was used to melt 1 kg of the alloys. Because the mold is very small, the metal loses heat very fast during the casting. In order to guarantee pouring temperature of 800°C, the temperature of molten metal in the furnace was maintained at 830°C. A small crucible was used to remove 70g of metal from the melt. The crucible was gradually dipped into the melt. When it became red-hot it was completely immersed in the melt and filled with liquid metal at 800°C. It was then poured quickly into the mold

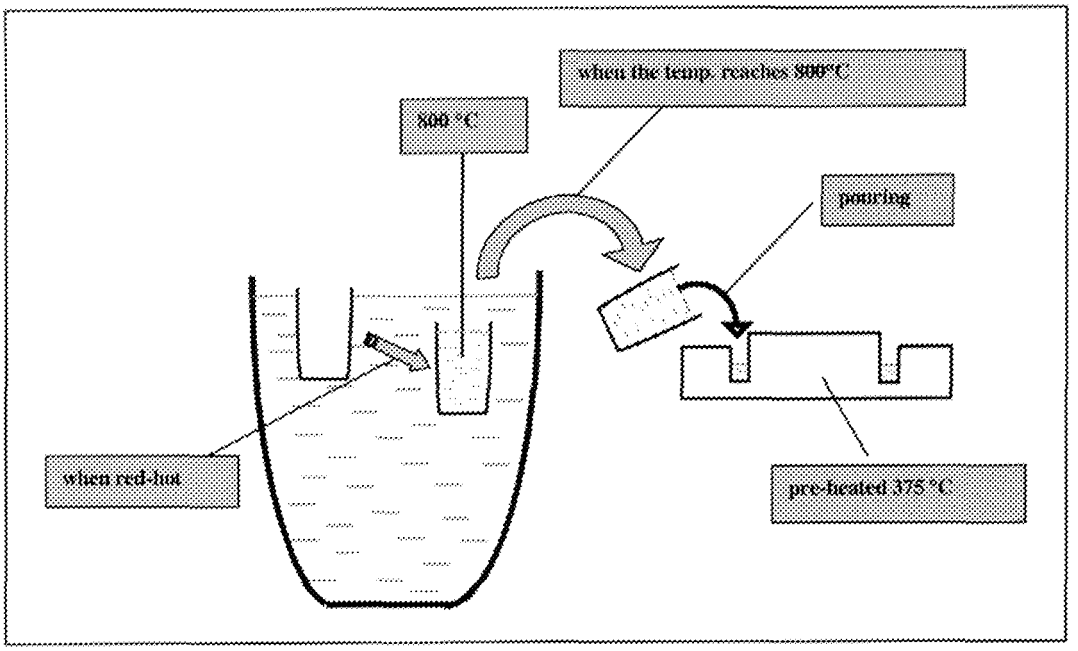

Fig. 3.8 a) Schematic illustrating the method of melting and casting.

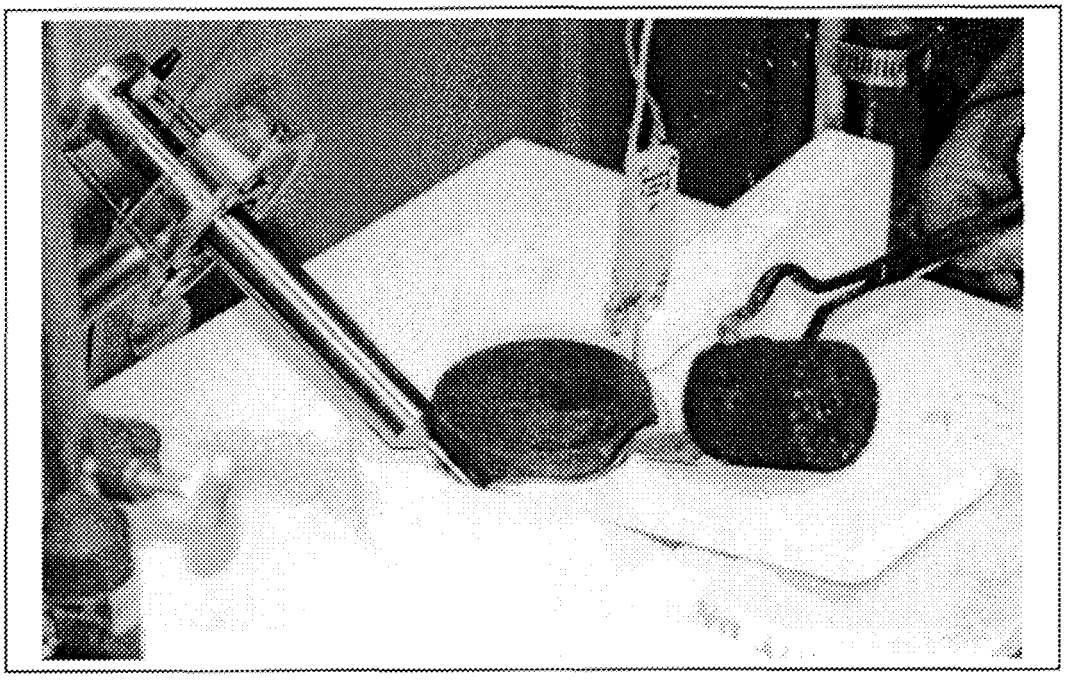

Fig. 3.8 b) The photograph shows the method of melting and casting.

This pre-heated temperature provides a good condition to get a complete cooling / solidification curve for this casting test (small mold and specimen). Two acquisition systems (AE and thermal) were started at same time as the molten metal was poured into the mold. The experiment was run for 60 seconds from the time of pouring until the temperature dropped to below 450°C.

3.4 Analytical Methods

3.4.1 Thermal Analysis (Cooling / Solidification Curve)

The cooling curve was obtained through thermal monitoring of the test casting. The

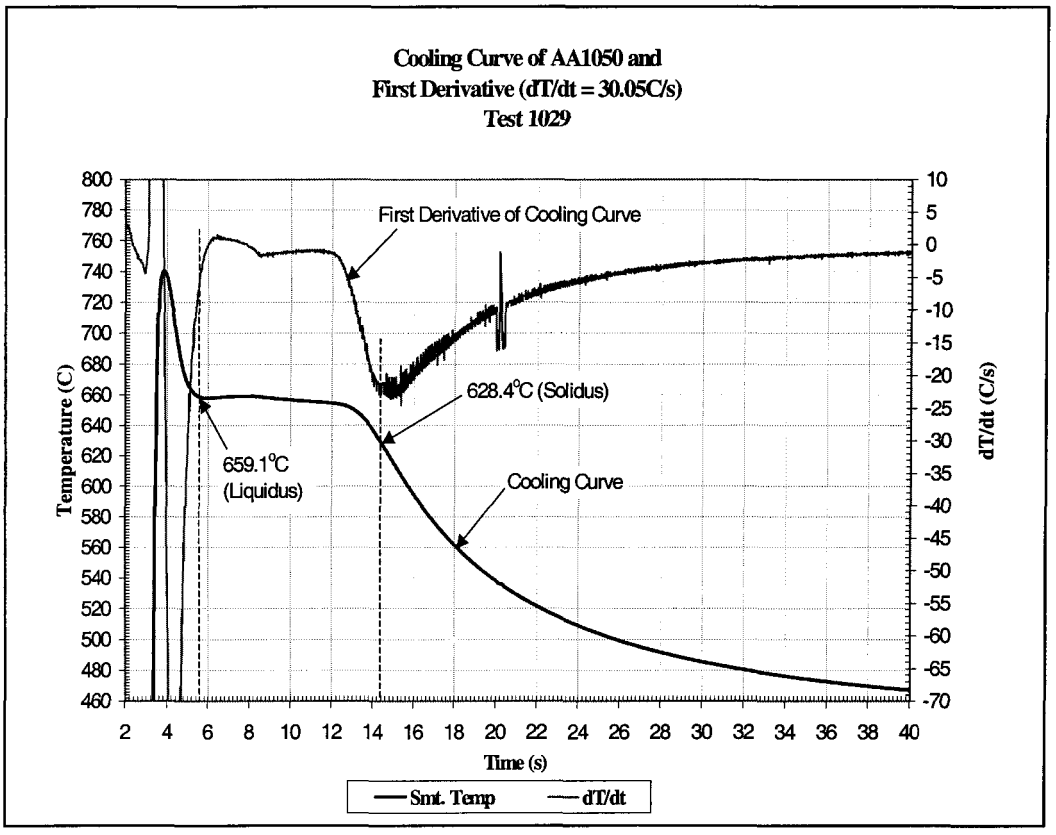

Fig. 3.9 The cooling/solidification curve and its first derivative.

cooling curve and its first derivative were then analyzed to determine both the liquidus and solidus arrests, which aids in determining the solidification activity on an elapsed time basis from the time of initial pouring of the casting. An example of the results obtained are shown in Fig. 3.9.

3.4.2 AE Signal Analysis

The types of AE signals output by the MISTRAS system are (i) AE energy; (ii) RMS (Root-Mean-Square) voltage; (iii) Average frequency; (iv) Peak Amplitude; (v) AE ring-down counts; and (vi) Burst duration. Fig. 3.10 shows an example of AE signals obtained from one test: AE Energy and RMS voltage, Average Frequency and AE Ring-down Counts. From Fig. 3.10, it is seen that several peaks are obtained during the solidification process indicating the occurrence of several solidification events. Fig. 3.10 shows the amount of AE energy is released, the frequency, and the ring-down counts in each solidification event clearly. Through AE characteristic features analysis, useful information of each solidification event, such as the forming and developing process of hot-tearing, and hot-cracking can be obtained.

3.4.3 Superposition of AE Signals and the Cooling / Solidification Curves

The superposition of the AE signals and the cooling/solidification curve yields information as shown in Fig. 3.11. It can be considered that each AE signal peak represents some solidification event. It is known based on previous studies that the high frequency stress waves generated by the rapid release of energy are produced by a hot-tear event.

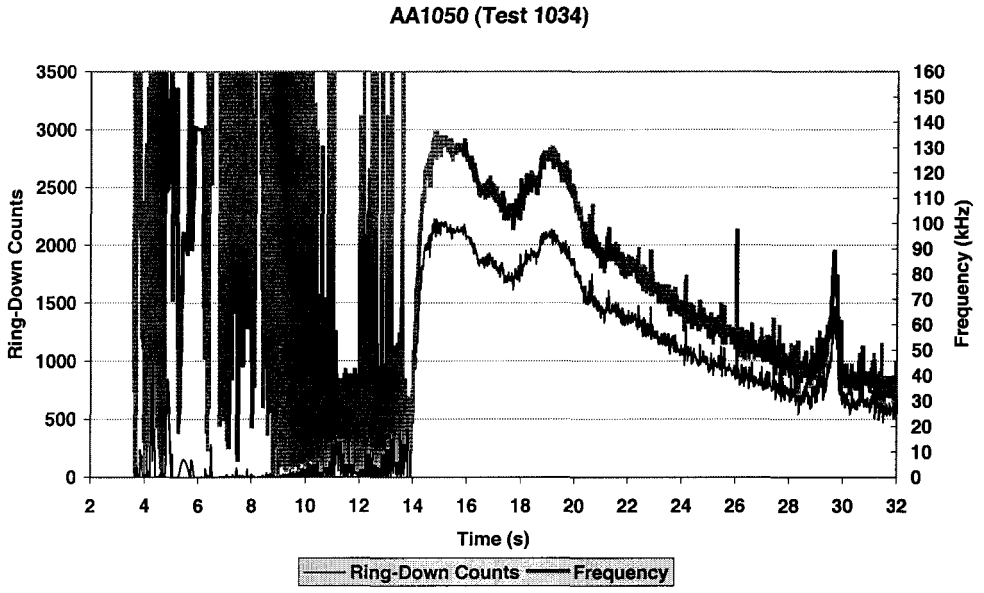

a) Average frequency & AE ring-down counts;

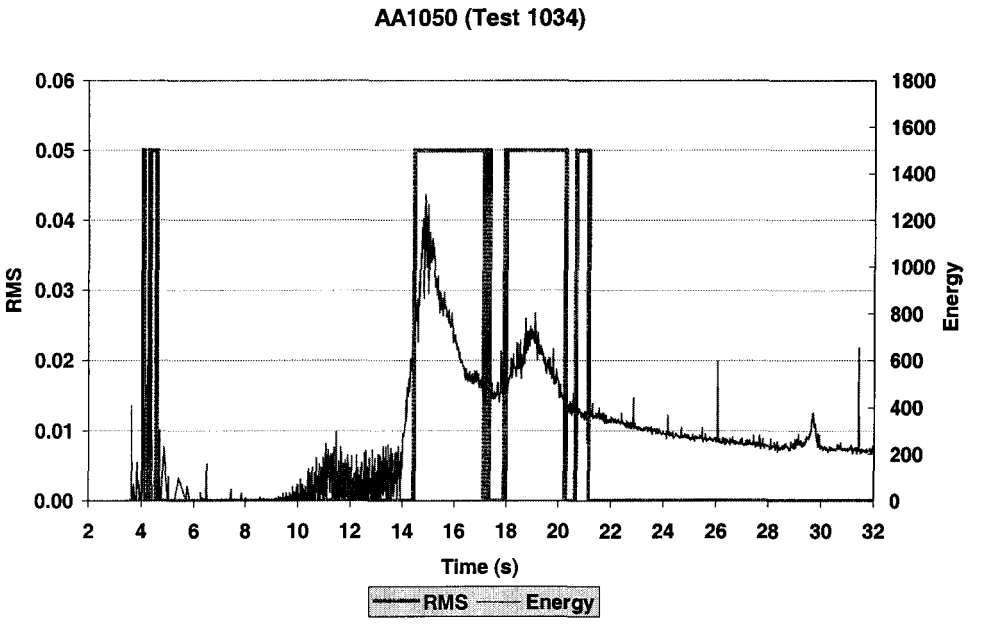

b) AE energy & RMS voltage.

Fig. 3.10 The typical output of acoustic emission signals: a) Average frequency & AE ring-down counts; b) AE energy & RMS voltage.

The continuous type of AE is known to occur when a large number of events occurs simultaneously in the entire volume of the test material. Previous work [58] has shown that a hot-tearing event can be distinguished from other events during the solidification process. The superposition of AE signals with the cooling curve also reveals with its characteristic frequency, the time that the hot-tearing event occurred, the amount of energy released due to hot-tearing.

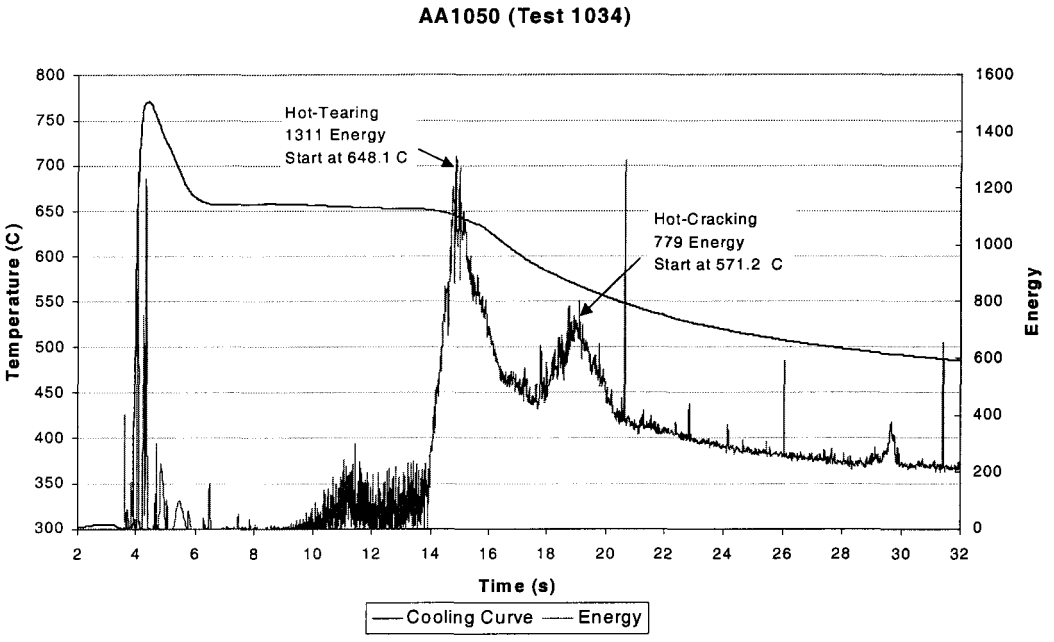

Fig. 3.11 The superposition of the AE signals and the cooling/solidification curves.

3.4.4 Fraction Solid Calculation

Fraction solid calculations are based on total fraction of latent heat released during the course of solidification. A computer program prepared by Aliravci et al. [64] was used to calculate solid fraction from the cooling curve data. A typical cooling curve, its first

derivative $(dT/dt)_{CC}$ and zero curves $(dT/dt)_{ZC}$ (curve where no phase change is assumed,) are shown in Fig.3.12. The calculation of the areas under the $(dT/dt)_{CC}$ and $(dT/dt)_{ZC}$ by numerical integration, and subtracting the area under the $(dT/dt)_{ZC}$ from the area under the $(dT/dt)_{CC}$ gives the total latent heat of fusion evolved during solidification. Subsequently, the fraction-solid as a function of time can be calculated as shown in the following equation:

$$f_S(t) = L_t / L \qquad (3.1)$$

where L_t is the latent heat evolved up to time t and L is the total latent heat evolved at the end of the solidification. By fraction solid calculation, the fraction solid while hot-tearing

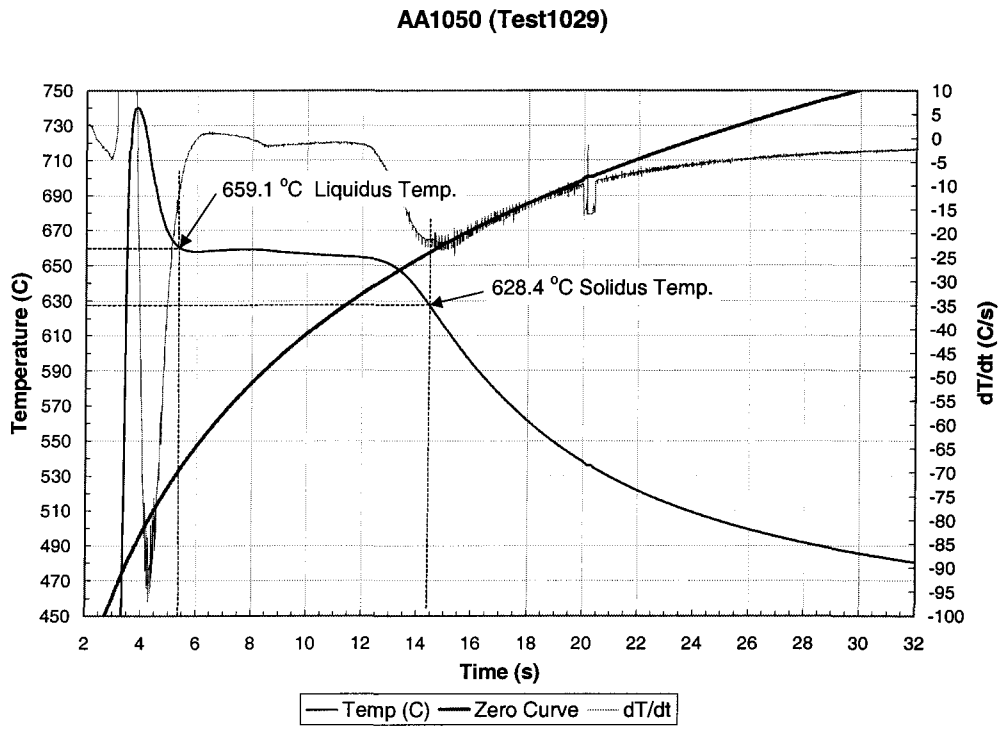

Fig. 3.12 The cooling curve, its first derivative and the null (Zero) curve for one test.

is occurring will be known, thus the occurrence mechanism of hot-tearing can be better understood.

3.5 Scanning Electron Microscopy (Fracture Surface Examination)

In order to further study the mechanism of hot-tearing from a microstructural perspective, the fracture surface of hot-tearing was investigated with scanning electron microscopy (SEM). A SEM examination of the fracture surface of a typical torn sample in our series of experiments (hot-tearing test 1010 for AA1050) is presented in Fig. 3.13. These photographs show free dendrites on the fracture surface, which indicates the presence of a hot-tearing defect rather than a hot crack.

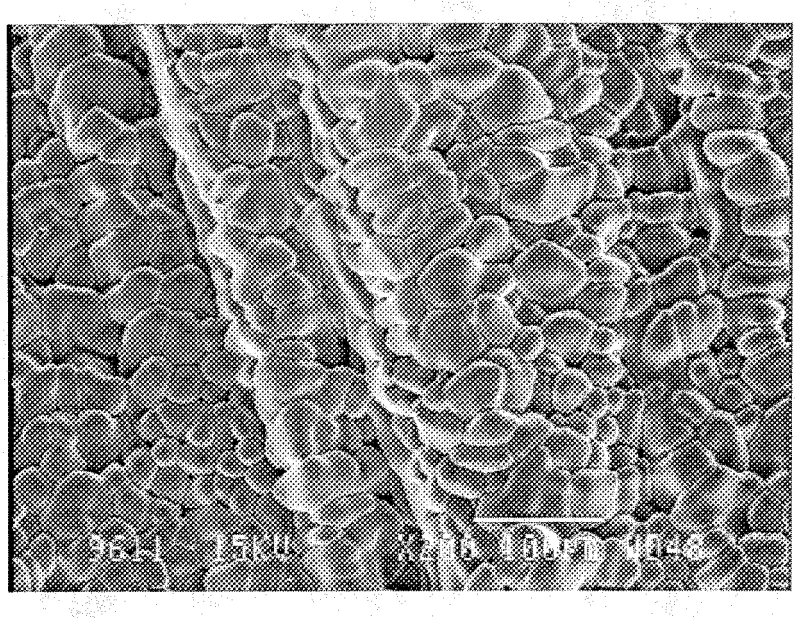

(a)

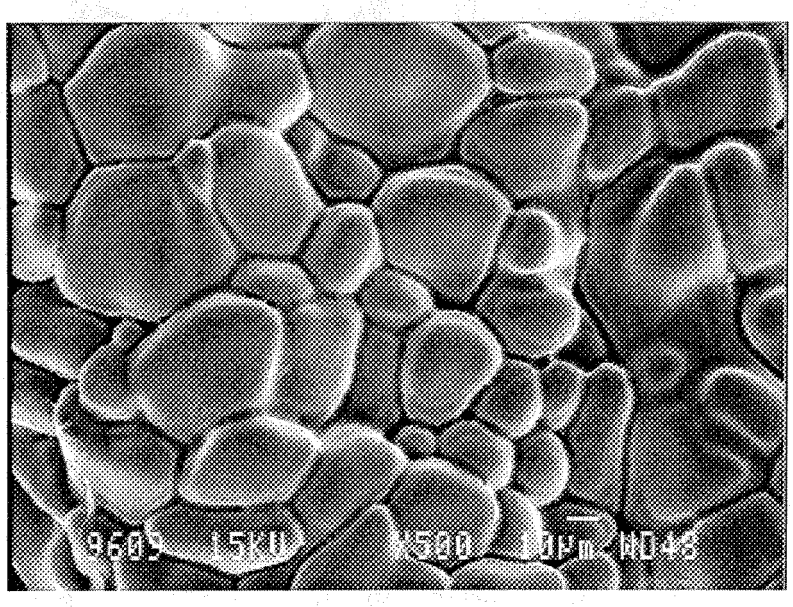

(b)

Fig. 3.13 SEM photos for a typical fracture obtained from hot-tearing experiments for AA 1050: the microstructure of the fracture surface for test 1010: (a) 200X magnification; (b) 500X magnification.

Chapter IV

Results and Discussion

4.1 Experimental Results

In order to develop an experimental procedure that produces hot-tear signals, the first series of tests of the commercial aluminum alloy AA1050, was carried out with six different conditions. The six conditions are shown in Table 4-1. Appendix I shows the test results where AE signals and the cooling/solidification curves are superposed. The test results obtained to date are summarized in Table 4-2.

In Group A tests, the mold pre-heat temperature was 180°C. These resulted in a very high solidification rate and obtained a good solidification curve that can determine solidification events corresponding to AE signals. Through repeated tests, the optimum mold pre-heat temperature was fixed at 375 °C, so that more suitable solidification duration could be obtained.

The average cooling rate (CR) is between 20~50 °C/s in our casting, and the optimum acquisition rate for a casting is 2~2.5 times the CR, hence we need a data acquisition rate of 72 data points per second (72/sec). In order to guarantee test measurement precision and

obtain the best cooling curve to analyze the cooling rate, liquidus and solidus temperature, latent heat, and fraction solid and data smoothing, we selected several Data Acquisition Rates. A Number of Samples and Scan Rates were tried. In summary, the optimum combination is considered to be Group F as follows: Number of Samples is 20, Scan Rate is 1440, and Data Acquisition Rate is 72°C/s.

Table 4-1 Six classes of test conditions

Test Condition	Test Number	Mold Pre-heat Temperature	Pouring Temperature	Date Acquisition Rate
Group A (4 tests)	114 116 1002 1003	180 °C	800 °C	72=360/5
Group B (1 test)	1005	200 °C	800 °C	72=1440/20
Group C (3 tests)	1010 1011 1013	200 °C	800 °C	72=1440/20
Group D (3 tests)	1014 1016 1017	250 °C	800 °C	72=1440/20
Group E (10 tests)	1018 1019 1020 1021 1022 1023 1025 1026 1027 1028	375 °C	800 °C	144=1440/10
Group F (4 tests)	1029 1030 1032 1033	375 °C	800 °C	72=1440/20

Table 4-2 The summary of test results

Test	T_L (C)		Ts (C)		Cooling Rate(C/s)	Solidification duration (s)	Hot-Tearing Temp.(C)		Hot-Crack	AE Signals					Tear Surface
	theo.	exp.	theo.	exp.			Start	fs	Temp.(C)	Characteristic*	Hot-Tearing		Hot-Cracking		
											Energy	Ave. Freq. (kHz)	Energy	Ave. Freq. (kHz)	
114	659.0	657.0	<630.0	627.4	43.25	4.444	644.4	0.831	592.4	Two Zones, two peaks. tear is zone I, the first peak	1233	135	1679	114	Free Dendrite
116	659.0	659.1	<630.0	627.7	38.77	5.806	645.8	0.893	489.4	Three Zones, three peaks. tear is zoneII, second peak	1754	131	1129	126	Free Dendrite
1002	659.0	658.5	<630.0	628.6	27.90	6.529	650.2	0.887	603.5	Three Zones, three peaks. Hot-Tearing is second peak	989	137	778	124	Free Dendrites
1003	659.0	658.9	<630.0	629.5	23.33	3.987	646.1	0.929	558.7	Three Zones, three peaks. Hot-Tearing is second peak Hot-Cracking is third peak	871	128	1234	135	Free Dendrite Cracking
1005	659.0	659.1	<630.0	626.7	49.31	5.623	643.65	0.889	568.7	Three Zones, three peaks. Hot-Tearing is first peak	747	128	784	129	Free Dendrite
1010	659.0	658.8	<630.0	628.5	30.18	6.663	644.9	0.974	578.6	Three Zones, three peaks. tear is zone II, second peak	658	119	1071	145	95 % Free Dendrite 5 % Crack
1011	659.0	659.1	<630.0	628.0	36.24	5.970	648.2	0.795	617.6	Three Zones. four peaks tear is zone III, third peak	684	103	905	135	75 % Free Dendrite 25 % Crack
1013	659.0	659.0	<630.0	613.0	46.95	5.220	645.2	0.965	511.9	Four Zones, four peaks tear is zone II, second peak	633	118	839	133	95 % Free Dendrite 5 % Crack
1014	659.0	659.2	<630.0	627.3	33.95	5.164	650.7	0.853	565.23	Three Zones, three peaks. tear is zone II, second peak	776	121	1257	141	95 % Free Dendrite 5 % Crack
1016	659.0	659.0	<630.0	628.3	39.69	5.206	646.9	0.904	563.6	Three Zones, three peaks. tear is zone II, second peak	840	127	1190	136	95 % Free Dendrite 5 % Crack
1017	659.0	659.0	<630.0	616.3	32.41	7.675	647.8	0.816	572.3	Three Zones. Five peaks tear is zone II, second peak	673	115	969	134	95 % Free Dendrite 5 % Crack
1018	659.0	659.0	<630.0	628.6	30.83	9.615	653.8	0.882	560.3	Three Zones, three peaks tear is zone II, second peak	1105	129	1344	138	95 % Free Dendrite 5 % Crack
1019	659.0	658.9	<630.0	628.2	38.91	8.958	652.2	0.891	580.9	Three Zones, three peaks tear is zone II, second peak	956	127	1013	130	95 % Free Dendrite 5 % Crack

* Refer to Appendix I

Table 4-2 The summary of test results (continued)

Test	T_L (C)		Ts (C)		Cooling Rate(C/s)	Solidification duration (s)	Hot-Tearing Temp.(C)		Hot-Crack Temp.(C)	AE Signals					Tear Surface
	theo.	exp.	theo.	exp.			Start	fs		Characteristic*	Hot-Tearing		Hot-Cracking		
											Energy	Ave. Freq. (kHz)	Energy	Ave. Freq. (kHz)	
1020	659.0	658.7	<630.0	626.3	51.19	7.595	648.7	0.984	552.4	Three Zones, three peaks tear is zone II, second peak	679	111	3044	148	95 % Free Dendrite 5 % Crack
1021	659.0	658.3	<630.0	627.1	50.37	8.969	643.9	0.976	588.5 496.4	Three Zones, three peaks tear is zone II, second peak	742 4392	111 145	1428 1456	106 132	90-95% Free Dendrite 5-10% Crack
1022	659.0	634.8	<630.0	612.6	44.72	9.560	631.2	0.949	516.8	Three Zones, three peaks tear is zone II, second peak	2202	139	3009	141	95 % Free Dendrite 5 % Crack
1023	659.0	659.2	<630.0	628.1	33.02	9.584	653.8	0.824	607.3	Three Zones, three peaks tear is zone II, second peak	664	113	917	131	95 % Free Dendrite 5 % Crack
1025	659.0	658.8	<630.0	629.3	23.35	7.818	641.8	0.976	596.7	Three Zones, four peaks tear is zone II, second peak	687	113	1063	125	95 % Free Dendrite 5 % Crack
1026	659.0	658.7	<630.0	628.2	32.05	7.565	642.3	0.978	541.9	Three Zones, three peaks tear is zone II, second peak	730	101	810	125	90-95% Free Dendrite 5-10% Crack
1027	659.0	659.0	<630.0	628.1	26.40	8.903	642.0	0.996	558.1	Three Zones, three peaks tear is zone II, second peak	1046	126	1314	131	90 % Free Dendrite 10% Crack
1028	659.0	658.9	<630.0	628.7	30.42	7.929	644.6	0.985	530.0	Three Zones, three peaks tear is zone II, second peak	1499	134	803	111	80 % Free Dendrite 20% Crack
1029	659.0	659.1	<630.0	628.4	30.05	8.883	610.1	-	511.2	Three Zones, three peaks tear is zone II, second peak	1385	134	1532	140	95 % Free Dendrite 5 % Crack
1030	659.0	658.8	<630.0	628.8	26.66	9.256	652.7	0.963	568.3	Three Zones, three peaks tear is zone II, second peak	1011	133	1892	143	95 % Free Dendrite 5 % Crack
1032	659.0	658.8	<630.0	631.1	13.68	8.468	642.6	0.996	581.5	Three Zones, three peaks tear is zone II, second peak	2101	139	1508	140	95 % Free Dendrite 5 % Crack
1033	659.0	659.1	<630.0	629.7	20.32	8.648	636.2	0.998	533.9	Three Zones, three peaks tear is zone II, second peak	1494	143	1639	139	90-95% Free Dendrite 5-10% Crack

* Refer to Appendix I

Table 4-3 The summary of the results for grain refined tests

	Test Number	T_L (C) theo.	T_L (C) exp.	Ts (C) theo.	Ts (C) exp.	Cooling Rate(C/s)	Solidification duration (s)	Hot-Tearing Temp.(C) Start	Hot-Tearing Temp.(C) fs	Hot-Crack Temp.(C)	AE Signals Characteristic*	Hot-Tearing Energy	Hot-Tearing Ave. Freq.	Hot-Cracking Energy	Hot-Cracking Ave. Freq.	Tear Surface
No-grain refiner	1034	659.0	658.8	<630.0	628.3	33.42	9.592	648.1	0.951	577.3	Two zones, two peaks Hot-Tearing is first peak Hot-cracking is second peak	1311	(kHz) 136	779	(kHz) 127	90-95% Free Dendrite 5-10% Crack
	1035	659.0	659.2	<630.0	627.9	34.86	8.350	650.1	0.897	575.2	Three zones, three peaks Hot-Tearing is second peak Hot-cracking is third peak	597	106	603	110	90-95% Free Dendrite 5-10% Crack
	1040	659.0	659.3	<630.0	628.7	29.63	10.149	641.2	0.964	601.5	Three zones, three peaks Hot-Tearing is second peak Hot-cracking is third peak	535	114	691	120	80% Free Dendrite 20% Crack
	1041	659.0	659.5	<630.0	629.3	25.16	8.787	647.3	0.941	571.1	Three zones, three peaks Hot-Tearing is second peak Hot-cracking is third peak	643	123	677	127	90% Free Dendrite 10% Crack
	1042	659.0	658.8	<630.0	628.2	32.99	8.537	637.8	0.989	578.7	Two zones, two peaks Hot-Tearing is first peak Hot-cracking is second peak	595	116	788	129	75% Free Dendrite 25% Crack

		Test Nomber	T_L (C) theo.	T_L (C) exp.	Ts (C) theo.	Ts (C) exp.	Cooling Rate(C/s)	Solidification duration (s)	AE Event "I" Temp.(C) Start	AE Event "I" Temp.(C) fs	AE Event "II" Temp.(C) Start	AE Event "II" Temp.(C) fs	AE Signals Characteristic*	AE Event "I" Energy	AE Event "I" Ave. Freq.	AE Event "II" Energy	AE Event "II" Ave. Freq.	Tear Surface
with grain refiner	6 ppm	1043	659.0	659.2	<630.0	628.3	30.89	7.995	637.2	0.991	592.3		Two zones, two peaks no tear, no crack	405	(kHz) 93	363	(kHz) 83	-
		1044	659.0	659.4	<630.0	628.2	30.52	8.773	619.6	-	579.9		Two zones, two peaks Second peak is very small no tear, no crack	339	74	302	65	-
		1046	659.0	659.4	<630.0	629.2	25.71	10.452	647.9	0.941	601.1		Two zones, two peaks no tear, no crack	468	101	413	93	-
	18 ppm	1039	659.0	658.9	<630.0	630.7	15.83	9.132	604.4	-	563.4		One zone, one peak no tear, no crack	383	80	392	89	-
		1045	659.0	659.1	<630.0	628.2	30.36	9.066	647.1 (AE Event II)	0.911	564.7 (AE Event III)		Three zones, one continum peak no tear, no crack	410	92	431	100	50% Free Dendrite 50% Crack
		1047	659.0	659.2	<630.0	628.3	29.57	10.287	640.0	0.952			one zone, one peak no tear, no crack	453	87	-	-	-
	35 ppm	1038	659.0	659.5	<630.0	628.3	29.94	8.967	644.2	0.955	615.1		Two zones, two peaks no tear, no crack	449	99	380	89	-
	50 ppm	1036	659.0	659.2	<630.0	628.9	24.74	13.923	-	-	607.0		One zone, one peak small Hot-cracking	-	-	584	119	-
		1037	659.0	659.4	<630.0	629.4	22.63	15.534	638.2	0.997	606.5		Two zones, two peaks no tear, no crack	369	89	425	97	-

* Refer to Appendix II

Secondly, a number of experiments were repeated with non-grain refined and grain-refined AA1050 alloys to investigate the incidence of hot-tearing and the effects of grain refining. The test conditions were the same as the conditions of preliminary tests in group F (see also Table 4-1). Appendix II shows the test results where AE signals and the cooling/solidification curves are superimposed. The test results obtained to date are summarized in Table 4-3.

4.2 Discussion

4.2.1 Information from Cooling Curve

Fig. 4.1 shows a typical cooling curve, its first derivative, and fraction solid from our experimental result. It shows various solidification stages and activities. T_f is the equilibrium freezing temperature of 660°C. Below T_f , solid is the stable phase and nucleation is expected to occur readily because solid has a lower free energy than liquid. However, when a liquid is cooled to a temperature below T_f, it does not spontaneously crystallize: a certain degree of supercooling and a certain nucleation period is necessary before solidification starts. For a metal or a single-phase alloy, the nucleation typically begins at a certain degree of supercooling ($\Delta T = \Delta Tn$) which is generally small (Fig. 4.1 a). The first solid fraction (fs) forms at this point (Fig. 4.1 c). Immediately after the supercooling reaches its minimum value as seen in Fig. 4.1 a, the temperature increases back to a level that is slightly below the equilibrium freezing point. However, since a small supercooling is always required to drive the transformation in the direction of solidification, the temperature does not completely return to its original level which is at T_f.

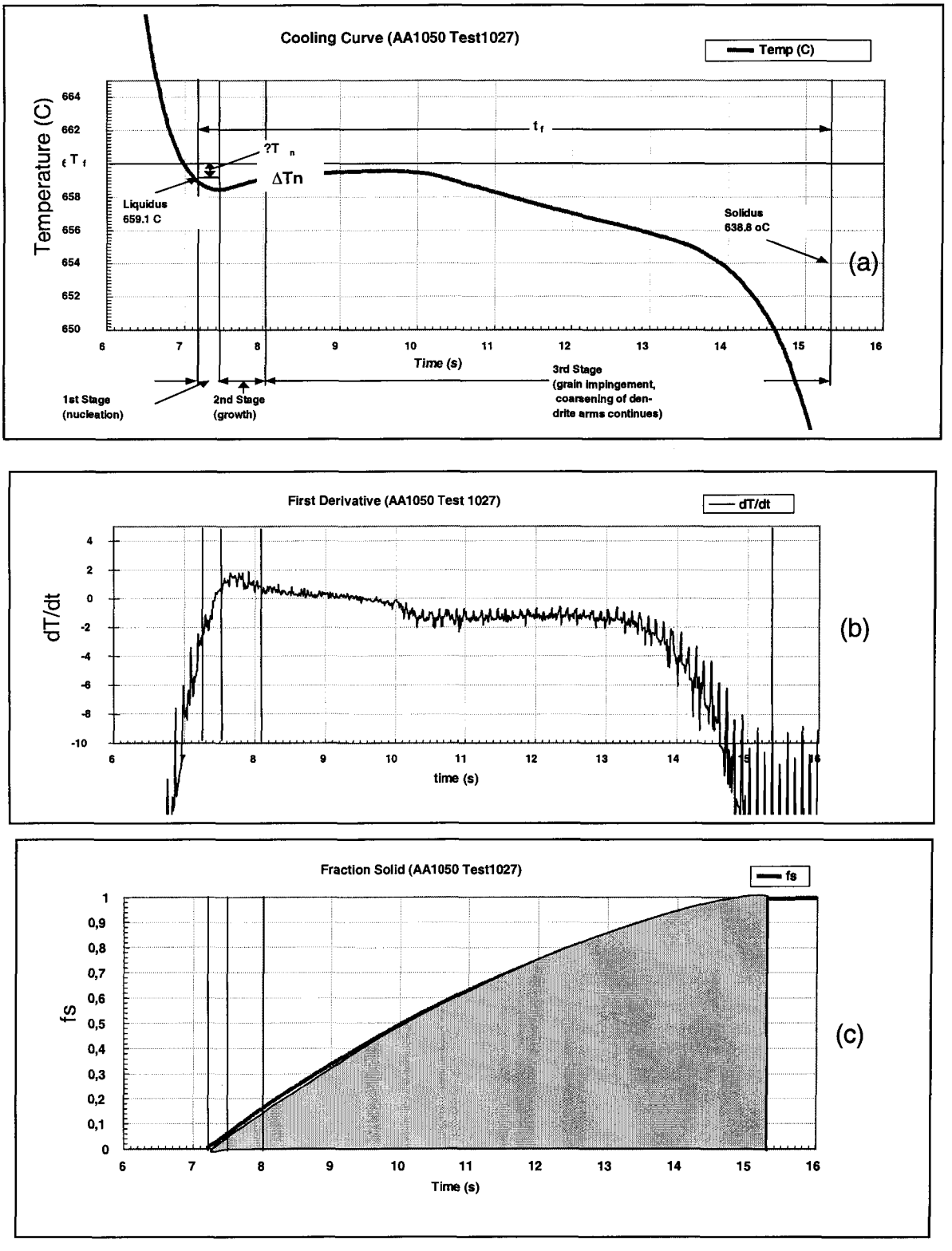

Fig. 4.1 Thermal history of AA1050 solidification from test1027; a) Cooling curve, b) First derivative, c) Fraction solid.

Therefore, the first stage of solidification is controlled by nucleation and it establishes the final size and number of grains in castings. The second stage of solidification starts after the system temperature rises above the nucleation temperature during recalescence. This stage is controlled by growth, and the number of grains remains constant while the solidification continues with dendrites growing and dendrite arms coarsening. In the last stage of solidification, growth stops due to grain impingement, and the coarsening of dendrite arms continue. Hot-tearing occurs in the latter part of this stage, close to completion of solidification, at or just above the solidus temperature. Hot-cracking occurs after completion of solidification, when the material is entirely solid below the solidus temperature.

4.2.2 Acoustic Emission Signals

The superposition graph shows a typical test result of acoustic emission signals and cooling curve in Fig. 4.2. The AE from the solidifying test casting was of the continuous type. This type of emission is known to occur when a large number of events occur simultaneously in the entire volume of the test material. It is clear that AE signals with high peak voltage, which were never detected in the early stage of solidification, were detected at the end of solidification in all of the castings and in the late stages of solidification in the castings having significant hot-tearing or cracking. There are three solidification zones in each test (Fig. 4.2 c); three high voltage peaks may represent three solidification events. The first peak of zone **I** represents the interdendritic friction as has been typically attributed to by earlier researchers (Purvis et al) [60]. Hot- tearing occurs at

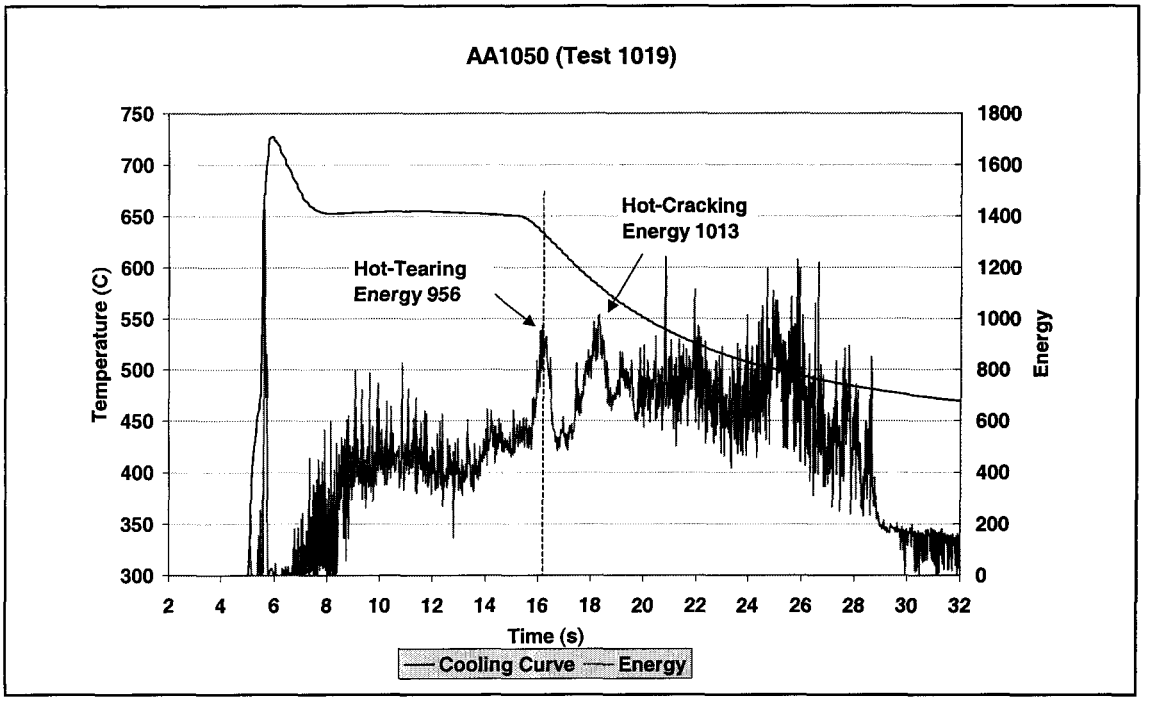

Fig. 4.2 (a) A typical superposition graph of acoustic emission energy and cooling curve obtained from AA1050 (test 1019);

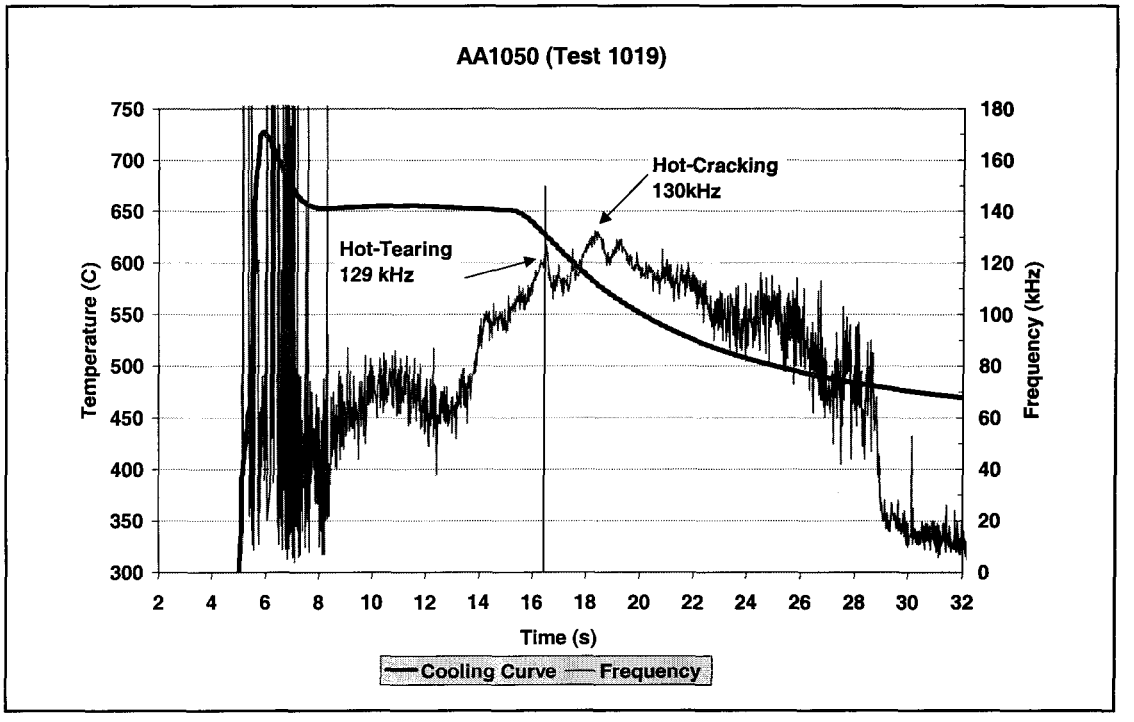

Fig. 4.2 (b) A typical superposition graph of acoustic emission average frequency and cooling curve obtained from AA1050 (test 1019);

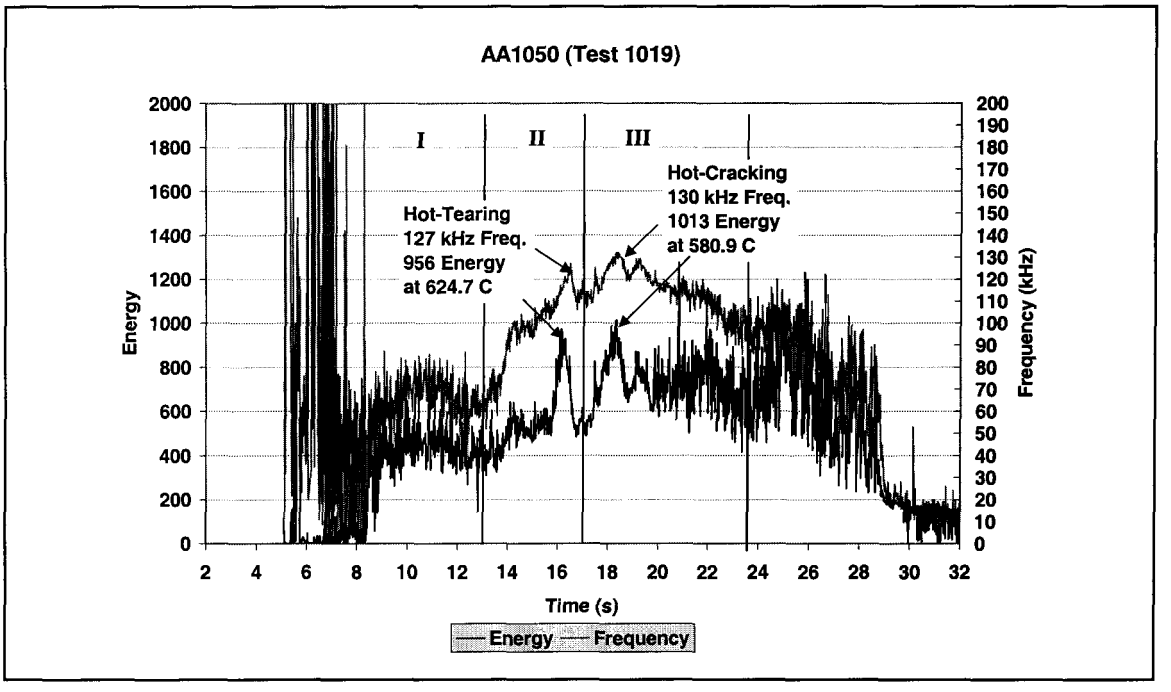

Fig. 4.2 (c) A typical superposition graph of acoustic emission average frequency and energy obtained from AA1050 (test 1019);

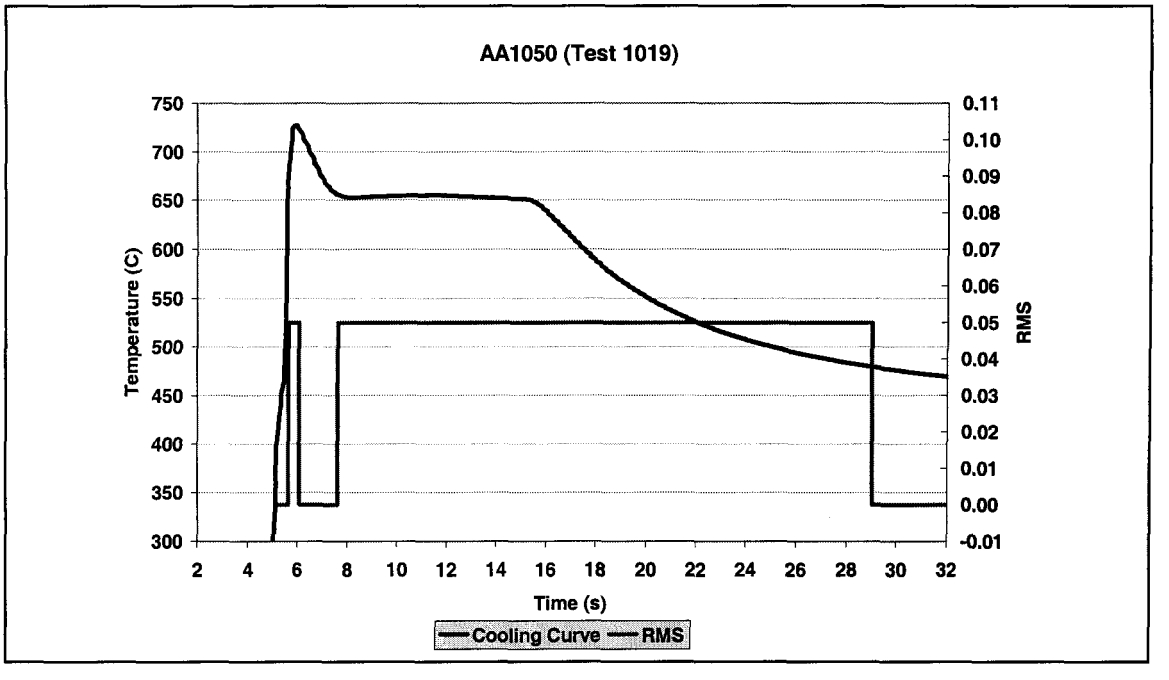

Fig. 4.2 (d) A typical superposition graph of acoustic emission RMS and cooling curve obtained from AA1050 (test 1019).

the second peak in zone **II**. We know this because comparison of castings with hot-tearing and without hot-tearing indicated the presence of a peak in zone II with a characteristic frequency of >130kHz when there is a hot-tearing [61]. The rising of the AE signal represents the beginning of hot-tearing. In the third zone where solidification has been completed and cooling of the casting begins, the characteristic peak has been obtained in castings that exhibit hot-cracking (as characterised by fracture surface analysis). In the third peak in zone **III**, the strain energy released by hot-cracking is greater than that released by hot-tearing. When hot-tearing events occurred, the AE energy was over 600, the average frequency was about 125 ±15kHz, and the RMS has an evident pulse as shown in Table 4-2. For hot-cracking events, the AE energy was over 650 , the average frequency was about 128 ±17kHz, and the RMS also has a evident pulse in zone **III**. Comparing with hot-tearing event, all of Energy of hot-cracking is larger for each test, but the average frequency is not at all larger.

4.2.3 Fraction Solid Evolution

As shown in Fig. 4.3, the liquidus and solidus temperatures are determined from the cooling curve and its first derivative. Further the latent heat and fraction solid during the solidification process are calculated. Combined with recorded AE signals, the temperature and the time when each AE event occurred can be known, thereby the fraction solid of each corresponding solidification activity can be determined. Therefore, the fraction solid of hot tearing can be determined for every test; this is summarized in Table 4-2.

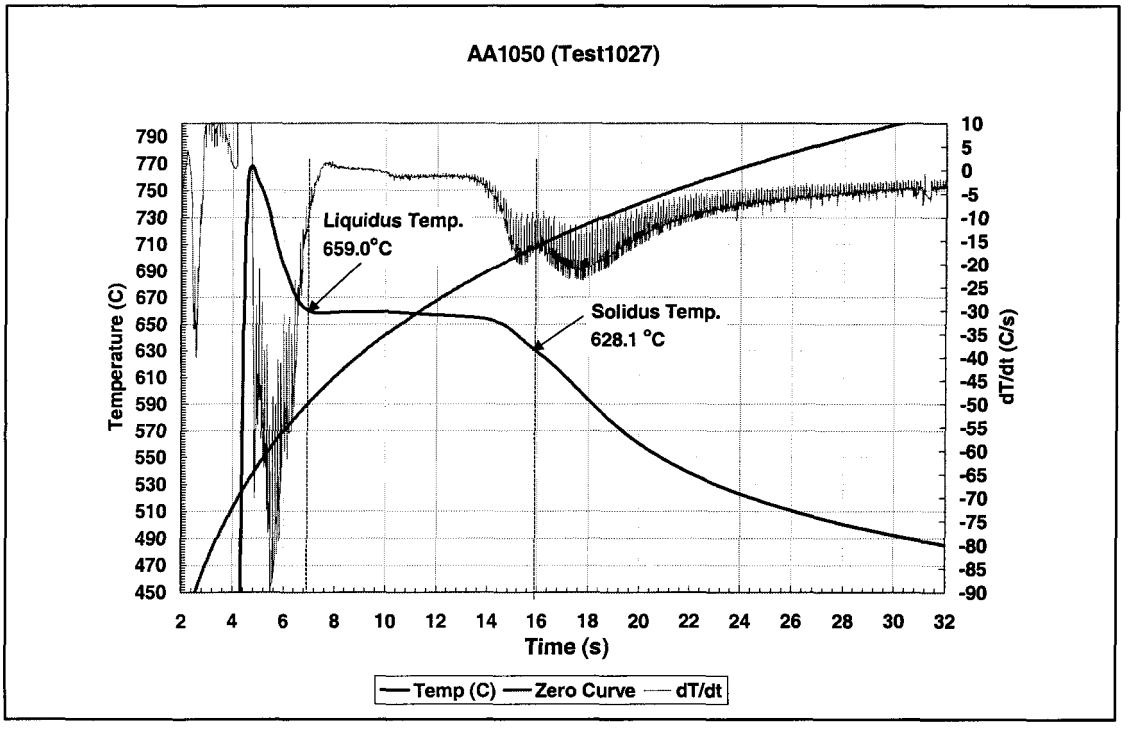

Fig. 4.3 (a) A typical graph of cooling curve obtained with its first derivative and null curve from AA1050 (test1027);

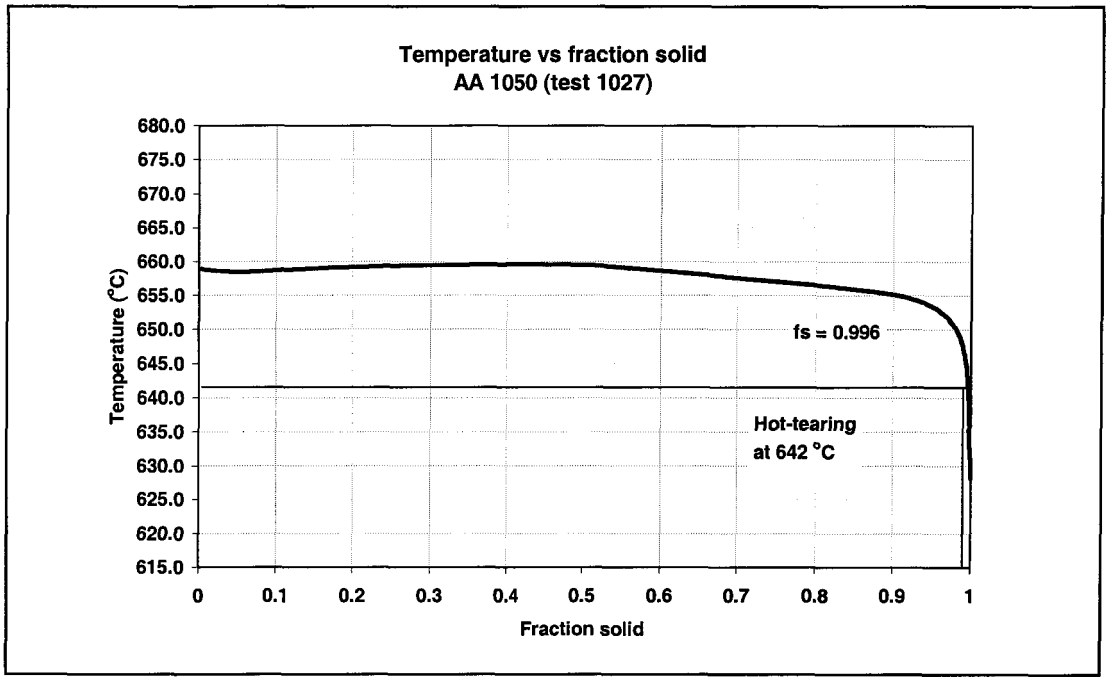

Fig. 4.3 (b) A typical graph of fraction solid at the time of hot-tearing occurred with temperature from AA1050 (test1027).

From the summary of table 4-2, the test results show that liquidus temperature is about 659°C, and the solidus temperature is under 630°C. This is in accordance with the results obtained by Backerud et al. [62]. They determined the liquidus and the solidus temperatures of AA1050 with increasing cooling rate as shown in Table 4-4. In our experiments the solidus temperature is under 630 °C because the cooling rates are always higher than 20 °C/s. Thus, the values of the solidus temperature gets smaller as the cooling rate goes up. Combining the information given in Table 4-4, a relative curve with solidus temperature and cooling rate from our experiments can be shown in Fig. 4.4.

Table 4-4 The liquidus temperature & the solidus temperature with different cooling rate for AA1050 (by Lennart Backerud et al. [62])

Cooling Rate (°C/s)	0.4	1.2	4.2	18
Liquidus Temp. (°C)	659	659	659	659
Solidus Temp. (°C)	642	638	636	630

It is of interest to note that the temperature when hot-tearing begins is not the same in each test, it is between 640°C~650°C. The fraction solid is also different when hot-tearing is occurring; between 0.795~0.998. But their trends are consistent; namely it is shown in Fig. 4.5, that the later the hot-tearing occurs, the nearer to the solidus is the temperature of hot-tearing, and the closer it is to 100 percent fraction solid. In our experiments, all results proved that hot-tearing occurs just prior to the completion of

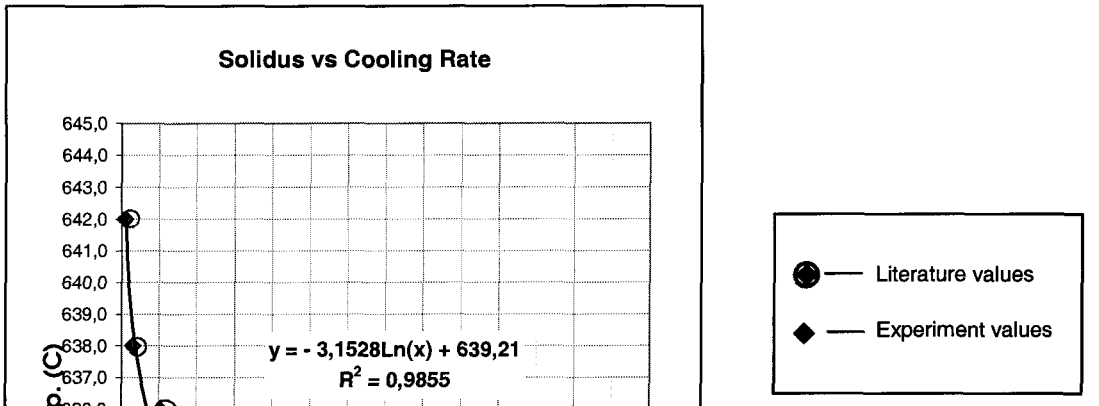

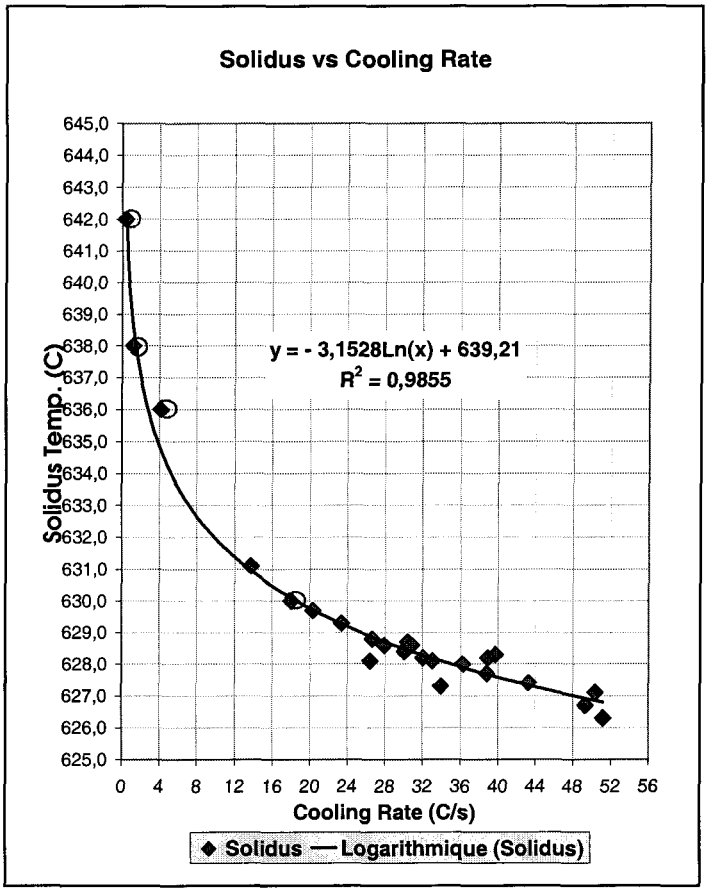

Fig. 4.4 Experimental variation of solidus temperature with cooling rate.

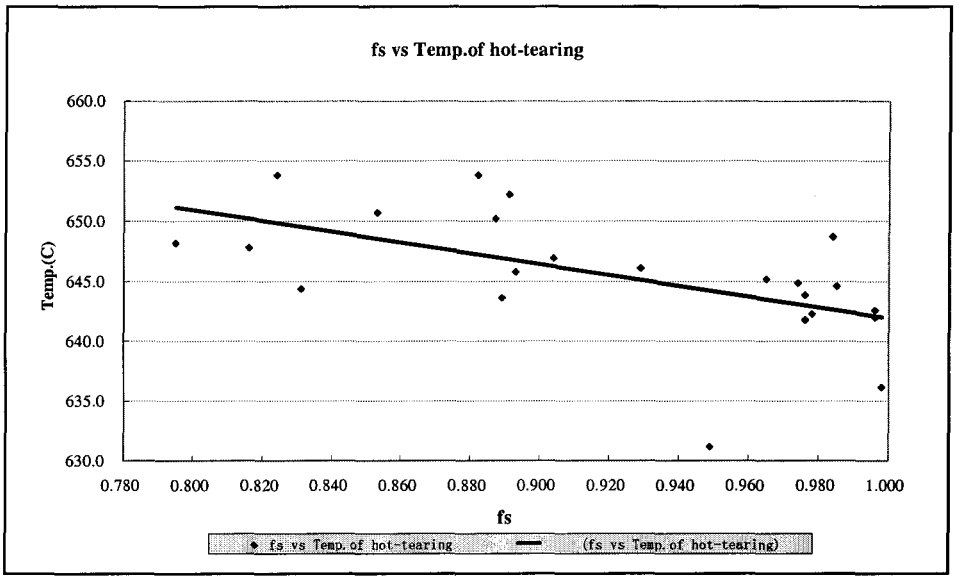

Fig. 4.5 The trends of fraction solid vs the temperature of hot-tearing when hot-tearing is occurring.

solidification.

4.2.4 Fracture Surface Analysis

4.2.4.1 Visual Observation

The hot-tearing fracture of the test rings for AA1050 is shown in Fig. 4.6. It can be seen that the fracture is a jagged, branched crack.

It also can be observed that the most fracture locations(≥ 80%) are at the same place, near the pouring entry point, where the final freezing zone of the solidifying casting is found (Fig.4.7).

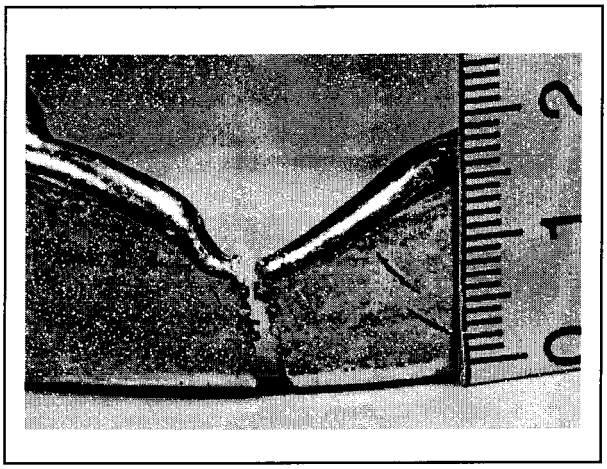

Fig. 4.6 The Hot-Tearing Fracture of the Test Rings for AA1050.

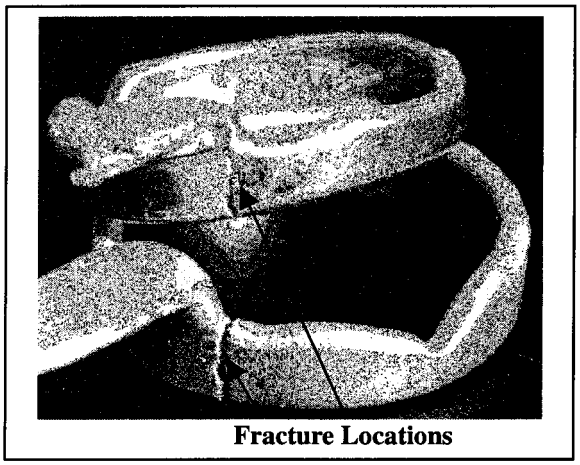

Fig. 4.7 Fracture Locations in most of the Test Rings.

4.2.4.2 Distinguishing between the Surface of Hot-Tearing and Hot-Cracking

It is observed that some portions are completely broken, and some portions are partially broken with a little bit of contact in some test castings. Therefore, to analyze the

fracture surface, it is important to distinguish between the completely broken portions by hot-tearing from the parts intentionally separated by us after the casting has reached and stayed at room temperature.

After both parts were carefully marked in the surface of samples, the fracture surface analysis was carried out with completely and partially broken test rings under a scanning electron microscope (SEM). The results are presented in Table 4-2.

Fig. 4.8 shows the SEM fractograph of the fracture surface of test ring for AA1050, which is the part of surface separated manually at room temperature to expose the partial hot-tear surface. It is seen that dimples, characteristic of a ductile fracture, are present in

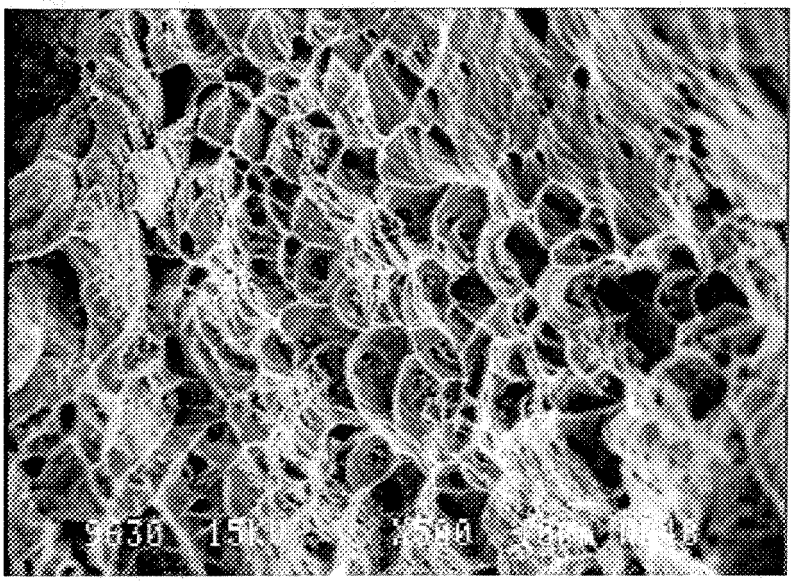

Fig. 4.8 SEM fractograph showing formation of dimples under conditions of tension.

the separated surface under conditions of tension. This is the main difference from a hot-tearing surface.

4.2.4.3 SEM Fractographs of Hot-Tearing Surfaces

The SEM of fracture surface obtained from the hot-tearing test 1032 for AA1050 is shown in Fig.4.9. It is quite obvious that the fracture propagates along the dendrite boundary interface, which further confirms the columnar mode of solidification as shown in Fig.4.10. It can be seen that the growing crystals followed the direction from inside to outside of the casting ring. This is due to the structure of the test mold, which consisted of steel concentric core and insulating material B3 outside mold, and which promotes directional solidification.

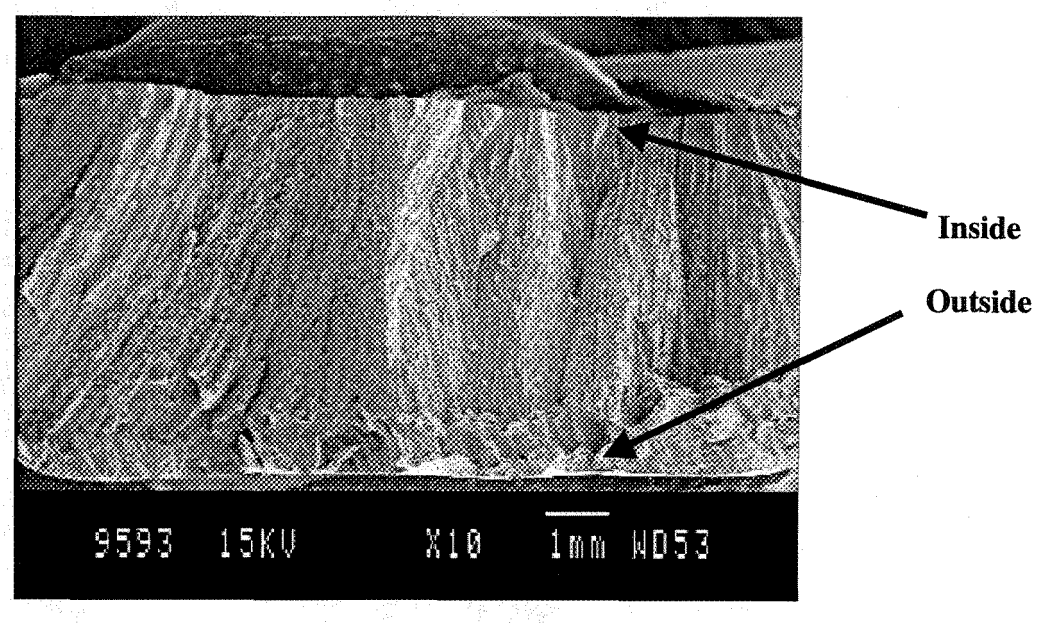

Fig. 4.9 The SEM of fracture surface obtained from the hot-tearing test 1032 for AA1050.

A few SEM fractographs of the typical torn samples in these series of experiments are presented in Fig. 4.11 ~ Fig. 4.15. These photographs show free dendrites (Fig. 4.11)

Fig.4.10 The fractograph of the casting ring from test 1032.

and columns (Fig. 4.12) on the fracture surface which indicates the presence of a hot-tearing defect, rather than simply a hot-crack of the solid. The existence of small regions of line of contact and the row of dendrite arms, which have ruptured under the stress, were also revealed (Fig. 4.13). The clearly discernible dendrite arms with smooth surfaces show that liquid metal was present at the time of the occurrence of the breakage. The interesting feature is that some small dimples and forks on the columns are evident in the Fig. 4.14 and Fig. 4.15. These small dimples and forks on the columns can be the evidence of contacts between solidified dendrites prior to hot-tearing. This indicates the points where separation happened after the dendrites formed an interconnected network while hot-tearing occurred. The dimples and forks on the columns imply that hot-tearing occurred due to overstress of the interconnected dendrites at points of contact.

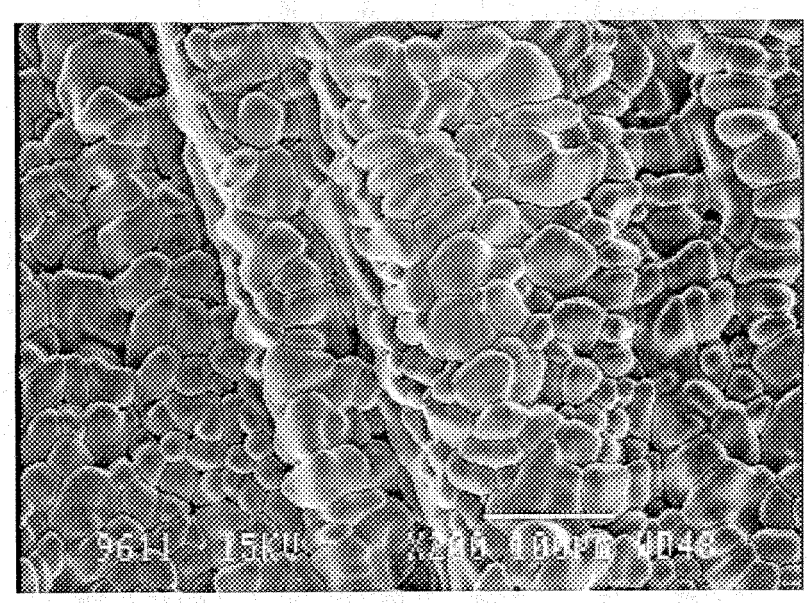

(a)

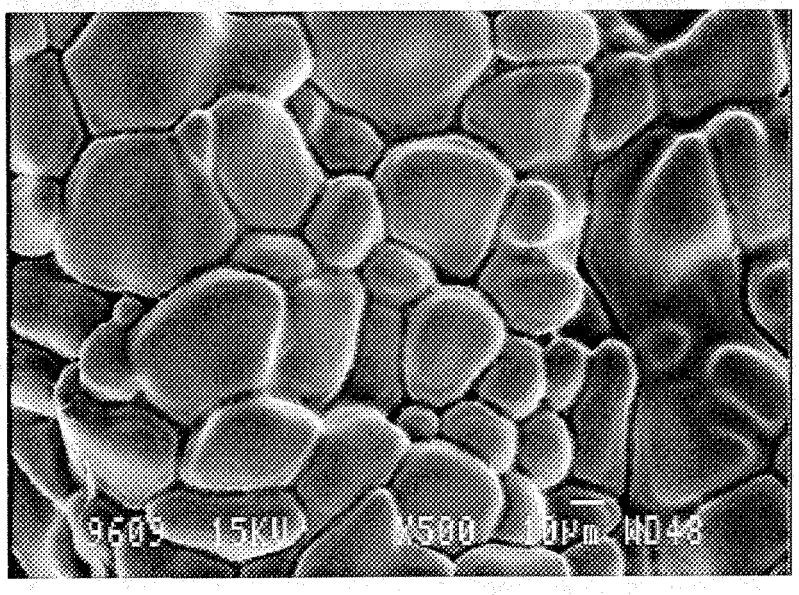

(b)

Fig. 4.11 SEM of a typical fracture surface obtained from the hot-tearing experiments test 1010 for AA1050: (a) 200X magnification; (b) 500X magnification.

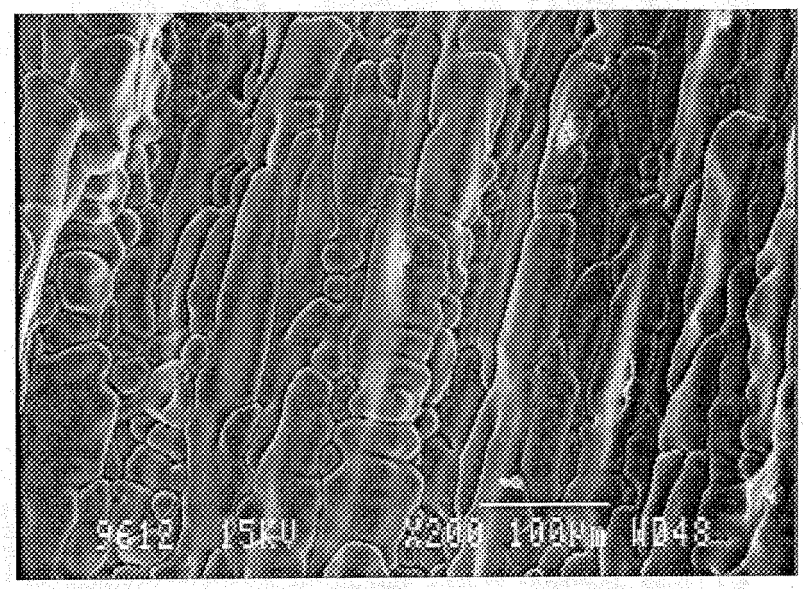

(a)

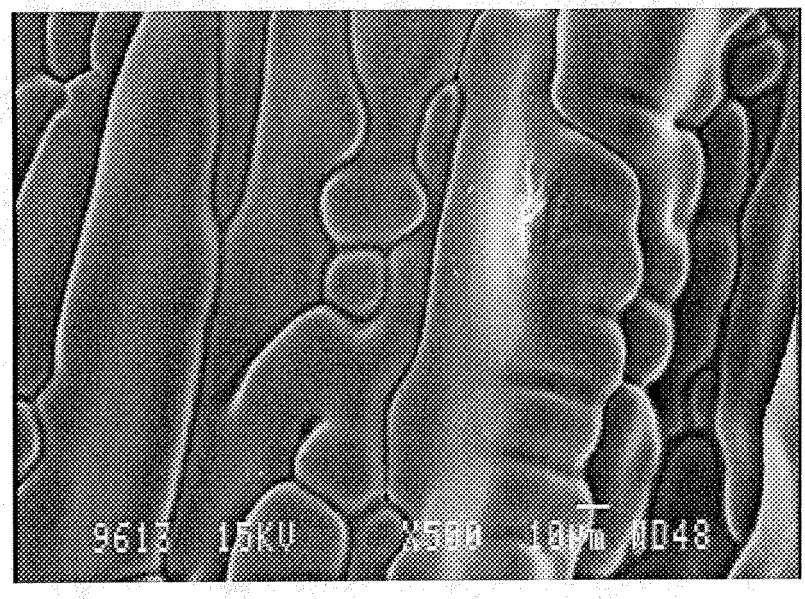

(b)

Fig. 4.12 SEM of a typical fracture surface obtained from the hot-tearing experiments test 1010 for AA1050: (a) 200X magnification; (b) 500X magnification.

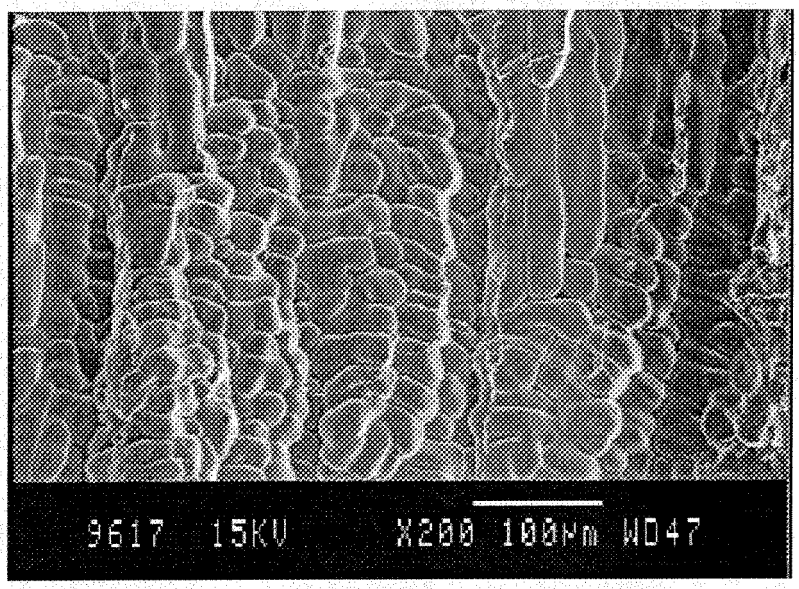

(a)

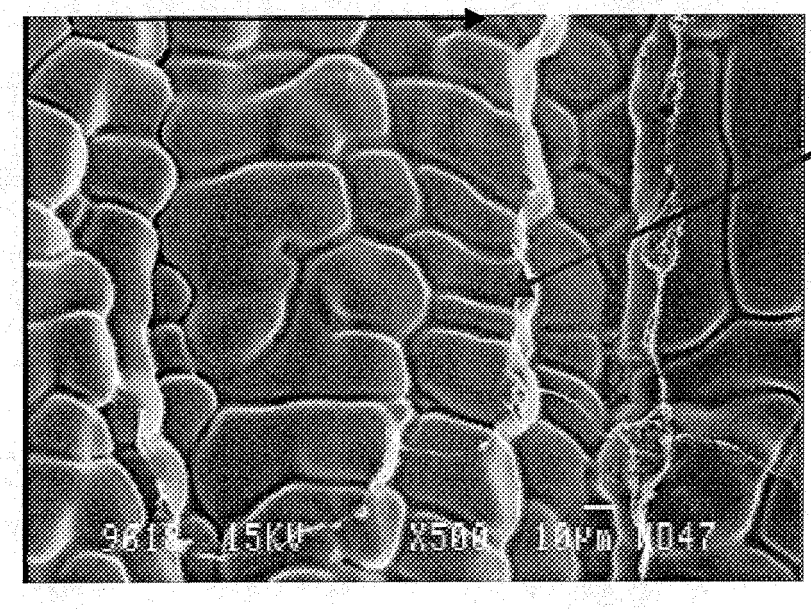

(b)

Fig. 4.13 SEM of a typical fracture surface obtained from the hot-tearing experiments (test 1013) for AA1050, which shows fracture of the line of contact of row of dendrite arms: (a) 200X magnification; (b) 500X magnification.

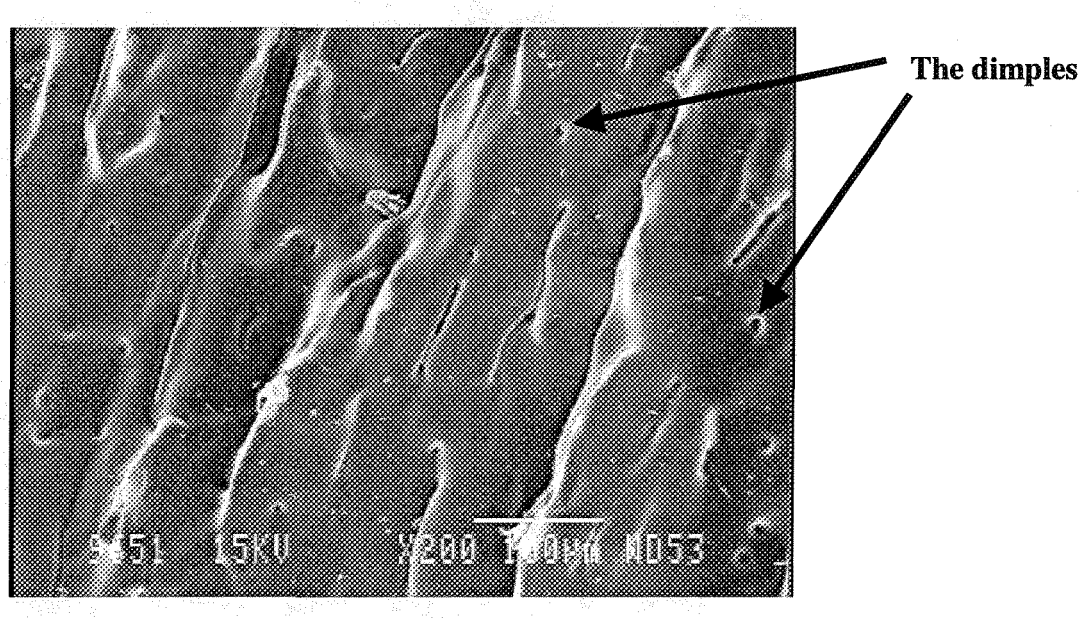

Fig. 4.14 SEM of hot-tearing surface of test 1020 for AA1050 with 200X magnification.

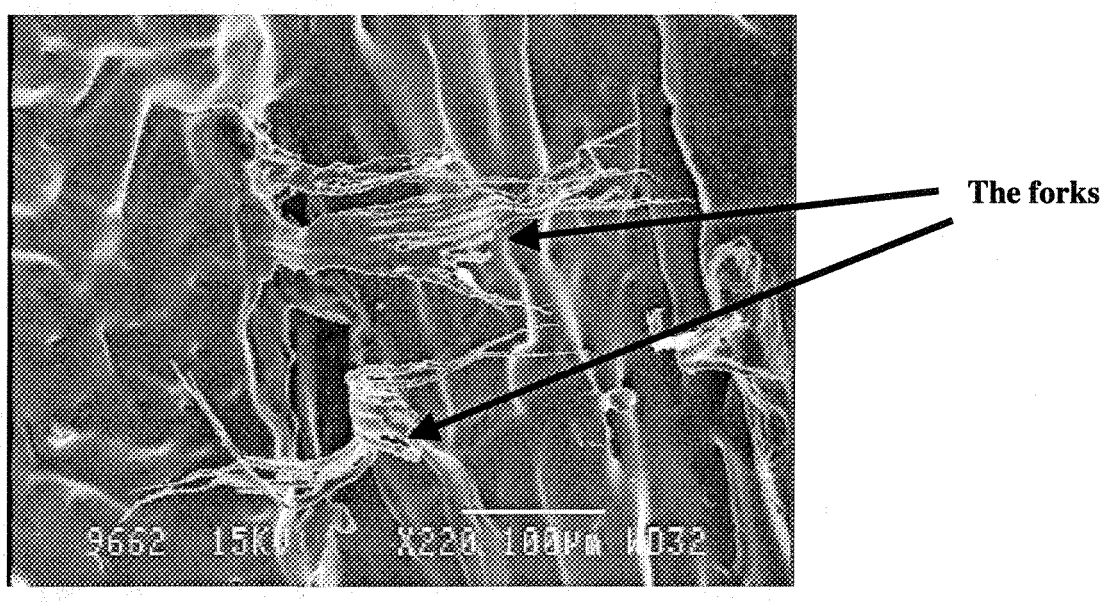

Fig. 4.15 SEM of hot-tearing surface of test 1020 for AA1050 with 220X magnification.

4.2.4.4 Comparing both Sides of the Fracture Surface

Fig. 4.16, 4.17 and 4.18 show a series of SEM photos of hot-tearing surface from one of the test ring samples (test 1035). The first picture shows the whole surface, and the others show the details at different locations in the sample (5 for the inside area and 3 for the outside area). Comparing the inside and the outside areas, it can be observed that the outside area is dominated by free dendrites. However, in the inside area, some ruptured dendrites were observed, which were connected to other dendrites before hot-tearing took place. This indicates that the solidification of inside parts is more advanced than outside parts when hot-tearing occurred in the casting ring. It can be considered that hot-tearing occurrence is usually accompanied by breaking of contacts between the dendrites. A number of samples were investigated to compare both sides of fracture surface by SEM examination and all gave similar results.

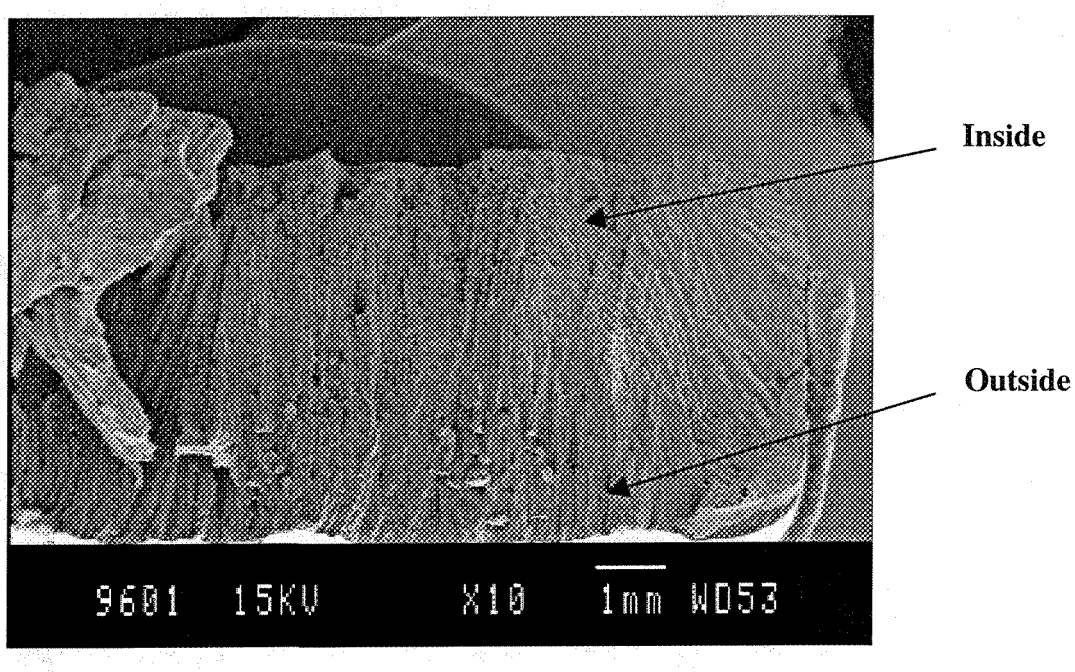

Fig.4.16 SEM of hot-tearing surface of test 1035 for AA1050: (Whole surface);

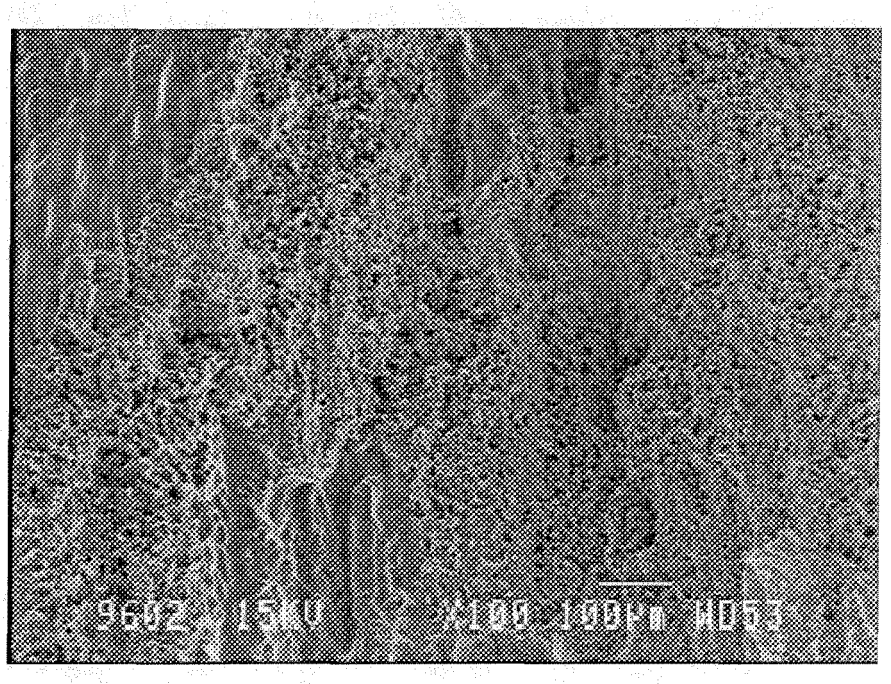

Fig. 4.17 SEM of hot-tearing surface of test 1035 for AA1050, which shows that some connected dendrites were ruptured when hot-tearing occurred: a) Inside area with 100X magnification;

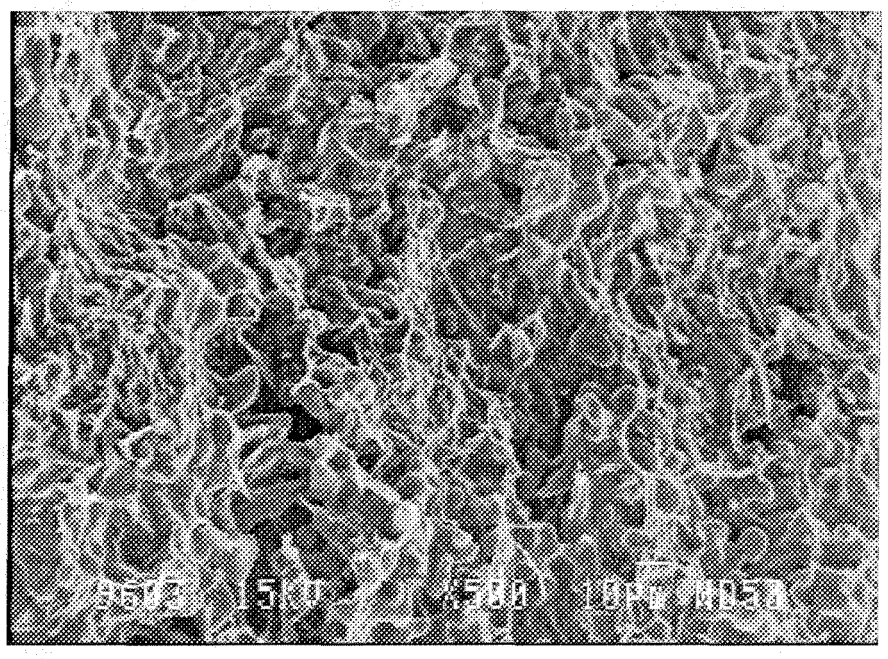

Fig. 4.17 SEM of hot-tearing surface of test 1035 for AA1050, which shows that some connected dendrites were ruptured when hot-tearing occurred: b) Inside area with 500X magnification;

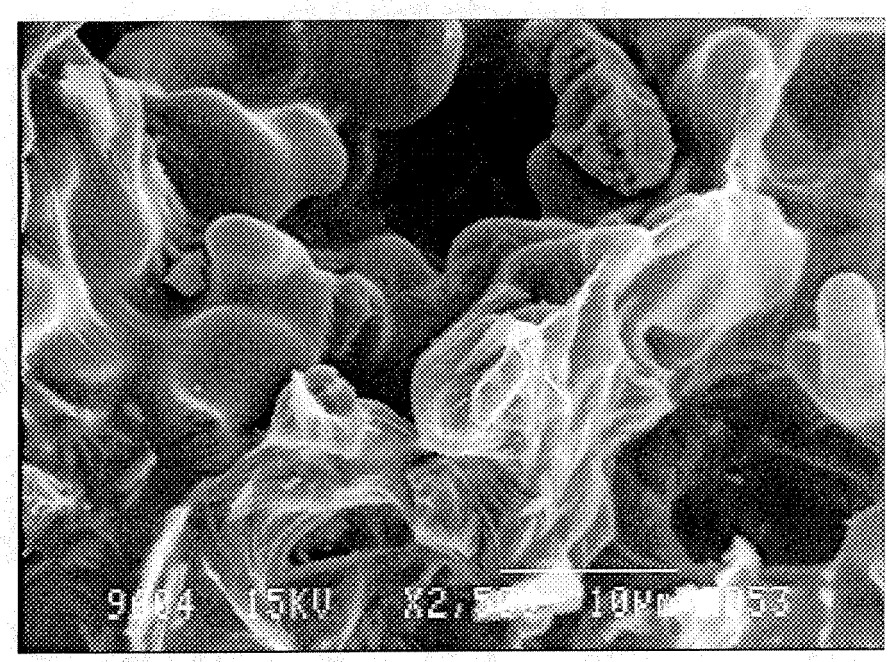

Fig. 4.17 SEM of hot-tearing surface of test 1035 for AA1050, which shows that some connected dendrites were ruptured when hot-tearing occurred: c) Inside area with 2500X magnification.

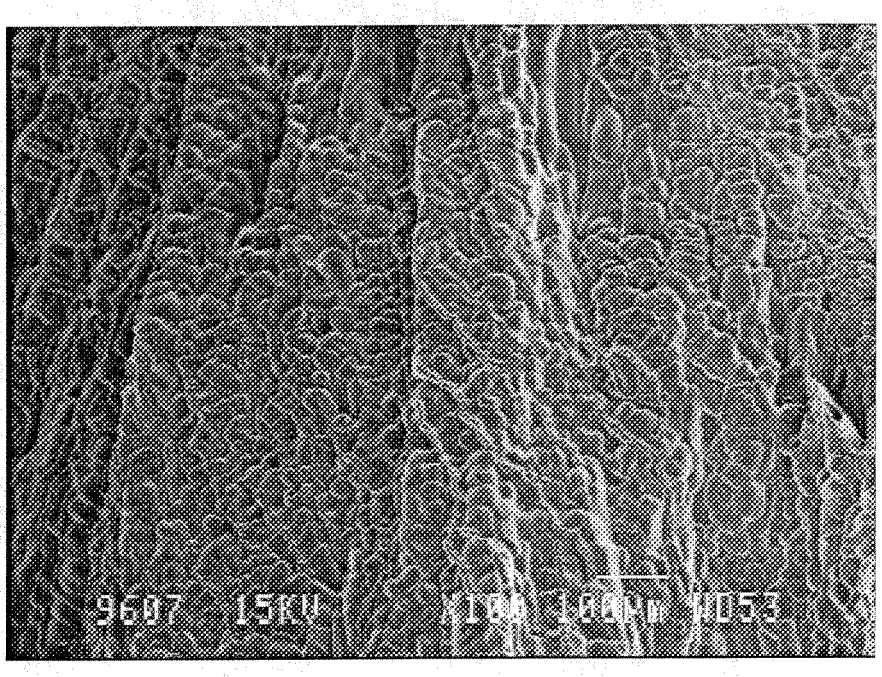

Fig. 4.18 SEM of hot-tearing surface of test 1035 for AA1050, which shows that free dendrites with liquid film dominated the outside area: (Outside area)

4.2.5 In-situ Monitoring of Hot-Tearing Development

It is known that the difference in the definition of hot-tearing and hot-cracking is that hot-tearing is a fracture occurring above the solidus temperature while hot-cracking occurs below the solidus temperature when the material is entirely solid [65].

In the present experiments, this identification is done through observing the AE signal waveform (such as in Appendix II: test114, 1003, 1010, 1021, 1022, 1025, 1029-1033, 1040, 1041, and test 1042). It should be noted that there is not an evident wave trough between the two peaks of the AE waves representing hot-tearing and hot-cracking in many tests. It is shown in Fig. 4.19, which is an example of this type of test result. These facts suggest that the first high voltage peak of the AE continuous wave accompanies the fracture of the test ring which begins in the semi-solid state when rigid primary dendrite networks are formed. As the stress continues inside the ring mold it is excessively restrained. The fracture progresses and develops, until it becomes a complete tear, thereby an AE is released from the breakage increases to the largest peak. Then, freezing continues until the metal is entirely solid. Hot-cracking occurs after solidus temperature due to the presence of coherency in the metal and some elasticity during the generation of thermal strains. In this situation, developed AE activity continues to occur and increases again to a peak voltage. Therefore it is considered that the fracture continues to spread, developing from the event of hot-tearing to hot-cracking. In the inside area hot-cracking is a continuance or development of hot-tearing. The AE waveform analysis demonstrates that in the 1050 alloy both tearing and cracking is a continuous process of the fracture.

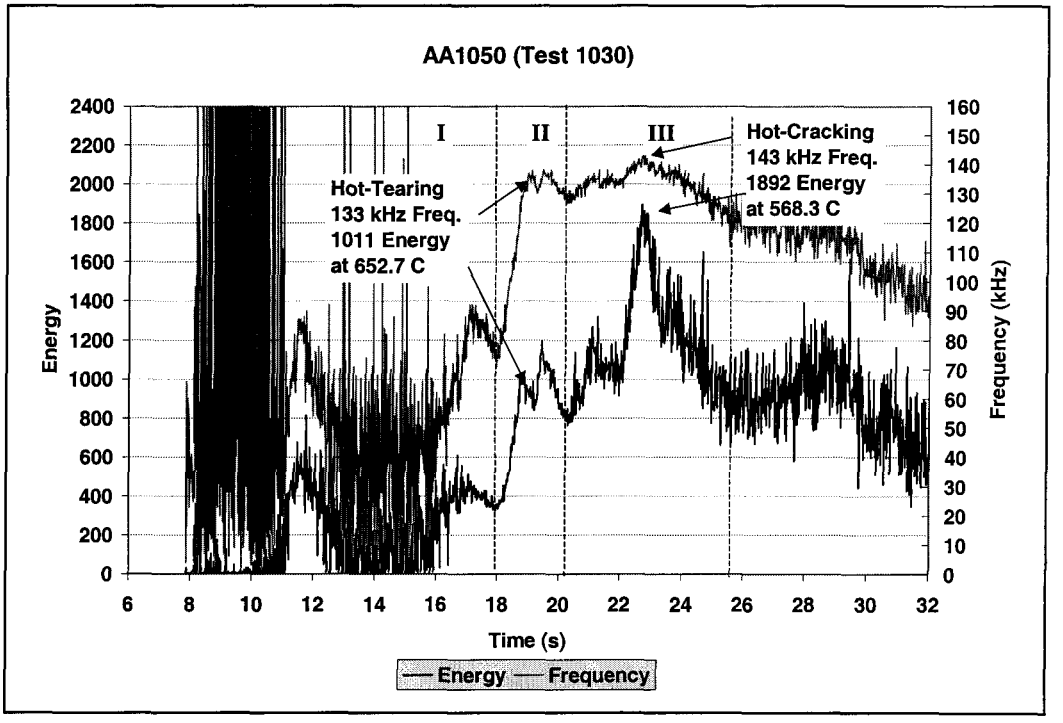

Fig. 4.19 a) AE energy and average frequency from AA1050 test 1030;

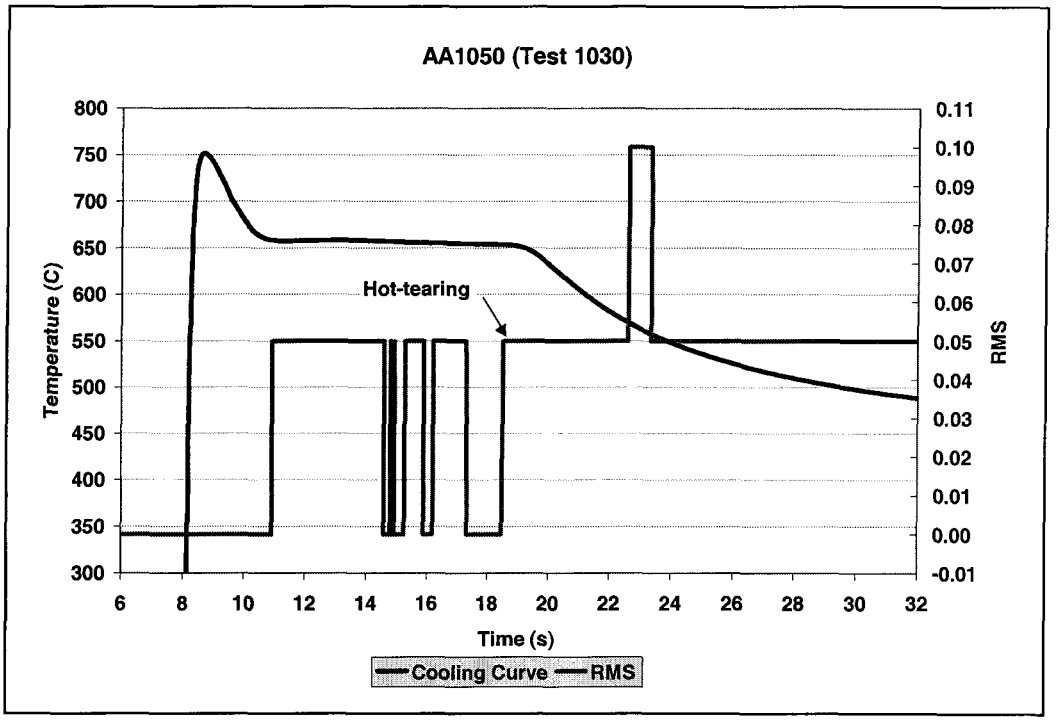

Fig. 4.19 b) AE RMS superpose cooling curve from AA1050 test 1030.

4.2.6 Comparison of Results with and without Grain-Refiner

It is well-known that aluminum alloys are usually more prone to hot-tearing when they have coarse columnar grains than the alloys with fine equiaxed grains. Grain refinement can reduce the hot-tearing tendency of alloys [8]. An easy way to control the grain size is the addition of grain refiners. Grain size is a function of the type and amount of grain refiners added. The most widely used grain refiners are master alloys of titanium, or of titanium and boron. In order to compare the hot-tearing behavior of AA1050 alloy with different grain size, an investigation into the energy voltage of the acoustic emission signals released with grain refined and non grain-refined alloys was done. The chemical composition of added material used is shown in Table 4-5. The test results with different amounts of Ti and B are shown in Table 4-3 and Appendix II.

Table 4-5 Chemical composition of grain refiner material

Material	Elements of Alloys (%)				
W72946	Fe	Ti	B	V	Si
	0.18	5.1	1.0	0.01	0.03

Fig. 4.20 is a series of AE signal graphs from Appendix II. It is observed that there is a reduction of AE energy released from interdendritic separation when the amount of grain refiner is increased.

(a) Without grain refinement, from the continuum wave peak of AE signal detected it can be concluded that the event is hot-tearing. This is because the AE energy is 643, and

the average frequency is 123 kHz; it is apparent that hot-tearing started at 647.3°C, and the fraction solid was 0.941.

(b) With a grain-refinement addition of 6 ppm B and 30 ppm Ti, the AE event detected that the energy was 468 and the average frequency was 101 kHz. It is considered

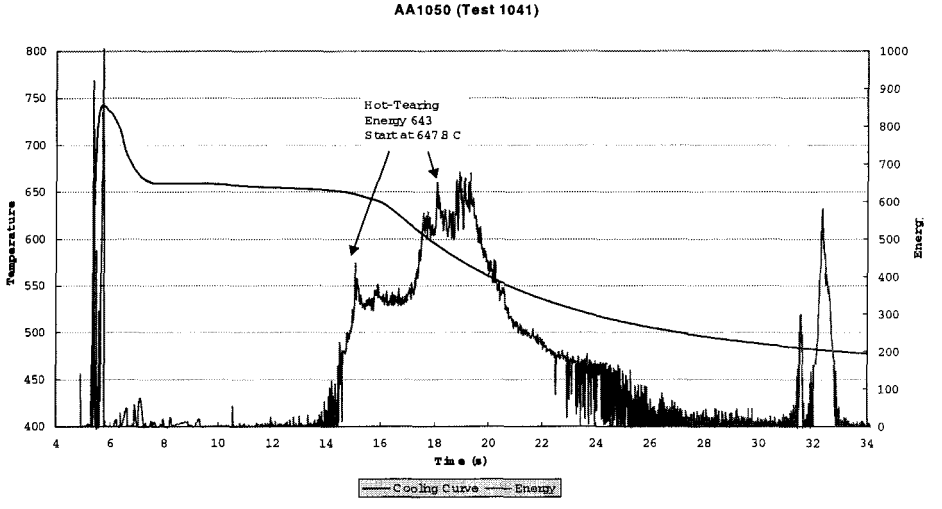

(a) With no-grain refiner

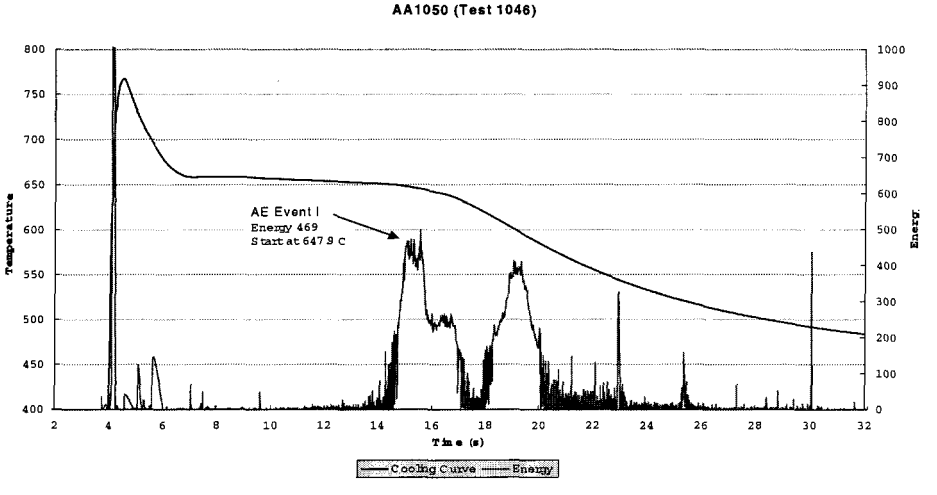

(b) With 6 ppm boron (B)

Fig. 4.20 The superposition graphs of AE energy and cooling curve obtained from AA1050 grain-refined tests.

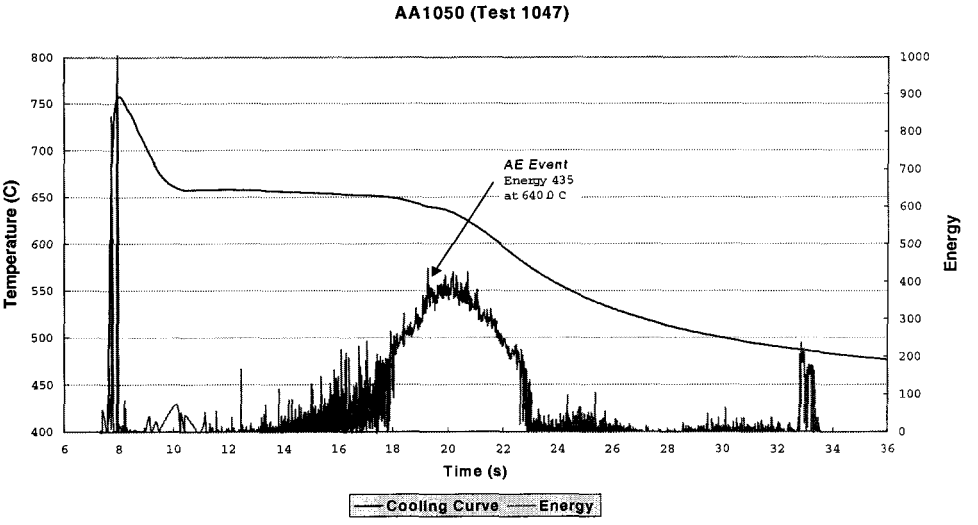

c) With 18 ppm boron (B)

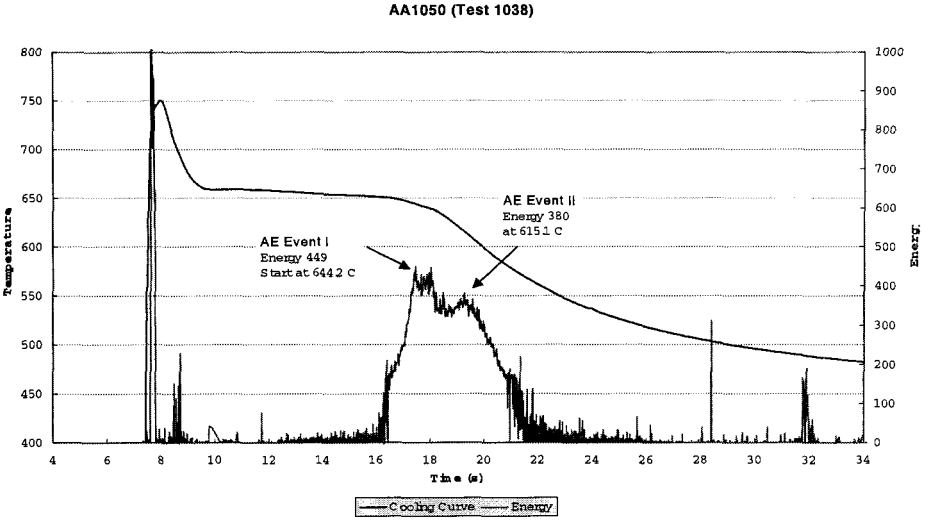

d) With 35ppm boron (B)

Fig. 4.20 The superposition graphs of AE energy and cooling curve obtained from AA1050 grain-refined tests.

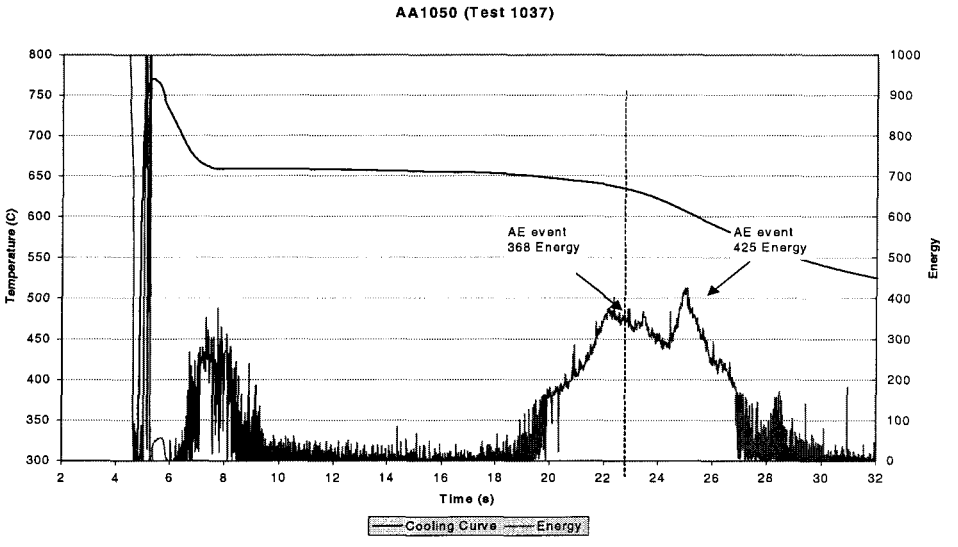

e) With 50ppm grain refiner (B)

Fig. 4.20 The superposition graphs of AE energy and cooling curve obtained from AA1050 grain-refined tests.

Table 4-6 Comparison of a series of test results with different amounts of grain-refiner

	Test	Titanium (ppm)	Boron (ppm)	Energy (Voltage)	Freq. (kHz)	fs
Non grain refined	1041	0	0	643	123	0.941
6ppm Boron	1046	30	6	468	101	0.941
18ppm Boron	1047	90	18	453	87	0.952
35ppm Boron	1038	175	35	449	99	0.955
50ppm Boron	1037	250	50	369	89	0.997

that interdendritic separation initially started at 647.9°C, but the conditions were not sufficient to form hot-tearing or cracking. At this time, the fs (fraction solid) was 0.941.

(c) With 18 ppm B and 90 ppm Ti addition, the AE event started at 640.0C, its energy was 453, and the average frequency was 87 kHz; the fs is 0.952.

(d) With 35 ppm B and 175 ppm Ti addition, the AE event started at 644.2°C, its energy was 449; the average frequency was 99 kHz; the fs was 0.955.

(e) With 50 ppm B and 250 ppm Ti addition, the AE event started at 638.2°C; the energy was 369, the average frequency was 89 kHz, the fs was 0.997.

Fig. 4.21 (a) illustrates the AE signal energy voltage with different amounts of B and Ti. It is clear that the released AE energy is 643 voltage without grain-refinement. A drastic decrease in released AE energy was observed when the content of grain refiner was more than 6 and 30 ppm for B and Ti respectively. More additions showed further decrease in released AE energy though the decrease was slight. When additions were over 35 and 175 ppm for B and Ti, a drastic decrease in released AE energy was again observed. As a result of this experiment, it is confirmed that Ti and B are beneficial additional elements to reduce the hot-tearing susceptibility of AA1050 alloys. Fig. 4.25 (b) shows the fraction solid of AE events vs grain refined AA1050 alloys, these effective results for grain refinement further demonstrate that grain refinement can reduce the hot-tearing tendency of alloys.

The visual observation analysis was carried out for these grain refined tests (three tests for 6 ppm B and 30 ppm Ti, three tests for 18 ppm B and 90 ppm Ti, one test for 35 ppm B and 175 ppm Ti, and two tests for 50 ppm B and 250 ppm Ti). Only one, test 1045 with 18 ppm B and 90 ppm Ti addition, has a visible fracture, but it is really small. In order to investigate the characteristic of the fracture, we examined the fracture surface of test 1045 sample by scanning electron microscope. The result shows 50% free dendrites and 50% typical crack surface. For other grain refined tests, they were not found any visible fracture.

Fig. 4.22 and Fig. 4.23 show the microstuctures of base alloy without and with 18 ppm B + 90 ppm Ti respectively by SEM. The grain structure in base alloy appears in a large columnar fashion (test 1032). However, by the addition of these grain refiners, they were suddenly changed to be very fine equiaxed grains (Test 1045) as shown in Fig. 4.24 when the added amounts were more than 18 ppm, 90 ppm for B and Ti. Further, more addition showed a decrease in grain size of equiaxed grains.

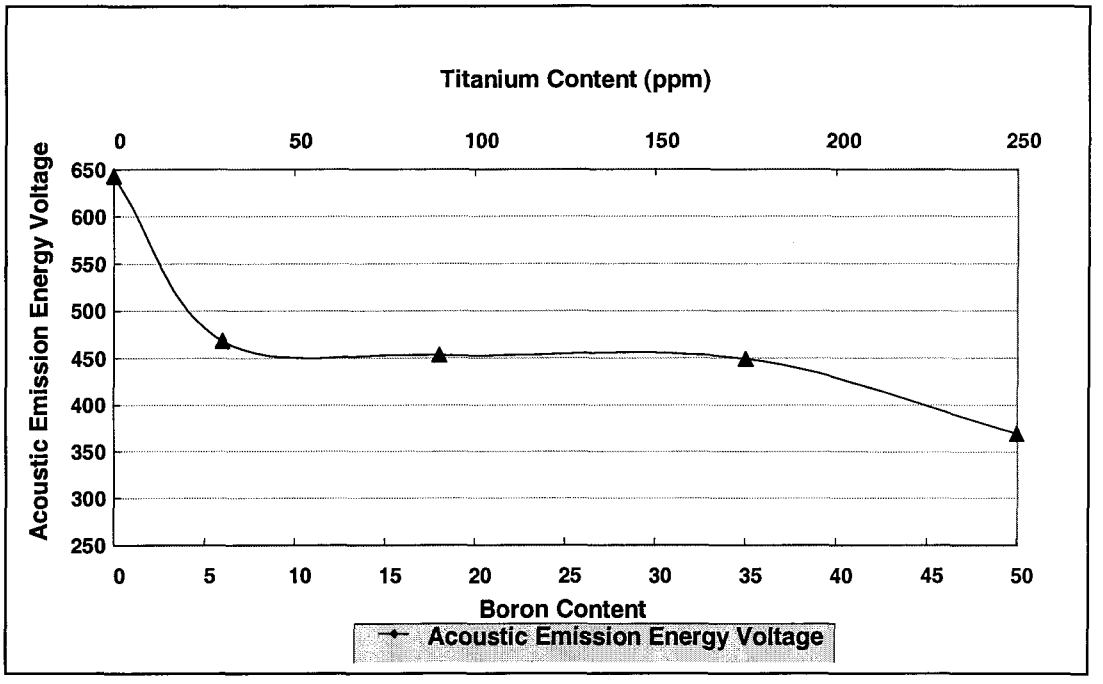

Fig. 4.21 a) Variation of AE energy with grain refiner (B) level;

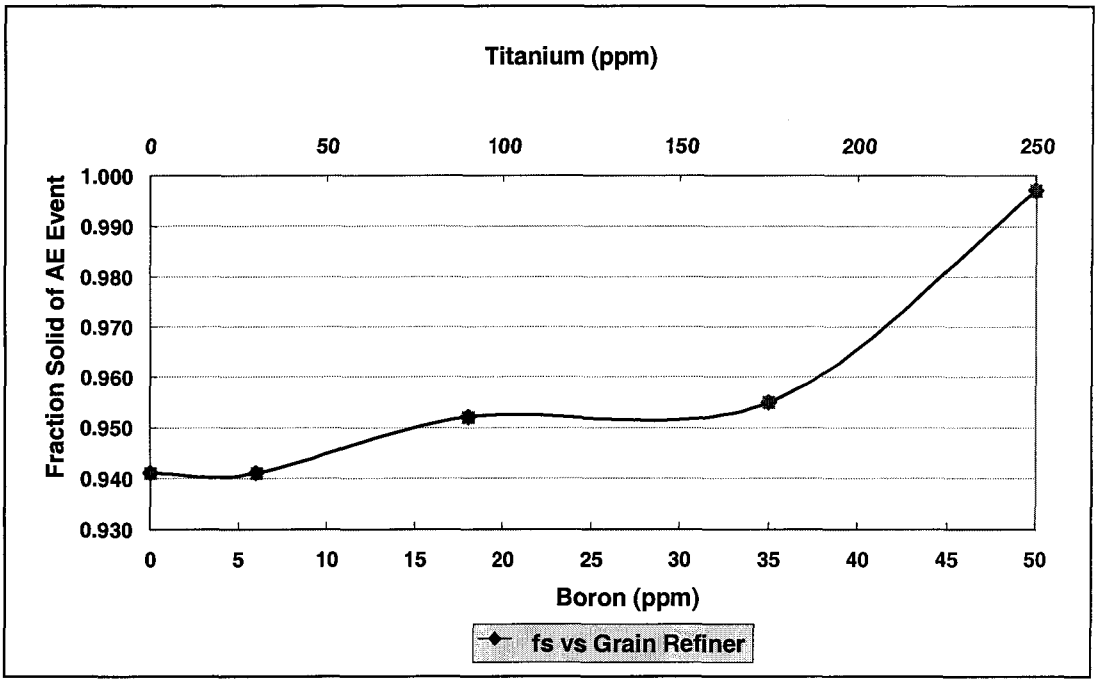

Fig. 4.21 b) Variation of fraction solid-at the start of AE event-with grain refiner (B) level.

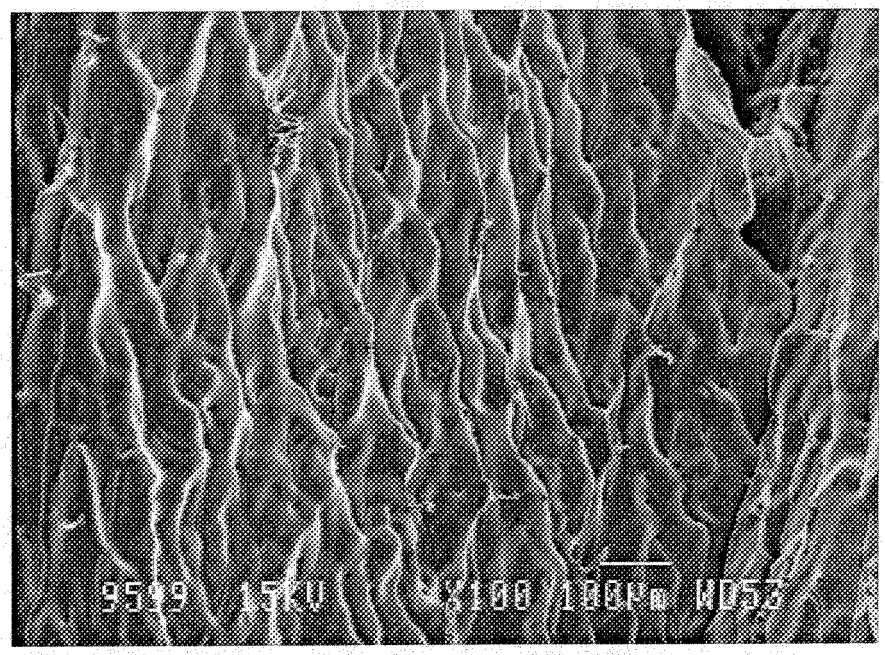

Fig. 4.22 SEM for the typical grain microstructure of base alloy without grain refiners (test 1032), 100X magnification.

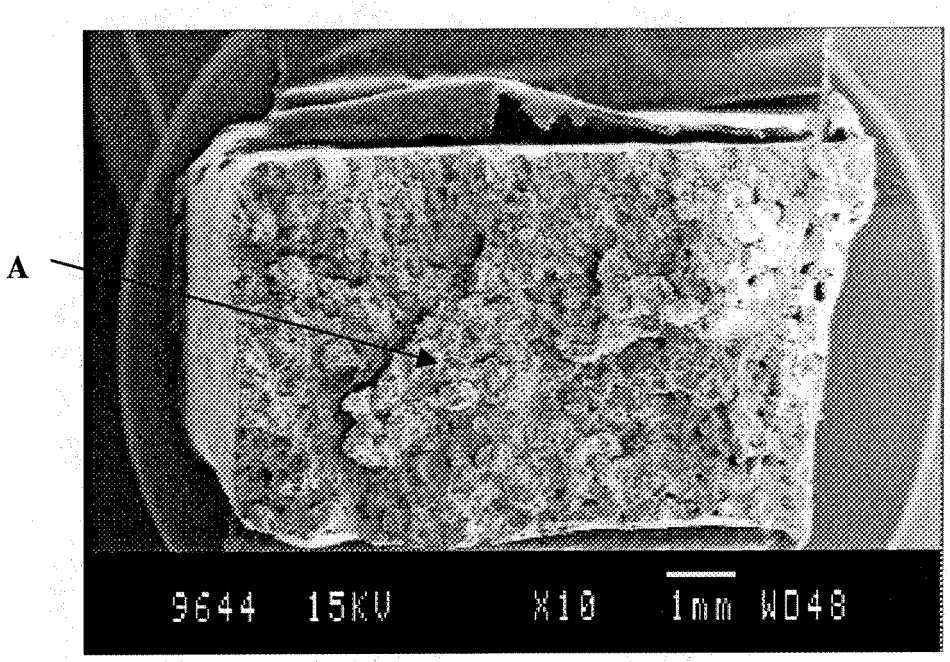

Fig. 4.23 SEM for the typical grain microstucture of base alloy with (18 ppm B and 90 ppm Ti) grain refiners (test 1045), 10X magnigication. The arrow A indicates an area where eutectic constituents have been observed (see figure 4.24 for details and enlarged picture).

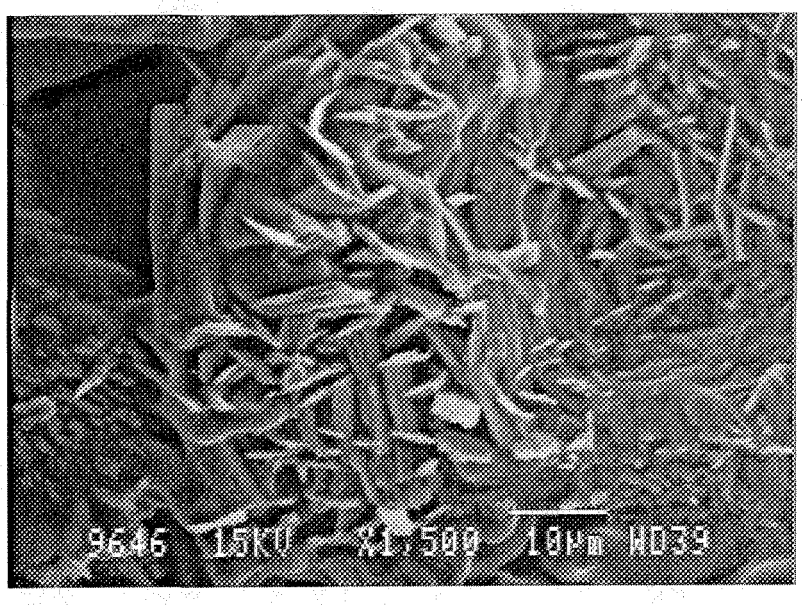

Fig. 4.24 SEM shows the typical eutectic phase at point A in Fig. 4.23, which is base alloy with (18 ppm B and 90 ppm Ti) grain refiners (test 1045).

Chapter V

Conclusions and Recommendations

5.1 Conclusions

1) In-situ and real-time measurement of hot-tearing was attempted by detecting acoustic emission signals.

2) AE signals have been simultaneously sampled with thermal monitoring of solidification. These measurements have provided a defined time frame for solidification and defect formation events and a time definition for AE signal characteristics. AE signals with appreciable peak voltage were produced at a temperature near the completion of solidification in all the castings, and are due to the occurrence of hot-tearing in the later stages of solidification.

3) AE signals accompanying hot-tearing can be summarized by various measurement parameters: the energy is over 600, the average frequency is 125 ± 15 kHz, the duration is between 2 ~ 4 seconds.

4) The results of the thermal analysis for these test conditions can be summarized as follows: the liquidus temperature is about 659 °C, the solidus temperature is under 630 °C, and the temperature when hot-tearing begins is between 650°C ~ 640°C. The corresponding fraction solid when hot-tear begins is between 0.795 ~ 0.998.

5) The hot-tearing tendency in AA1050 alloys with grain refined and without grain refined were investigated by the AE method. There was a reduction of AE energy released from interdendritic separation when the amount of grain refiner was increased. Hot-tearing can be inhibited when a minimum of 18 ppm boron and 90 ppm titanium grain refiner are added based on AE signals as well as visual observation of the castings. Therefore a conclusion that grain refinement can reduce the hot-tearing tendency in AA1050 alloy can be drawn.

6) Corresponding to a decrease of AE energy was a change in the mode of solidification from columnar to fine equiaxed solidification.

7) The fracture surfaces of all samples were investigated under a scanning electron microscope. The typical torn surfaces were observed. Clearly discernible dendrite and dendrite arms with smooth surfaces showed that liquid metal was present at the time of the occurrence of the breakage, proving that the fracture was due to hot-tearing and not to hot-cracking.

5.2 Recommendations for Future Work

Recommendations for future work could include:

1) Further investigation of hot-tearing in different alloys such as AA3105, AA5182, AA6111.

2) Analysis of test results to compare the differences in hot-tearing of the various alloys and the effects of grain refining.

3) To establish relationships between the AE Energy values and the energy values

released during solidification by the formation of hot-tearing.

4) To modify the ring mold with tighter control on the pouring and casting process, data acquisition and stresses generated, and to avoid effect of directional solidification, so that the reproduction of the experiment and the repeatability of test data can be improved.
5) Investigation of trace element effects on hot-tearing.
6) Adaptation of AE monitoring technique as a quality and process control technique in plant environment.

References

[1] Dodd, R. A. "Hot-tearing of Castings: A Review of the Literature", *Foundry Trade Journal,* pp 321-331, (Sep. 20, 1956).

[2] Lange, E. A. and Heine, R. W., "A Test for Hot Tearing Tendency" *Trans., AFS.* vol 60, pp (182-196), (1952).

[3] Bishop, H. F., Ackerlind, C. G. and Pellini, W. S. , "Metallurgy and Mechanics of Hot tearing", *Trans. AFS.,* 60, pp 818-833, (1952).

[4] Singer, A. R. E. and Cottrell, S. A. "Properties of Aluminum-Silicon Alloys at Temperatures in the Region of the Solidus", *J. Inst. of Metals*, 73, p 33, p 73, (1947).

[5] Pellini W.S. "Strain Theory of Hot Tearing", *Foundry*, 80, 124-133, 194,196,199, (1952).

[6] Durrans I. Thesis, *University of Oxford*, (1981).

[7] Warrington D., McCartney D. G., *Cast Metals*, 2, pp 134-143, (1989).

[8] Spittle J.A., Cushway A. A. , *Metals Technol., 10,* pp 6-13, (1983).

[9] Sellars, C. M., *Int. Met. Reviews, 17* (1972), 1.

[10] Feurer, U., "Quality Control of Engineering Alloys, and the Role of Metals Science", *Delft University of Technology,* p.131, (1978).

[11] Clyne, T. W. and Davies, G. J., "Solidification and Casting of Metals", *The metals Society Conference, London,* pp 275-278, (1979).

[12] Middieton, J. M., and Protheroe, H. T., "Hot Tearing of Steel" *J.Iron and Steel Institute* 168, p 384 (1951).

[13] Lange, E. A., and Heine R. W., "A Test for Hot Tearing Tendency", *Trans. AFS.* vol 60, p 182, (1952).

[14] Van Eegheren and A. De Sy, "A contribution to Understanding the Mechanism of Hot-Tearing", *Trans. AFS.* 73. p 282, (1965).

[15] Singer, A.R.E. and Jennings, P. H., *Journal Inst of Metals*, vol 72, p 197, (1946).

[16] Hall, H. F., "Strength and Ductility of Cast Steel During Cooling from the Liquid State in Sand Molds" *2nd Special Report No.15 of the Steel Castings Research Committee of the Iron and Steel Institure, Part IV,* pp 65-93, (1936).

[17] Rosenberg, R. A. ,Flemings, M. C. and Taylor, H. F., "Nonferrous Binary Alloys Hot Tearing", *Trans. AFS,* vol 68, pp 518-528, (1960).

[18] Couture, A. and Edwards, J. O., "The Hot-Tearing of Copper-Base Casting Alloy", *Trans. AFS,* vol.74, pp 709-721, (1966).

[19] Warrington, D. and Mccartney, D. G., "Development of a New Hot-cracking Test for Aluminium Alloys", *Cast Metals, 2*, pp 134-143, (1989).

[20] Gamber, E.J., "Hot Cracking Test for Light Metal Casting Alloys", *Trans. AFS.* vol 67, p 237, (1959).

[21] Kaiser, J., "Untersuchungen uber das auftreten Gerauschen beim Zugversuch (A study of Acoustic Phenomena in Tensile Tests)". *Ph.D. thesis, Technische Hochschule, Munich*, Germany, 1950; also, *Arkiv fur das Eisenhuttenwesen, AREIA*, vol.24, 1-2, pp 43-45, Jan./Feb (in Geman) (1953).

[22] Schofield, B0. H., Bareiss, R. A., and Kyrala, A. A., "Acoustic Emission Under Applied Stress" *ASTIA Document AD 155674, WADC Technical Report.* pp 58-194, (1958).

[23] Tatro, C. A., "Sonic Techniques in the Detection of Crystal Slip in Metals". *Status report, Division of Engineering Research, College of Engineering, Michigan State University, East Lansing, Mich.*, (1959).

[24] Schofield, B. H., "Acoustic Emission Under Applied Stress". *Report ARL-150, Aeronautical Research Laboratory, Office of Technical Services, U.S. Dept. of Commerce, Washington, D. C.*, (1961).

[25] Schofield, B. H., "Acoustic Emission Under Applied Stress" *Final Report, Contract* AF33(616)-5640, Project 7021, Task 70663, Aeronautical Research Laboratory, Wright-Patterson Air Force Base, Ohio, (1964).

[26] Tatro, C. A. and Liptai, R. G., *in Proceedings, Symposium on Physics and Nondestructive Testing, Southwest Research Institute, San Antonio*, Tx., pp 145-158, (1962).

[27] Liptai, R. G. and Tatro, C. A., *in Proceedings, Fourth Annual Symposium on Nondestructive Testing of Aircraft and Missile components, Southwest Pesearch Institute, San Antonio,* Texas, pp 287-341, (1963).

[28] Miller, R.K. and P. McIntire, Ed., *American Society for Nondestructive Testing*, pp 67-186, 187-193, (1987).

[29] Parry, D.L., "Industrial Application of AE Analysis Technology, in Monitoring Structural Integrity by AE", *STP* 571, *American Society for Testing and Materials*, pp 150-183, (1975).

[30] Dunegan, H. L., Harris, D. O., and Tatro, C. A., "Engineering Fracture Mechanics", *EFMEA*, vol. 1, No.1, pp 105-122, (June 1968).

[31] Fisher, R. M. and Lally, J. S., *Canadian Journal of Physics*, CJPHA, vol. 45, No. 2, Part 3, pp 1147-1159, (Feb. 1967).

[32] Dunegan, H. L. and Tatro, C. A. *in Techniques of Metals Research*, vol. 5, Part 2, R.Bunshah, Ed., Wiley, New York, pp 273-312, (1971).

[33] Dunegan, H. L., Harris, D. O., *Ultrasonics*, ULTRA, vol. 7, No.3, pp 160-166, (July 1969).

[34] Liptai, R. G., Dunegan, H. L., and Tatro, C. A., *International Journal of Nondestructive Testing*, IJNTA, vol. 1, No. 3, pp 213-221, (Aug. 1969).

[35] Srawley, J. E. and Brown, W. F., Jr., "Fracture Toughness Testing and Its Applications", *ASTM STP* 381, American Society for Testing and Materials, pp 133-198, (1965).

[36] Brown, W. F., Jr., and Srawley, J. E. : "Plane Strain Crack Toughness Testing of High Strength Metallic Materials". *ASTM STP* 410, *American society for Testing and Matierials*, (1967).

[37] Dunegan, H. L. and Tetelman, A. S., "Nondestructive Characterization of Hydrogen Embrittlement Cracking by Acoustic kEmission Techniques". *submitted for publication to Engineering Fracture Mechanics.*

[38] Gerverich, W. W. and Hartbower, C. E., "Monitoring Crack Growth of Hydrogen Embrittlement and Stress corrosion Cracking by Acoustic Emission". *Proceedings conference on Fundamental Aspects of Stress Corrosion Cracking, Ohio State University*, Columbus, Ohio, (1967).

[39] Dunegan, H. L. and Harris, D. O., "Acoustic emission Techniques". *to be published in Experimental Techniques in Fracture Mechanics, A. S. Kobayashi, Ed., Society for Experimental Stress Analysis.*

[40] Hartbower, C. E., Gerberich, W. W., and crimmins, P. P., *The Welding Journal*, WEJUA, vol. 47, No. 1, pp. 1s-18s,(Jan. 1968).

[41] Green, A. T., Lockman, C. S., and Steele, R. KK., *Modern Plastics*, MOPLA, vol..41, No.11, p 137, (July 1964).

[42] Hutton, P. H. "Detection of Incipient Failure in Nuclear Reactor Pressure System Using Acoustic Emission". *Report BNWL-997, Battelle-Northwest, Richland, Wash.*, (1969).

[43] Hutton, P. H., "Integrity Surveillance of Pressure Systems by Means of Acoustic Emission". *Report BNWL-SA-2194, Battelle-Northwest, Richland, Wash.*, (1969).

[44] Parry, S. and Robinson, D., "Incipient Failure Detection by Acoustic Emission Development and Status Report", *Report IN-1398, Idaho Nuclear Corp., Idaho Falls, Idaho*, (1970).

[45] Muenow, R. A., "Uses of Acoustic Emission in Construction" *presented at Symposium on Acoustic Emission, Bal Harbour, Fla.*, 7-8 (Dec.1971).

[46] Wadley, H. N. G., Scruby, C. B., and Speake, J. H. "Acoustic emission for physical examination of metals". *International Metals Reviews*, No.2, (1980).

[47] Birchon, D.: Br. J. *Non-Destr. Test.*, 18, (3), 66, (1976).

[48] Pollock, A. A.: *Non-Destr. Test.*, 6, 264, (Oct. 1973).

[49] Kiesewetter, N., and Schiller, P.,: *Phys. Status solidi (a)*, 38, 569, (1976).

[50] Mirabile, M.: *ibid.*, 8, 77, (April 1975).

[51] Eshelby, J. D.: *Proc. T. Soc.*, A266, 222, (1962).

[52] Pekeris, C. L. and Lifson, H.: *J. Acoust. Soc. Am.*, 29, (11), 1233, (1957)

[53] Pollock, A. A.: "Acoustic emission Inspection", *METALS HANDBOOK*, Ninth Edition, vol 17, ASM International (1989): pp 278-294

[54] Kumar, T. S. P., Prabhakan, O.; "Acoustic Emission During Solidification of Aluminum Alloys", *AFS Transaction*, vol 93, pp 13-22, (1985).

[55] Ohtaki, M., Naguchi, T., Uto, H., Honma, U., Oya, S.: "In-Situ Detection of Casting Defects in Solidifying Al 7% Si Alloy Castings by the Acoustic Emission Method", *Journal of the Japan Institute of Light Metals*, vol 34, pp 36-41 (1983).

[56] Ohtaki, M., Naguchi, T., Uto, H., Honma, U., Oya, S.: "In-Situ Detection of Hot Tearing in Solidifying Al-Cu and Al-Cu and Al-Si Alloy Castings by the Acoustic Emission Method", *Journal of the Japan Institute of Light Metals*, vol 37, pp 207-213 (1986).

[57] Sharma, D.G.R., Prabhakar, O., Roshan, H.M., Ramachandran E. G.: "Detection of Hot Tearing in Aluminum Alloys by Acoustic Emission Techniques", *Aluminum*, vol 59, pp 519-522 (1983).

[58] Tensi, H.M.: "Acoustic Emission Measurements During Crystallization and Melting of Metals and Binary Alloys", *Proceedings, The Second Acoustic Emission Symposium*, Japan Industrial Planning Association, Tokyo, pp 46-57 (Sep 1974).

[59] Purvis, A.L., Kannatey-Asibu,E., Pehlke, R.D.: "Evaluation of Acoustic Emission from lSsand Cast Alloy 319 During Solidification and Formation of Casting Defects", *AFS Transactions*, vol 98, pp1-7 (1990).

[60] Purvis, A.L., Kannatey-Asibu, E., Pehlke, R. D.: "Acoustic EmissionSignal Characteristics from Casting Defects Formed During Solidification of Al Alloy 319", *AFS Transactions*, vol 102, pp525-530 (1991).

[61] Tremblay, H., Lessard, S., and Pekguleryuz, M. : "Fissuration a chaud a l'aide d'Emissions Acoustiques", *ALCAN-UQAC Chair Research Report*, 1996.

[62] Backerud, L., Krol, E. and Tamminen, J. "Solidification Characteristics of Aluminium Alloys" vol.1: Wrought Alloys. *Department of Structural Chemistry Arrhenius Laboratory, University of Stockholm S-106 91 STOCKHOLM, SWEDEN.*

[63] "Properties of Wrought Aluminum and Aluminum Alloys", *Metals Handbook*, vol.2 10^{th} edition.

[64] Aliravci, C. A., Larouche, M. E. and Mihriban, P. Ö. "A Comparative Study of Fraction-Solid Evolution in Aluminum Alloys: Experimental Determination at Different Cooling Rates vs Calculation via the Scheil Model", *Alcan-UQAC Chair in Solidification and Metallurgy of Aluminium,* Chicoutimi, Québec, Canada

[65] Aliravci, C. A., "Investigation of Quantitative Methods to Measure the Hot Tearing Tendency in Wrought Aluminum Alloys", *Summary Report I, Alcan-UQAC Chair on Solidification and Metallurgy of Aluminum*, Chicoutimi, Quebec, Canada, 1995.

Appendix I

Test results of the superposition graphs of AE signals and the cooling/solidification curves (25 test results):

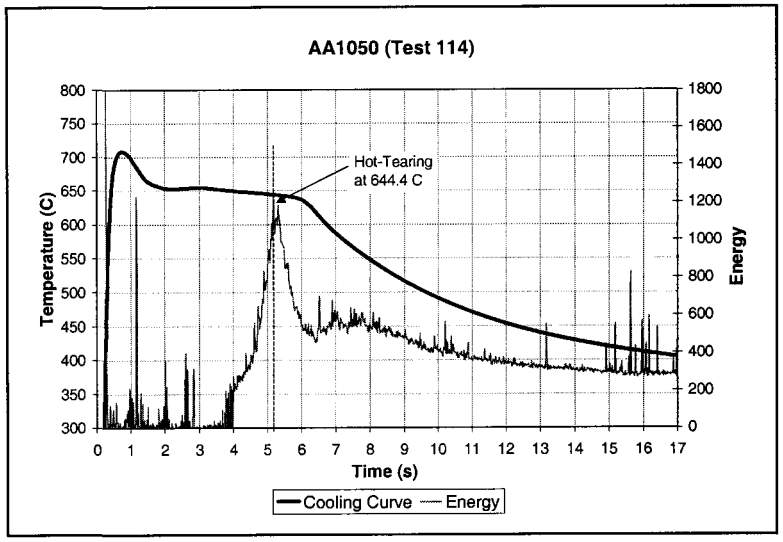
AA1050 (Test 114)
Hot-Tearing
at 644.4 C
Temperature (C)
Energy
Time (s)
Cooling Curve
Energy

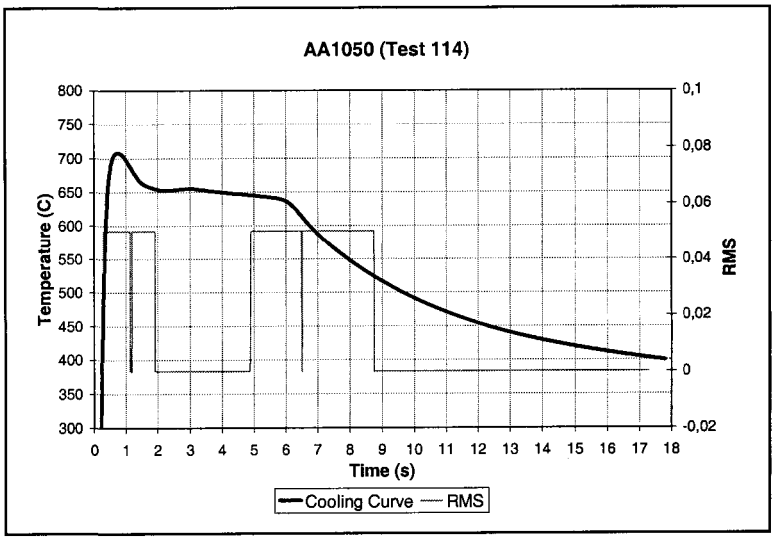
AA1050 (Test 114)
Temperature (C)
RMS
Time (s)
Cooling Curve
RMS

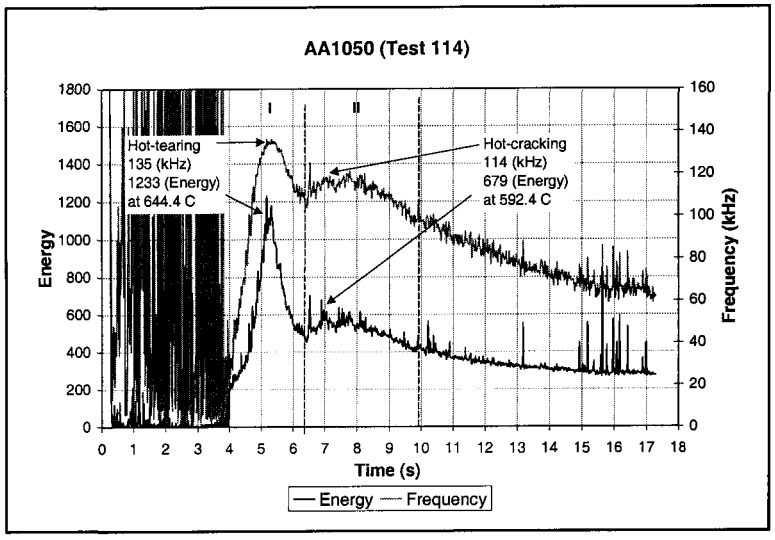
AA1050 (Test 114)
I
II
Hot-tearing
135 (kHz)
1233 (Energy)
at 644.4 C
Hot-cracking
114 (kHz)
679 (Energy)
at 592.4 C
Energy
Frequency (kHz)
Time (s)
Energy
Frequency

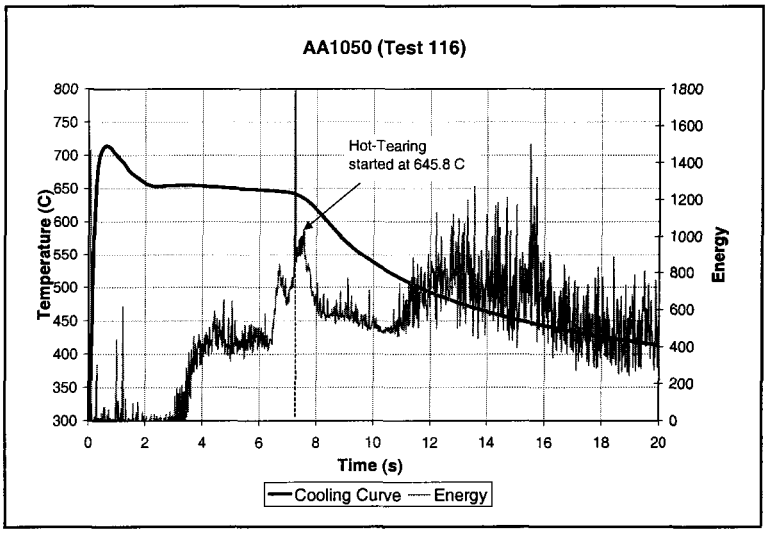
AA1050 (Test 116)
Hot-Tearing
started at 645.8 C
Temperature (C)
Energy
Time (s)
Cooling Curve
Energy

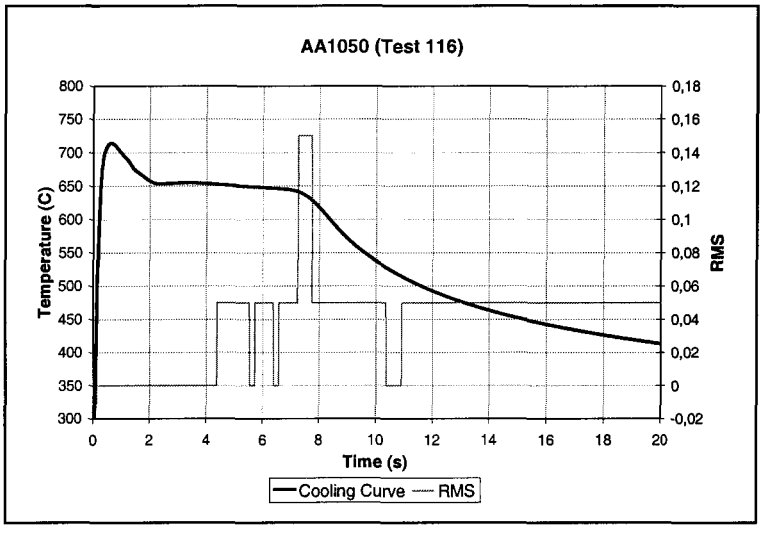
AA1050 (Test 116)
Temperature (C)
RMS
Time (s)
Cooling Curve
RMS

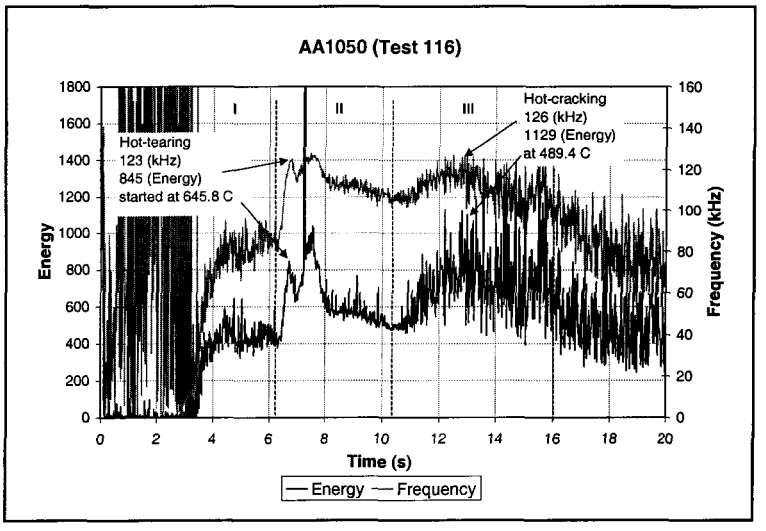
AA1050 (Test 116)
I
II
III
Hot-tearing
123 (kHz)
845 (Energy)
started at 645.8 C
Hot-cracking
126 (kHz)
1129 (Energy)
at 489.4 C
Energy
Frequency (kHz)
Time (s)
Energy
Frequency

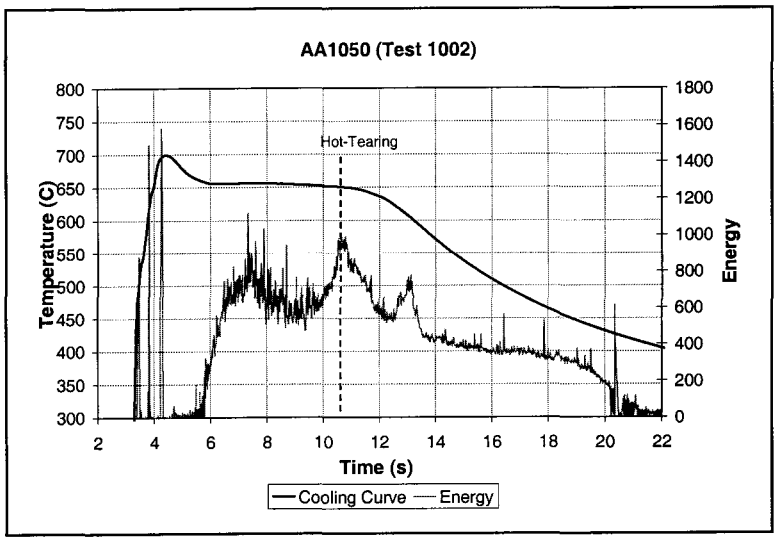
AA1050 (Test 1002)
Hot-Tearing
Temperature (C)
Energy
Time (s)
Cooling Curve
Energy

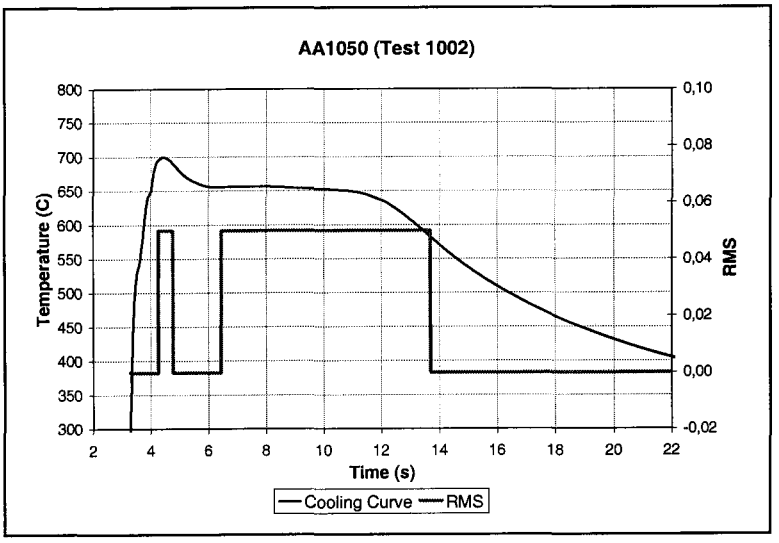
AA1050 (Test 1002)
Temperature (C)
RMS
Time (s)
Cooling Curve
RMS

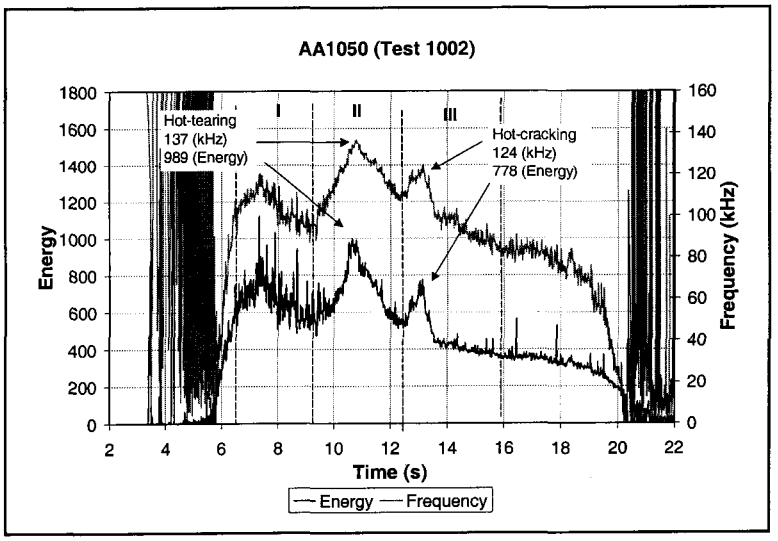
AA1050 (Test 1002)
Hot-tearing
137 (kHz)
989 (Energy)
I
II
III
Hot-cracking
124 (kHz)
778 (Energy)
Energy
Frequency (kHz)
Time (s)
Energy
Frequency

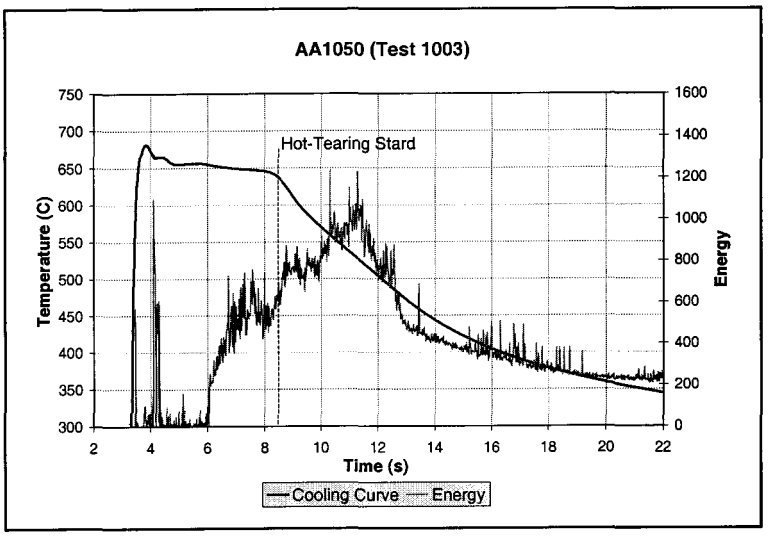
AA1050 (Test 1003)
Hot-Tearing Stard
Temperature (C)
Energy
Time (s)
Cooling Curve
Energy

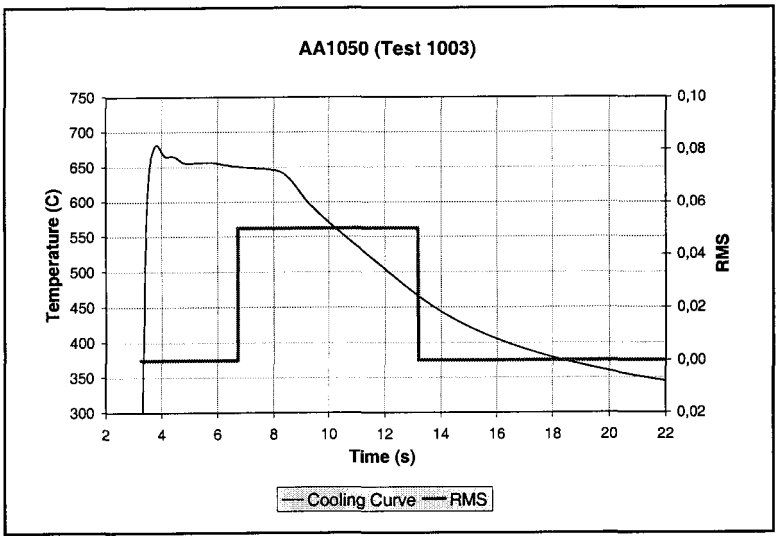
AA1050 (Test 1003)
Temperature (C)
RMS
Time (s)
Cooling Curve
RMS

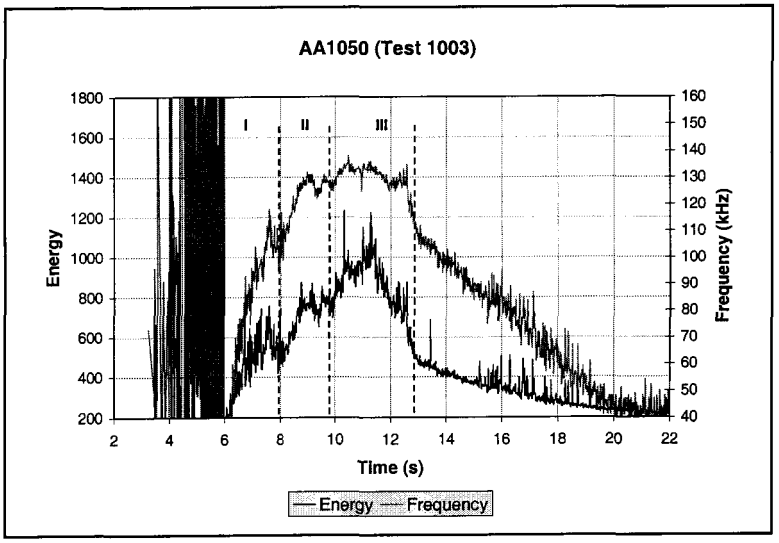
AA1050 (Test 1003)
I
II
III
Energy
Frequency (kHz)
Time (s)
Energy
Frequency

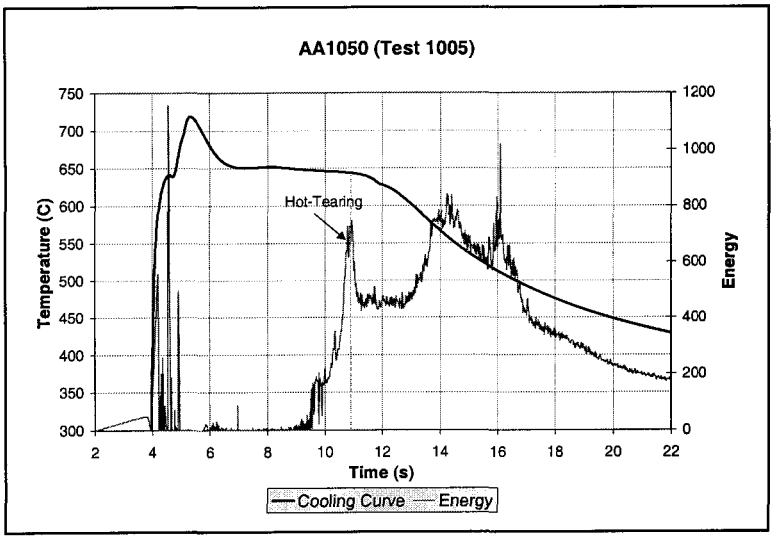
AA1050 (Test 1005)
Temperature (C)
Energy
Time (s)
Hot-Tearing
Cooling Curve
Energy

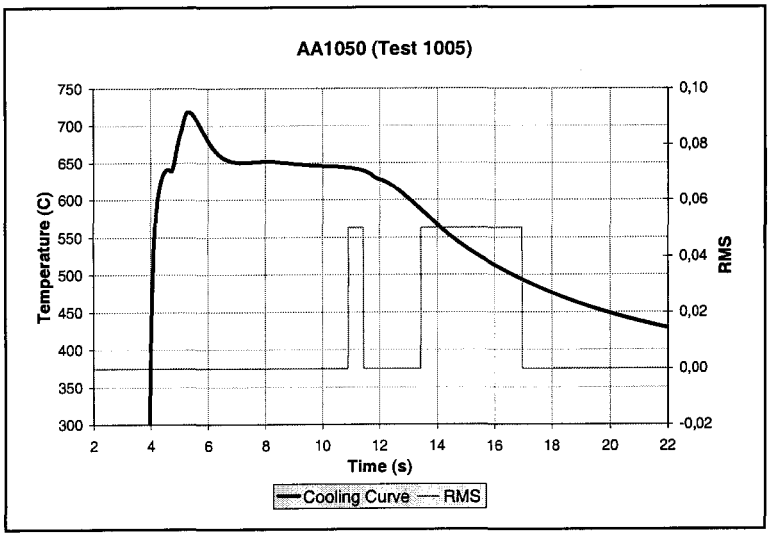
AA1050 (Test 1005)
Temperature (C)
RMS
Time (s)
Cooling Curve
RMS

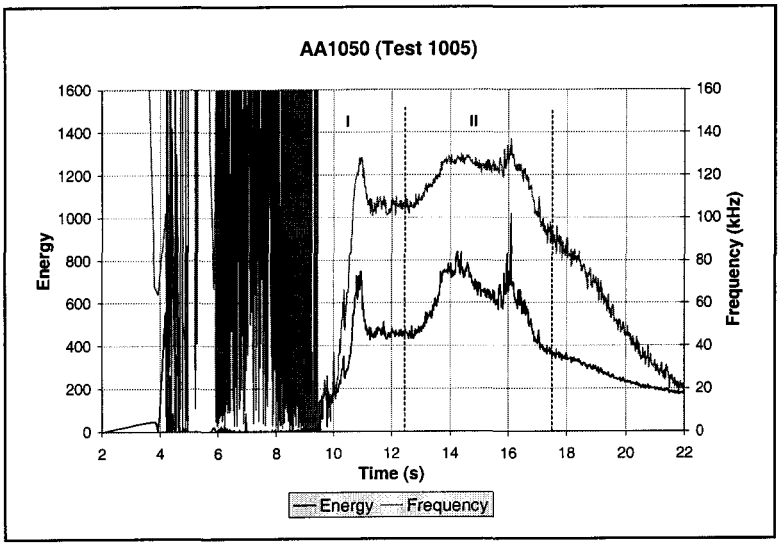
AA1050 (Test 1005)
Energy
Frequency (kHz)
Time (s)
I
II
Energy
Frequency

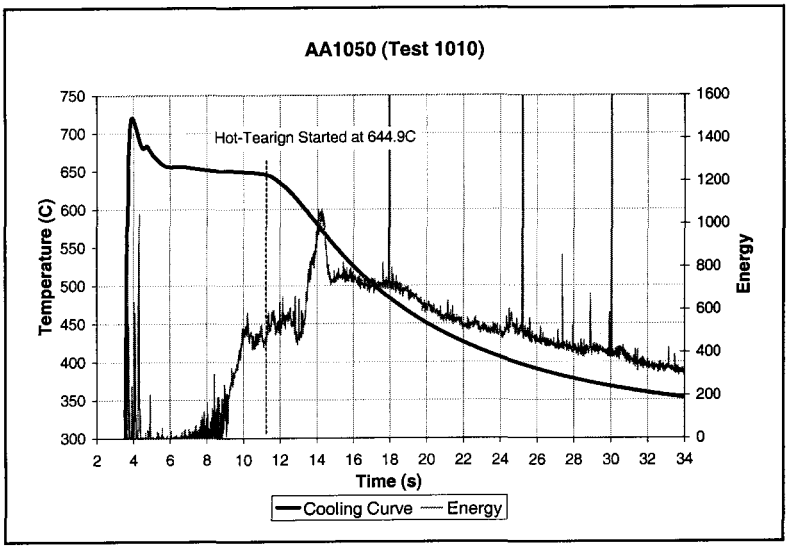
AA1050 (Test 1010)
Hot-Tearign Started at 644.9C
Temperature (C)
Energy
Time (s)
Cooling Curve
Energy

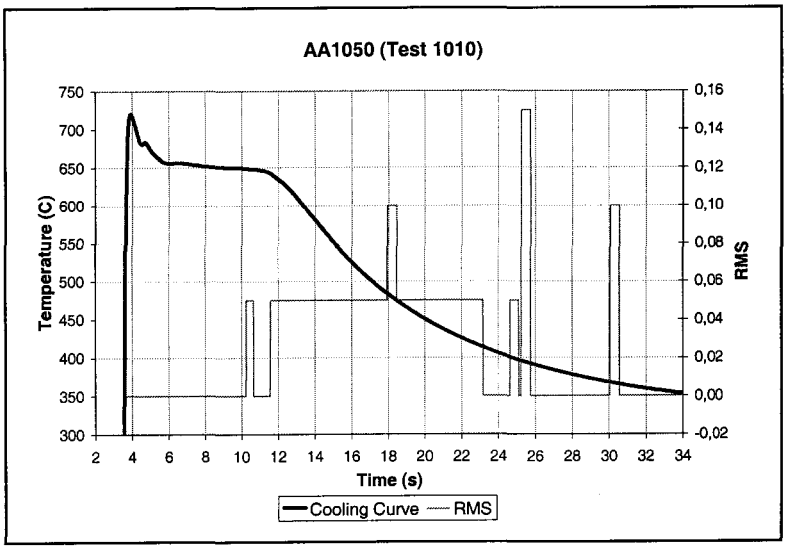
AA1050 (Test 1010)
Temperature (C)
RMS
Time (s)
Cooling Curve
RMS

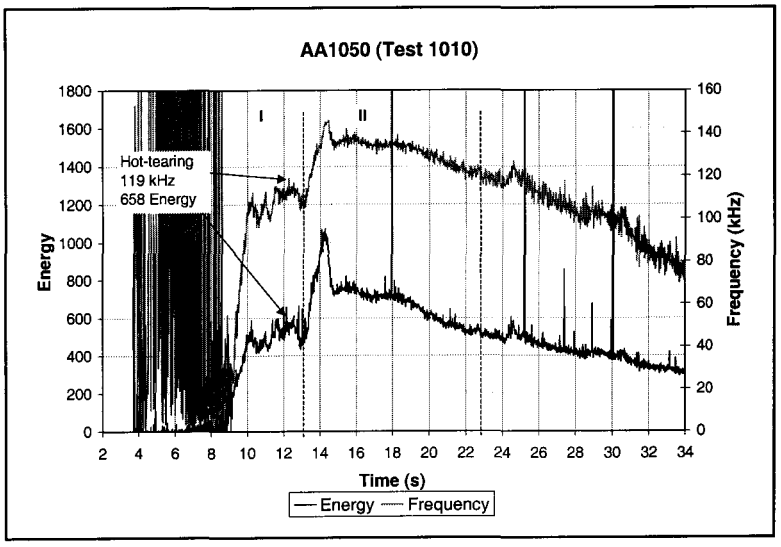
AA1050 (Test 1010)
I
II
Hot-tearing
119 kHz
658 Energy
Energy
Frequency (kHz)
Time (s)
Energy
Frequency

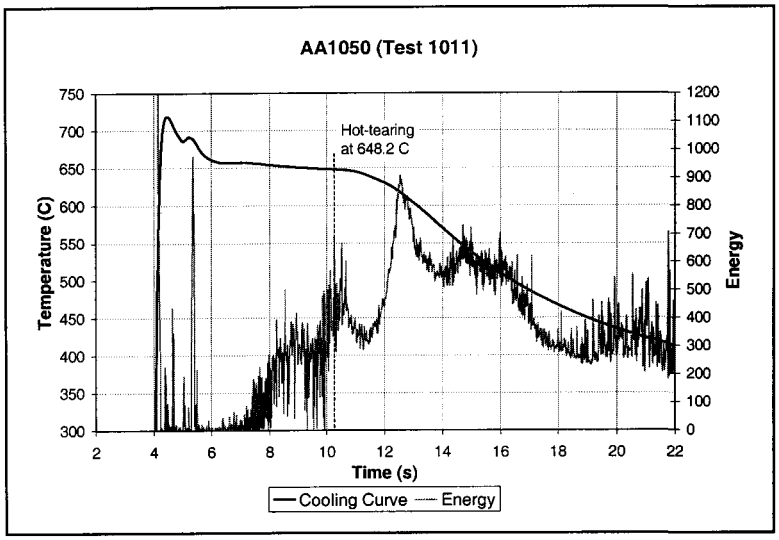
AA1050 (Test 1011)
Hot-tearing
at 648.2 C
Temperature (C)
Energy
Time (s)
Cooling Curve
Energy

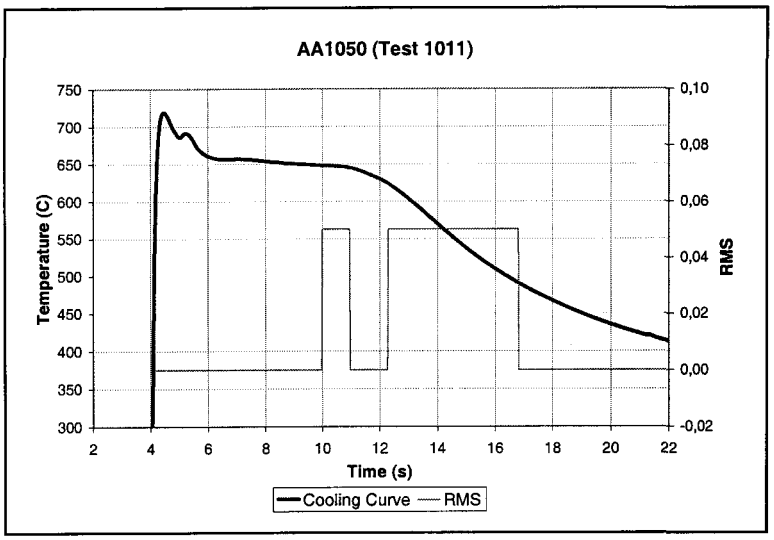
AA1050 (Test 1011)
Temperature (C)
RMS
Time (s)
Cooling Curve
RMS

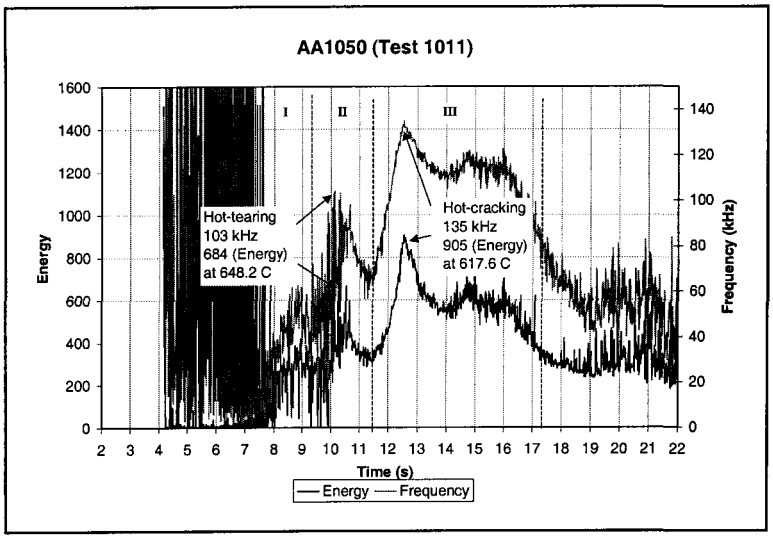
AA1050 (Test 1011)
I
II
III
Hot-tearing
103 kHz
684 (Energy)
at 648.2 C
Hot-cracking
135 kHz
905 (Energy)
at 617.6 C
Energy
Frequency (kHz)
Time (s)
Energy
Frequency

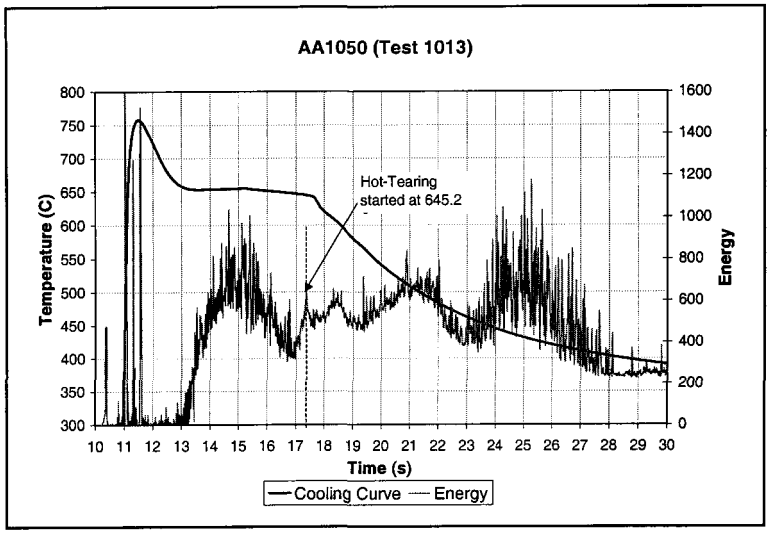
AA1050 (Test 1013)
Temperature (C)
Energy
Hot-Tearing
started at 645.2
Time (s)
Cooling Curve
Energy

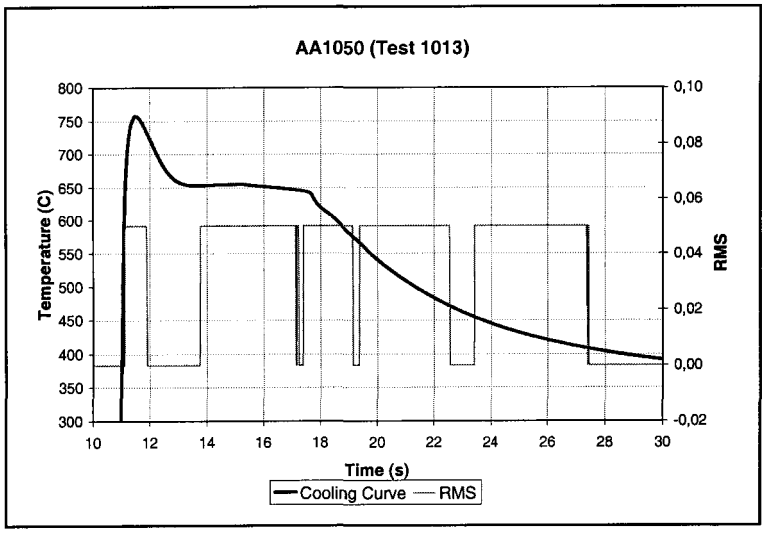
AA1050 (Test 1013)
Temperature (C)
RMS
Time (s)
Cooling Curve
RMS

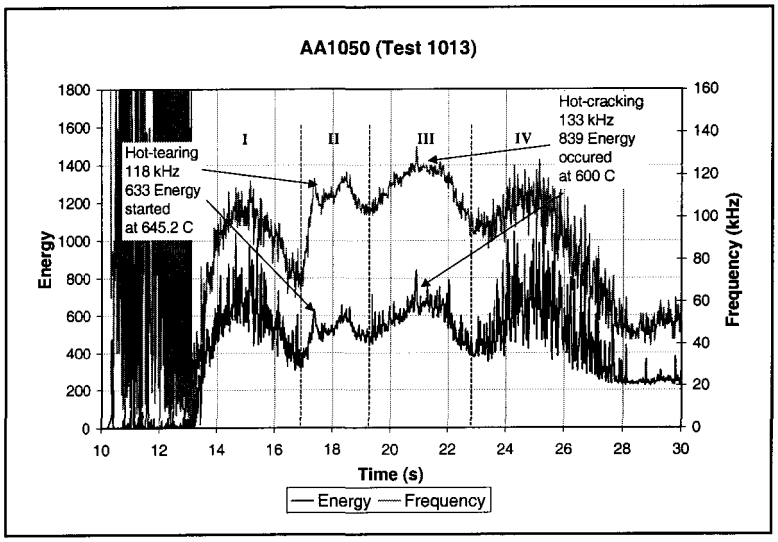
AA1050 (Test 1013)
Energy
Frequency (kHz)
Hot-tearing
118 kHz
633 Energy
started
at 645.2 C
Hot-cracking
133 kHz
839 Energy
occured
at 600 C
I
II
III
IV
Time (s)
Energy
Frequency

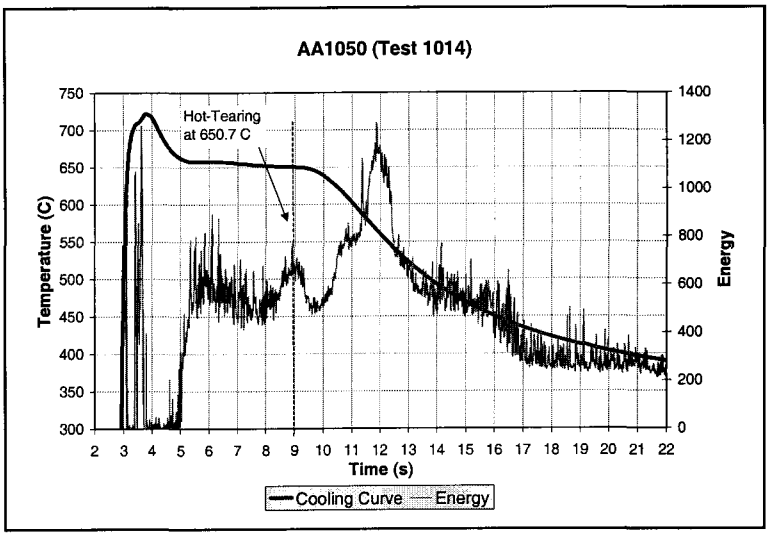
AA1050 (Test 1014)
Hot-Tearing
at 650.7 C
Temperature (C)
Energy
Time (s)
Cooling Curve
Energy

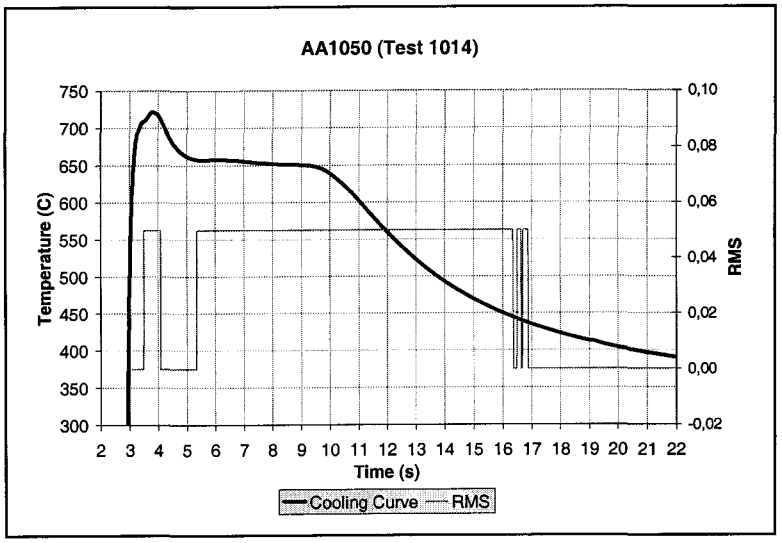
AA1050 (Test 1014)
Temperature (C)
RMS
Time (s)
Cooling Curve
RMS

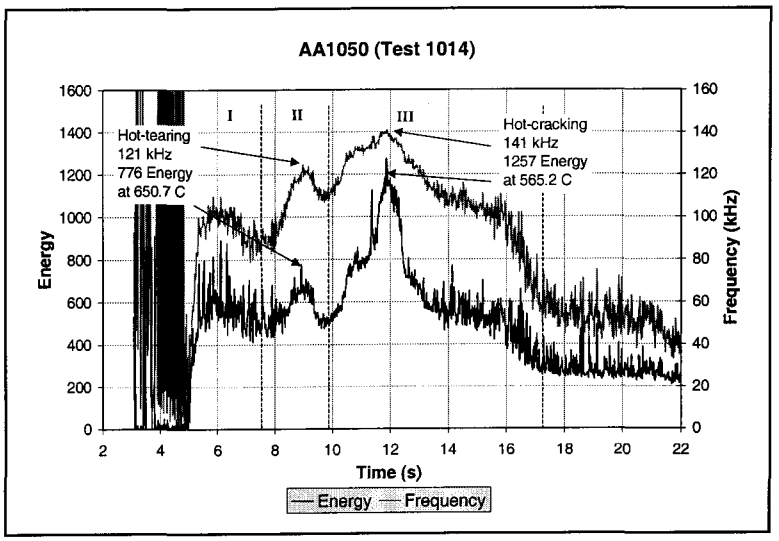
AA1050 (Test 1014)
I
II
III
Hot-tearing
121 kHz
776 Energy
at 650.7 C
Hot-cracking
141 kHz
1257 Energy
at 565.2 C
Energy
Frequency (kHz)
Time (s)
Energy
Frequency

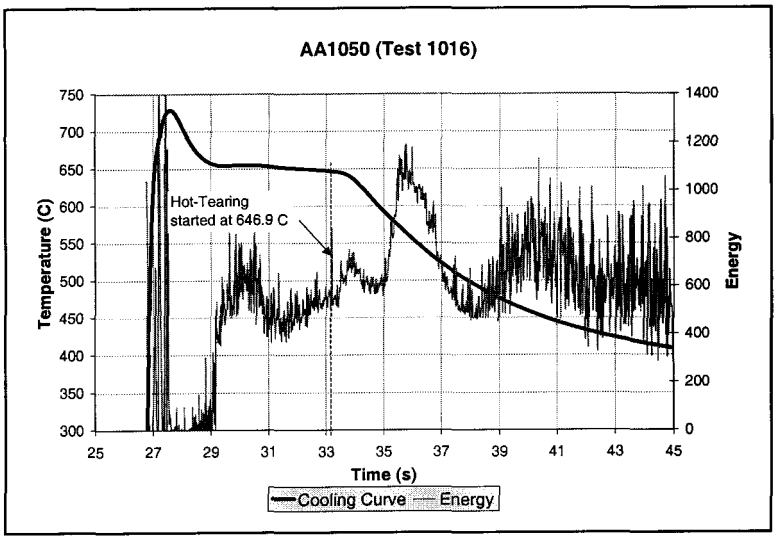
AA1050 (Test 1016)
Temperature (C)
Energy
Time (s)
Hot-Tearing
started at 646.9 C
Cooling Curve
Energy

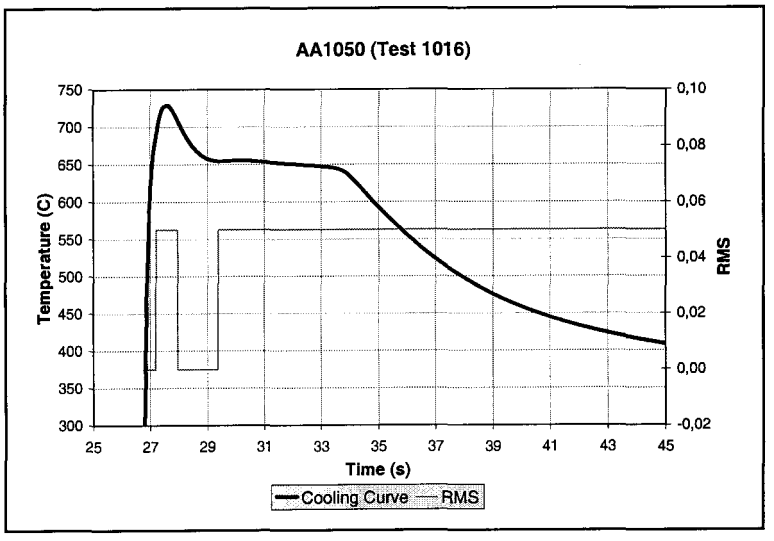
AA1050 (Test 1016)
Temperature (C)
RMS
Time (s)
Cooling Curve
RMS

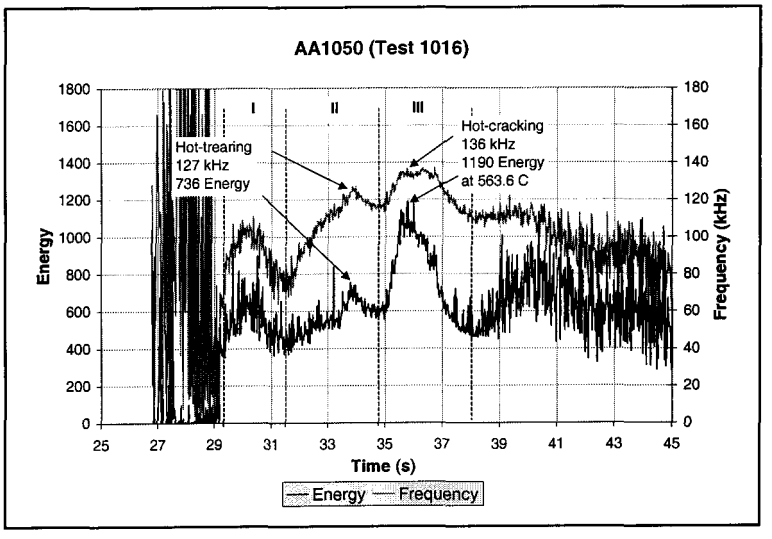
AA1050 (Test 1016)
Energy
Frequency (kHz)
Time (s)
I
II
III
Hot-trearing
127 kHz
736 Energy
Hot-cracking
136 kHz
1190 Energy
at 563.6 C
Energy
Frequency

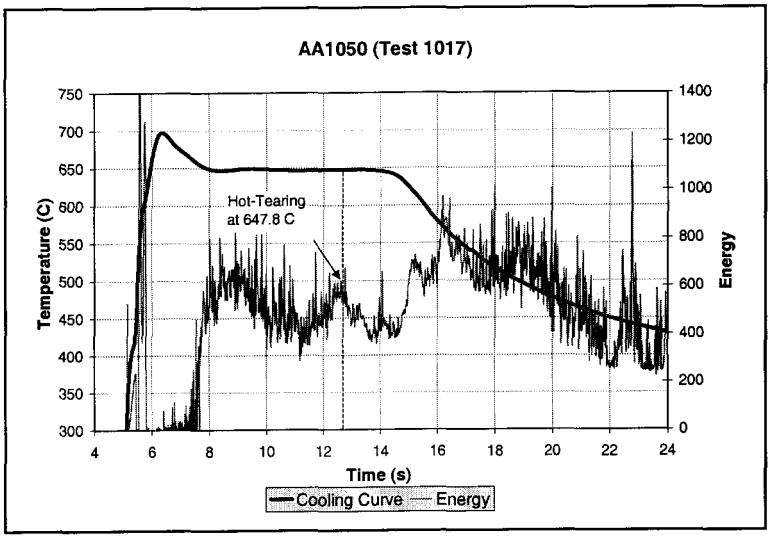
AA1050 (Test 1017)
Temperature (C)
Energy
Time (s)
Hot-Tearing
at 647.8 C
Cooling Curve
Energy

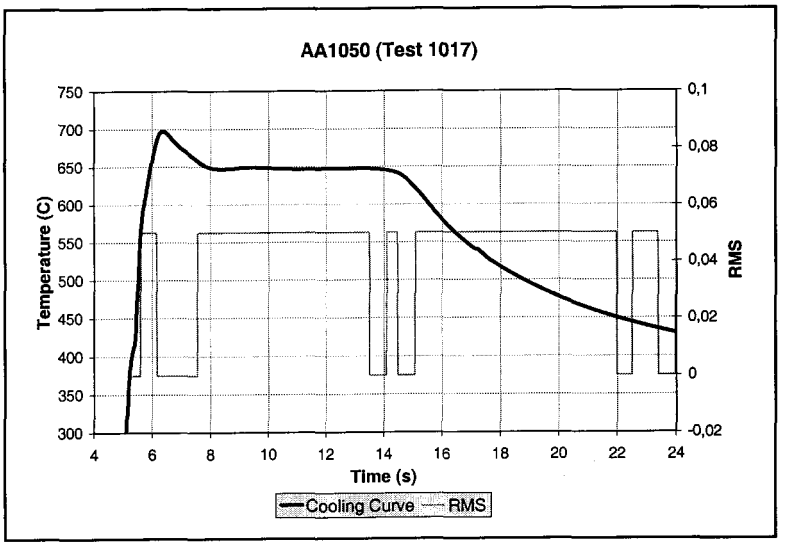
AA1050 (Test 1017)
Temperature (C)
RMS
Time (s)
Cooling Curve
RMS

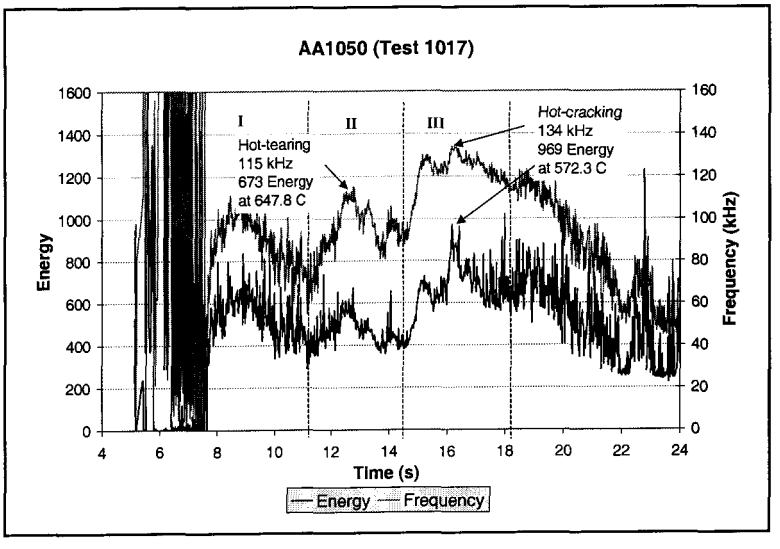
AA1050 (Test 1017)
Energy
Frequency (kHz)
Time (s)
I
II
III
Hot-tearing
115 kHz
673 Energy
at 647.8 C
Hot-cracking
134 kHz
969 Energy
at 572.3 C
Energy
Frequency

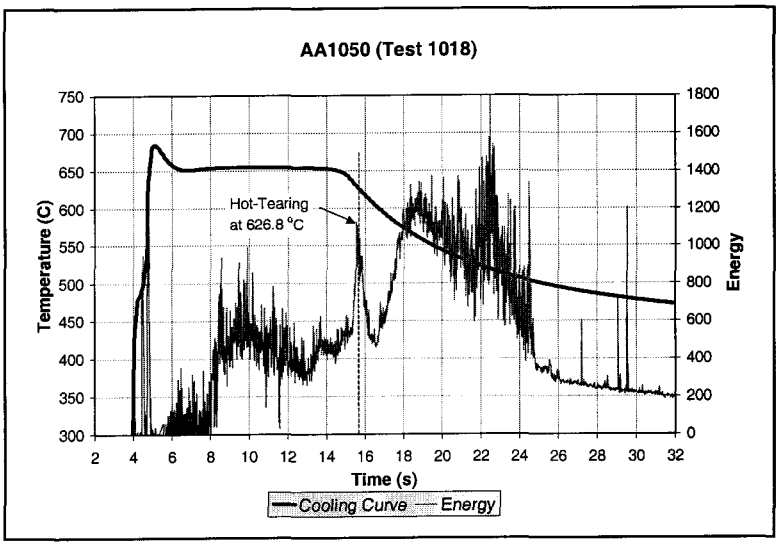
AA1050 (Test 1018)
Temperature (C)
Energy
Time (s)
Hot-Tearing
at 626.8 °C
Cooling Curve
Energy

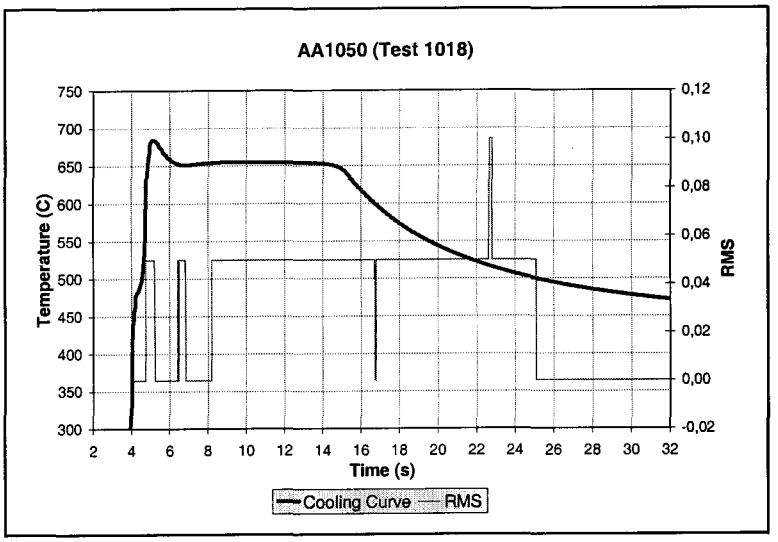
AA1050 (Test 1018)
Temperature (C)
RMS
Time (s)
Cooling Curve
RMS

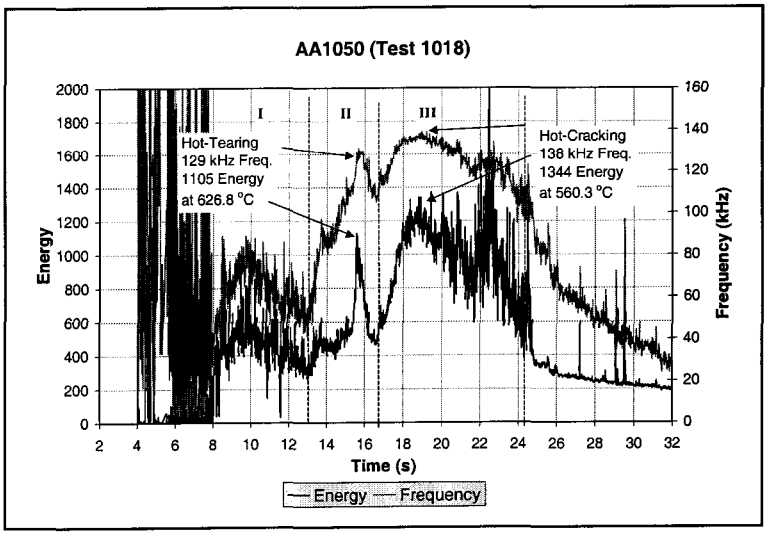
AA1050 (Test 1018)
Energy
Frequency (kHz)
Time (s)
I
II
III
Hot-Tearing
129 kHz Freq.
1105 Energy
at 626.8 °C
Hot-Cracking
138 kHz Freq.
1344 Energy
at 560.3 °C
Energy
Frequency

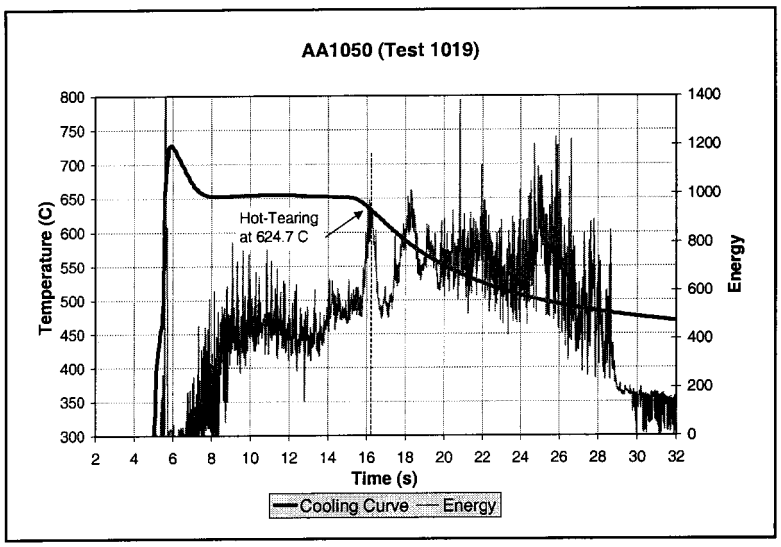
AA1050 (Test 1019)
Temperature (C)
Energy
Time (s)
Hot-Tearing
at 624.7 C
Cooling Curve
Energy

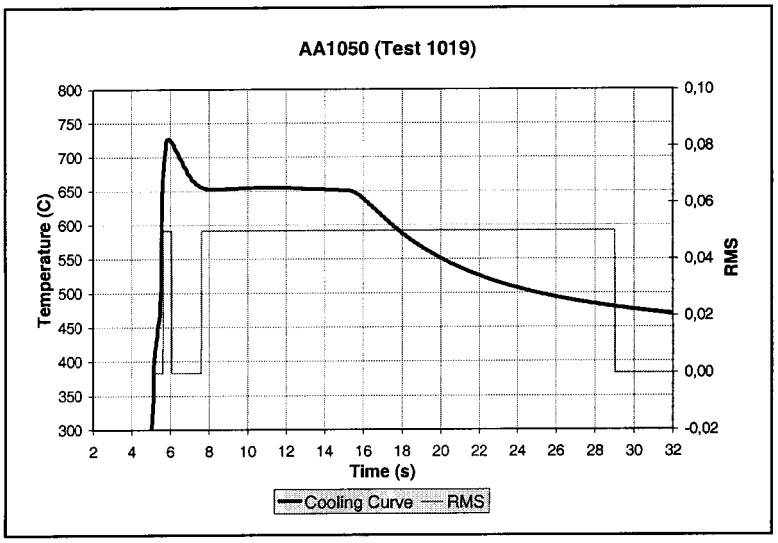
AA1050 (Test 1019)
Temperature (C)
RMS
Time (s)
Cooling Curve
RMS

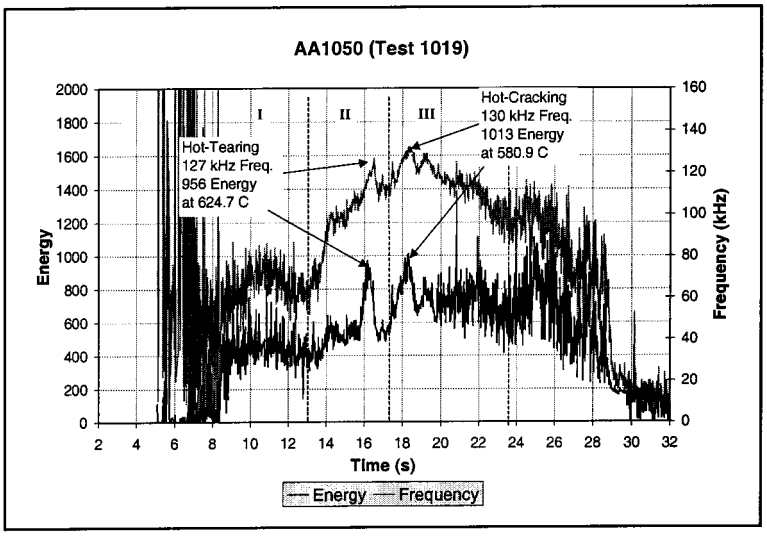
AA1050 (Test 1019)
Energy
Frequency (kHz)
Time (s)
I
II
III
Hot-Tearing
127 kHz Freq.
956 Energy
at 624.7 C
Hot-Cracking
130 kHz Freq.
1013 Energy
at 580.9 C
Energy
Frequency

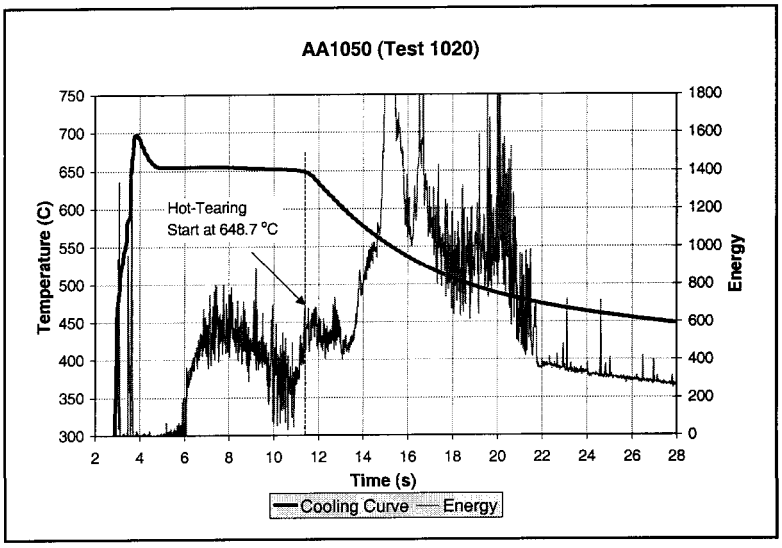
AA1050 (Test 1020)
Temperature (C)
Energy
Time (s)
Hot-Tearing
Start at 648.7 °C
Cooling Curve
Energy

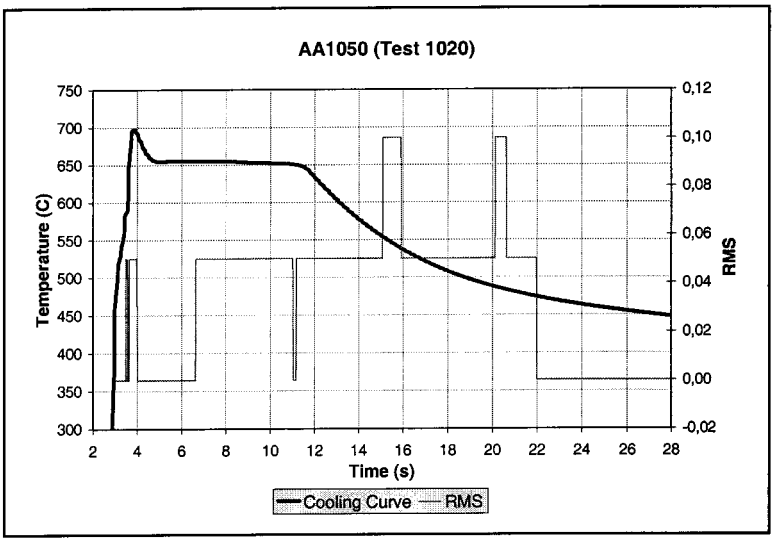
AA1050 (Test 1020)
Temperature (C)
RMS
Time (s)
Cooling Curve
RMS

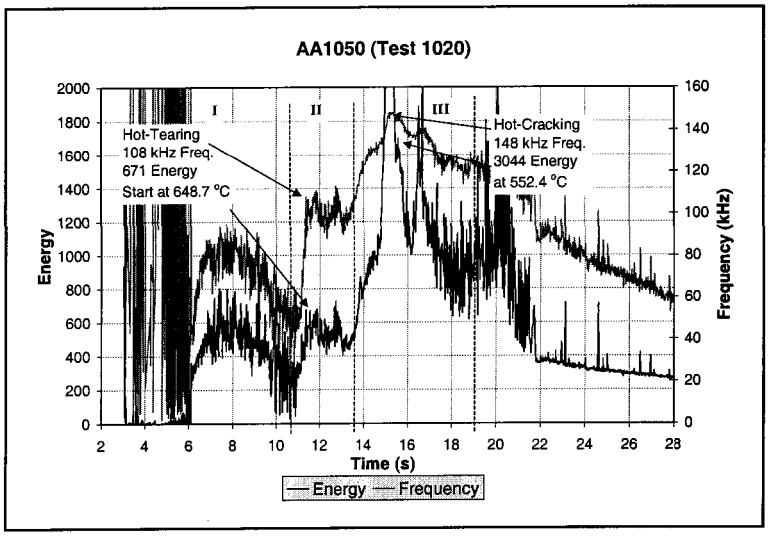
AA1050 (Test 1020)
Energy
Frequency (kHz)
Time (s)
I
II
III
Hot-Tearing
108 kHz Freq.
671 Energy
Start at 648.7 °C
Hot-Cracking
148 kHz Freq.
3044 Energy
at 552.4 °C
Energy
Frequency

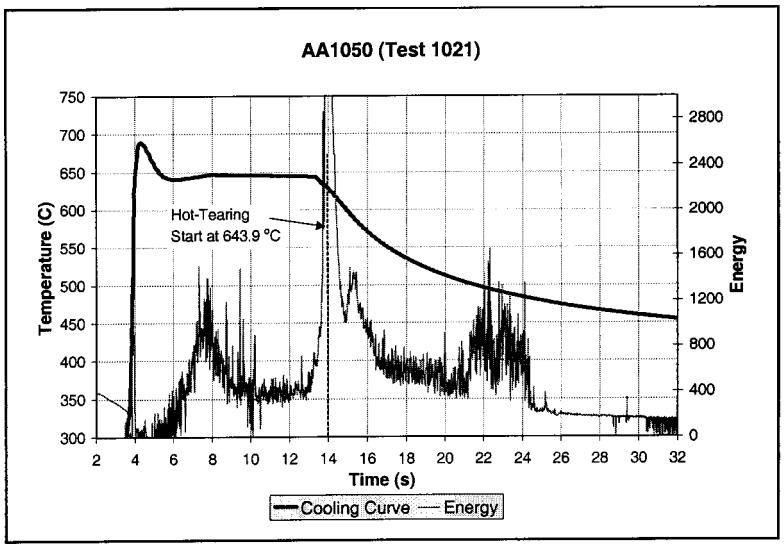
AA1050 (Test 1021)
Temperature (C)
Energy
Time (s)
Hot-Tearing
Start at 643.9 °C
Cooling Curve
Energy

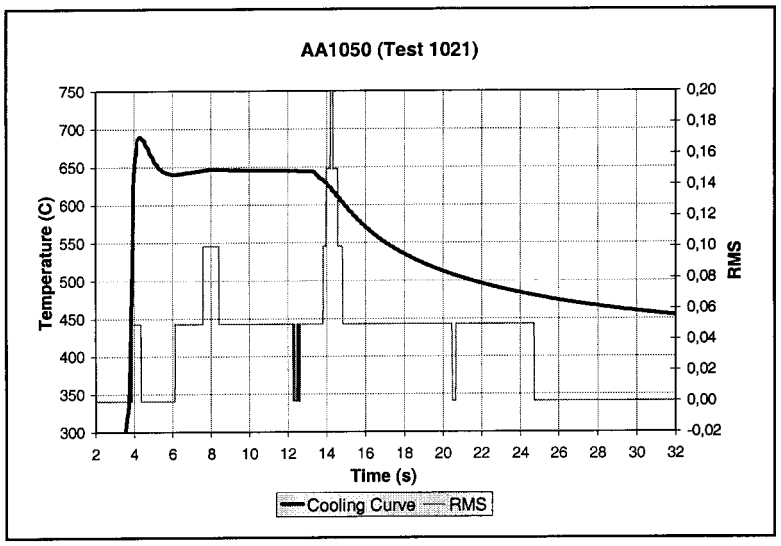
AA1050 (Test 1021)
Temperature (C)
RMS
Time (s)
Cooling Curve
RMS

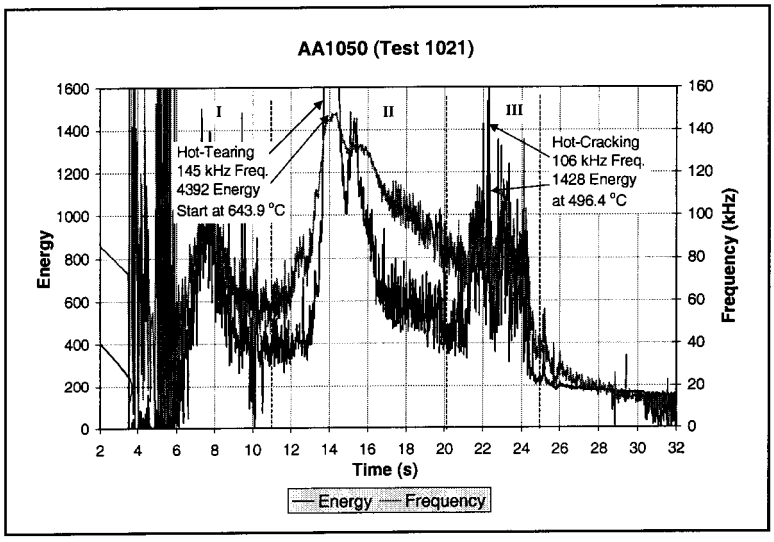
AA1050 (Test 1021)
Energy
Frequency (kHz)
Time (s)
I
II
III
Hot-Tearing
145 kHz Freq.
4392 Energy
Start at 643.9 °C
Hot-Cracking
106 kHz Freq.
1428 Energy
at 496.4 °C
Energy
Frequency

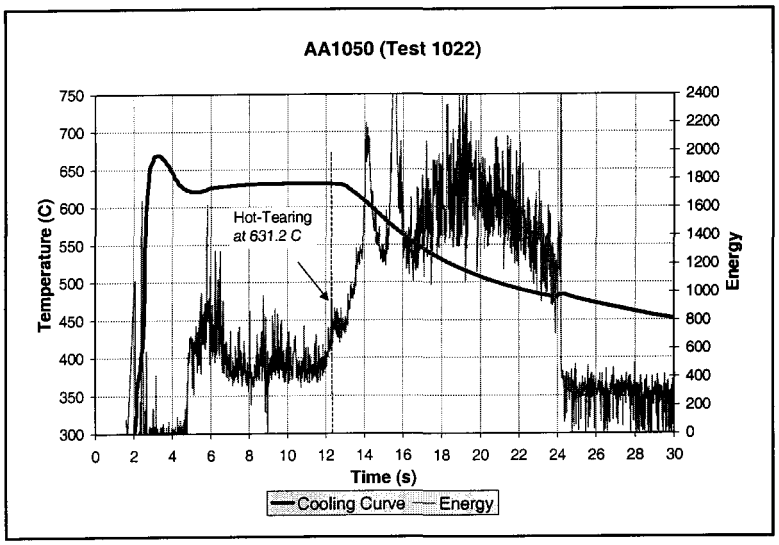
AA1050 (Test 1022)
Temperature (C)
Energy
Hot-Tearing
at 631.2 C
Time (s)
Cooling Curve
Energy

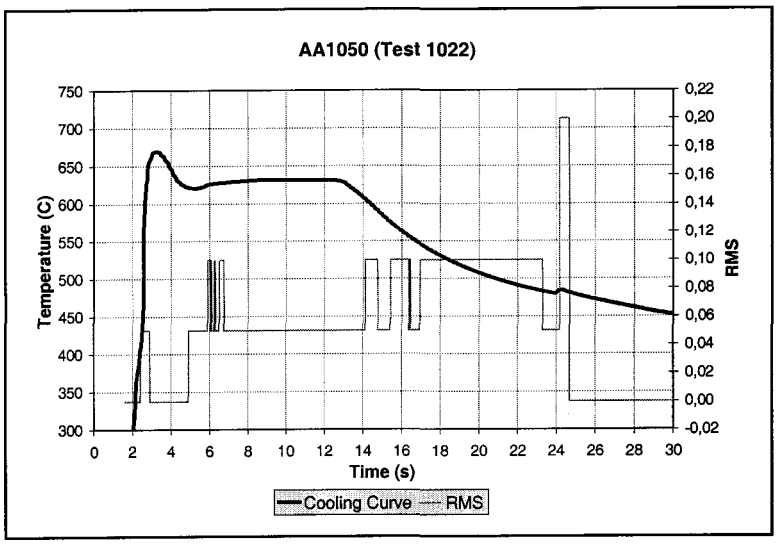
AA1050 (Test 1022)
Temperature (C)
RMS
Time (s)
Cooling Curve
RMS

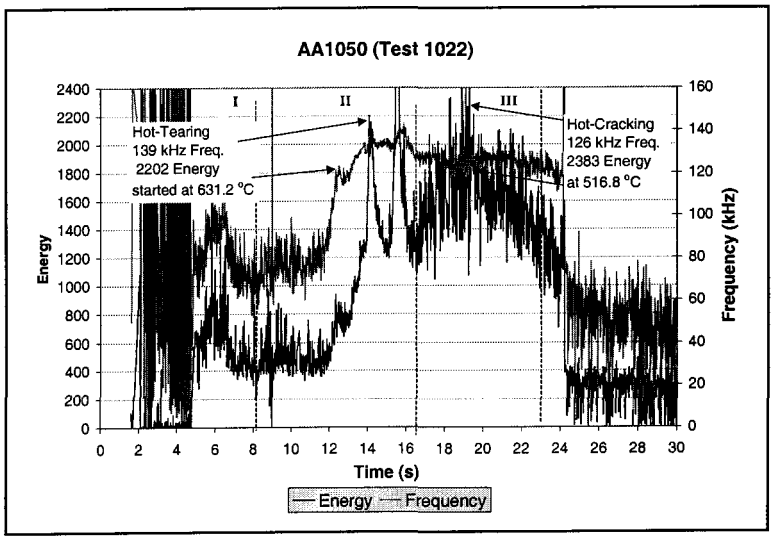
AA1050 (Test 1022)
I
II
III
Hot-Tearing
139 kHz Freq.
2202 Energy
started at 631.2 °C
Hot-Cracking
126 kHz Freq.
2383 Energy
at 516.8 °C
Energy
Frequency (kHz)
Time (s)
Energy
Frequency

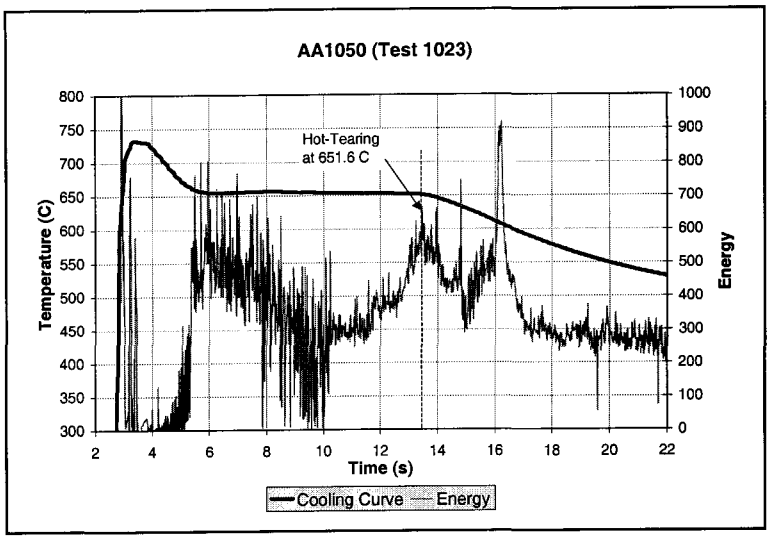
AA1050 (Test 1023)
Hot-Tearing
at 651.6 C
Temperature (C)
Energy
Time (s)
Cooling Curve
Energy

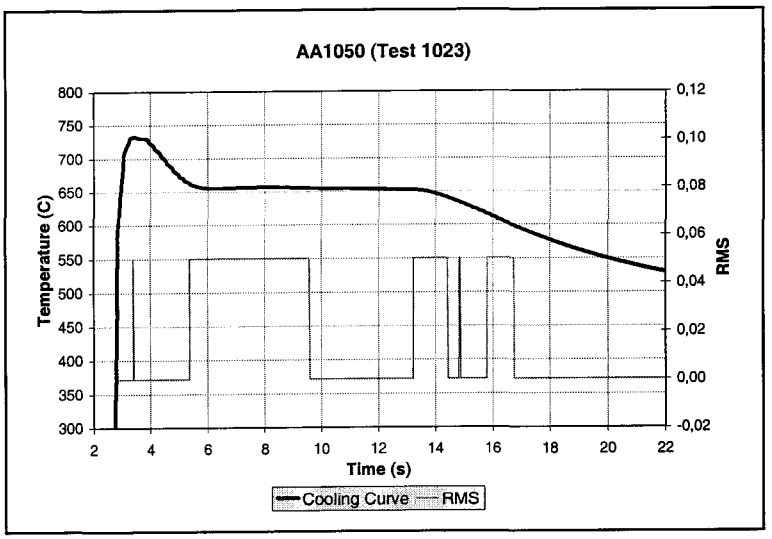
AA1050 (Test 1023)
Temperature (C)
RMS
Time (s)
Cooling Curve
RMS

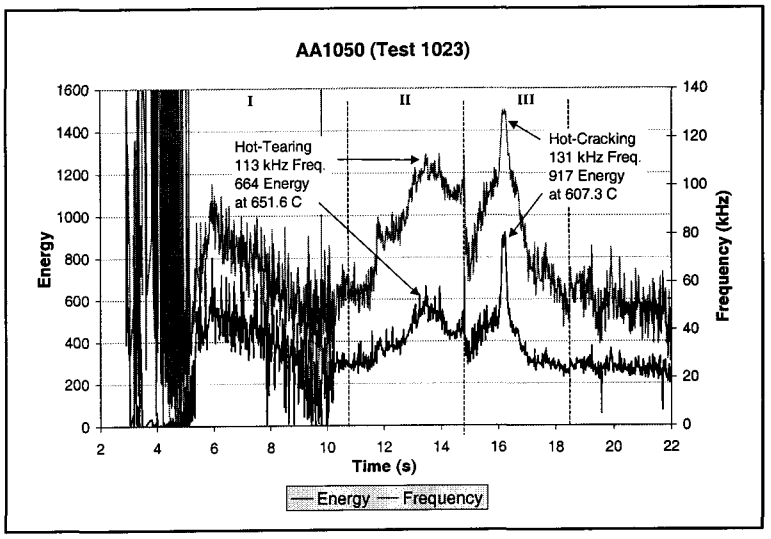
AA1050 (Test 1023)
I
II
III
Hot-Tearing
113 kHz Freq.
664 Energy
at 651.6 C
Hot-Cracking
131 kHz Freq.
917 Energy
at 607.3 C
Energy
Frequency (kHz)
Time (s)
Energy
Frequency

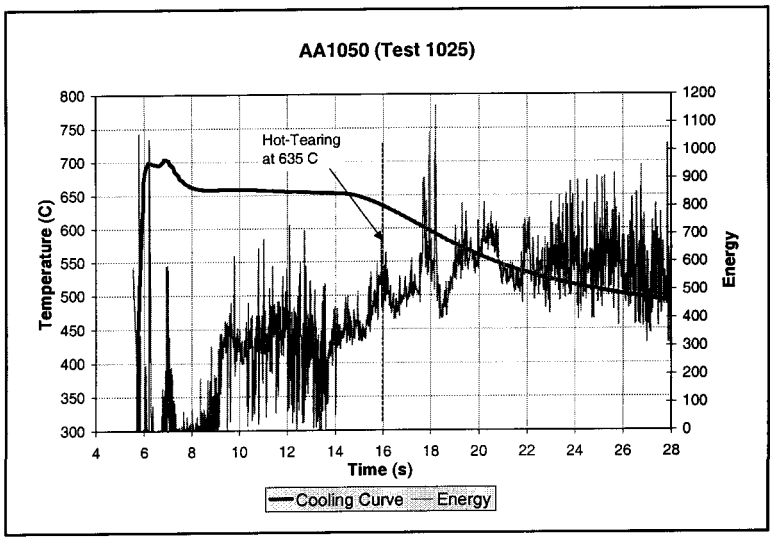
AA1050 (Test 1025)
Hot-Tearing
at 635 C
Temperature (C)
Energy
Time (s)
Cooling Curve
Energy

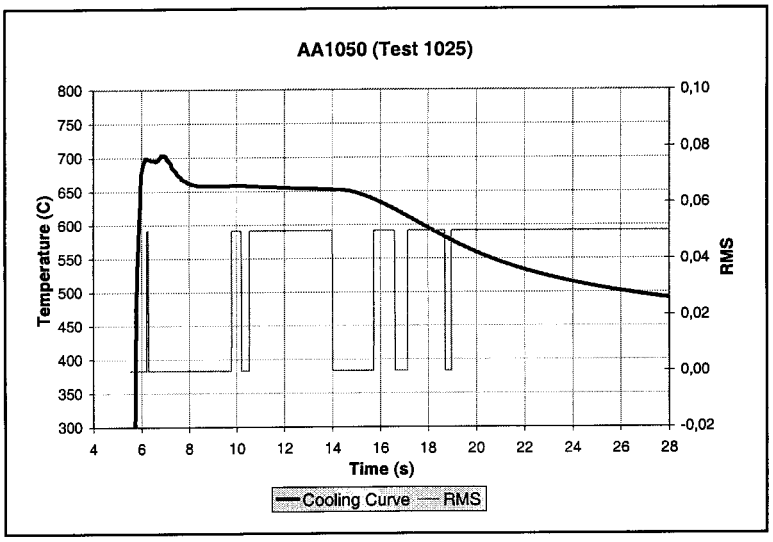
AA1050 (Test 1025)
Temperature (C)
RMS
Time (s)
Cooling Curve
RMS

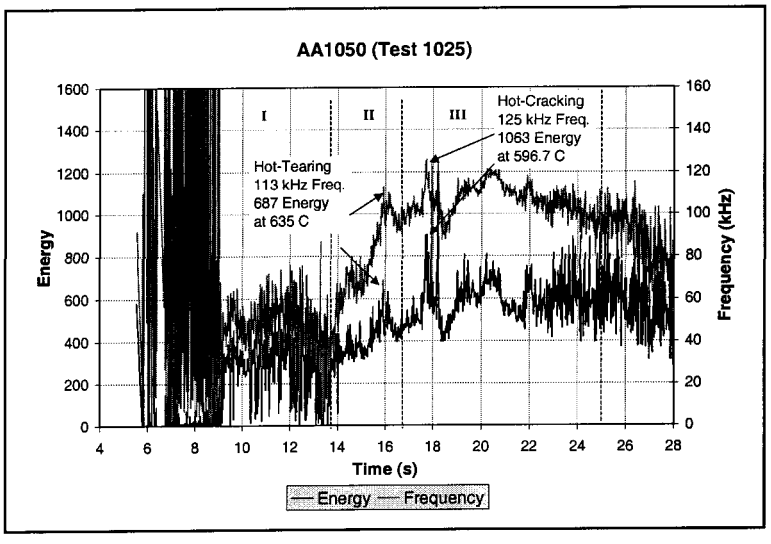
AA1050 (Test 1025)
I
II
III
Hot-Cracking
125 kHz Freq.
1063 Energy
at 596.7 C
Hot-Tearing
113 kHz Freq.
687 Energy
at 635 C
Energy
Frequency (kHz)
Time (s)
Energy
Frequency

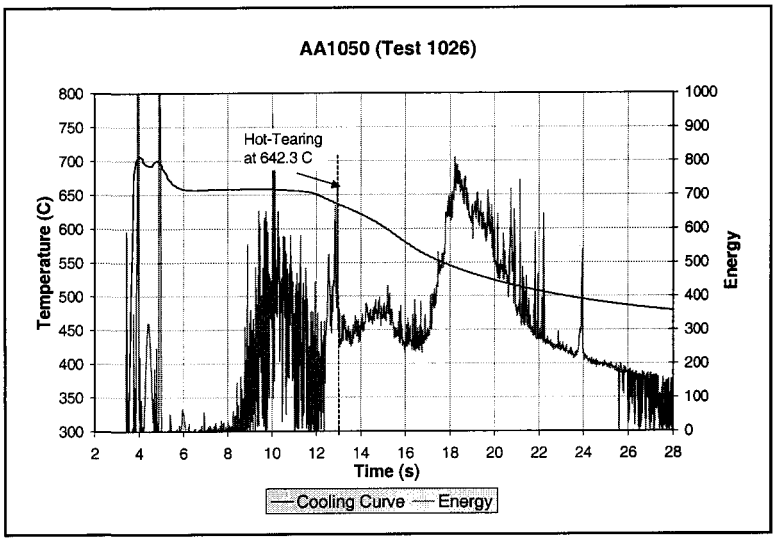
AA1050 (Test 1026)
Hot-Tearing
at 642.3 C
Temperature (C)
Energy
Time (s)
Cooling Curve
Energy

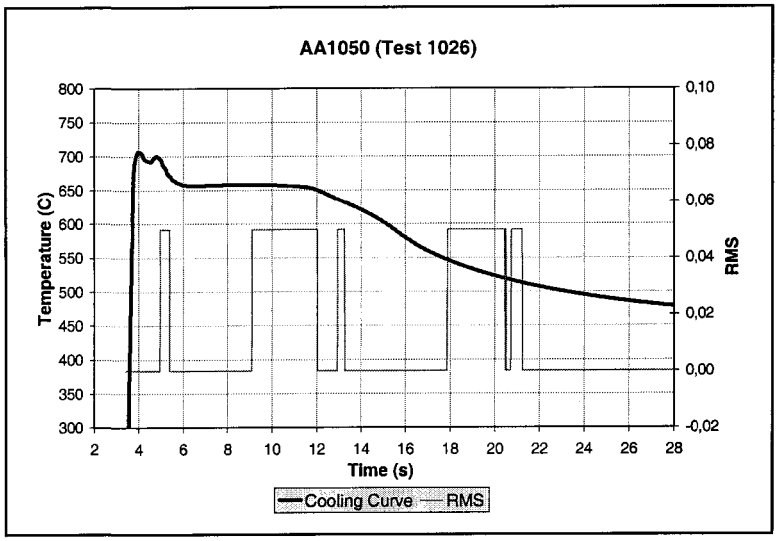
AA1050 (Test 1026)
Temperature (C)
RMS
Time (s)
Cooling Curve
RMS

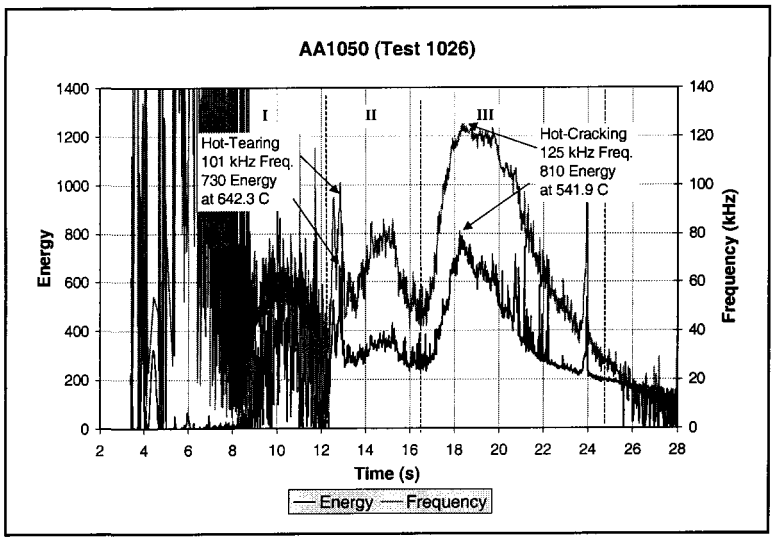
AA1050 (Test 1026)
I
II
III
Hot-Tearing
101 kHz Freq.
730 Energy
at 642.3 C
Hot-Cracking
125 kHz Freq.
810 Energy
at 541.9 C
Energy
Frequency (kHz)
Time (s)
Energy
Frequency

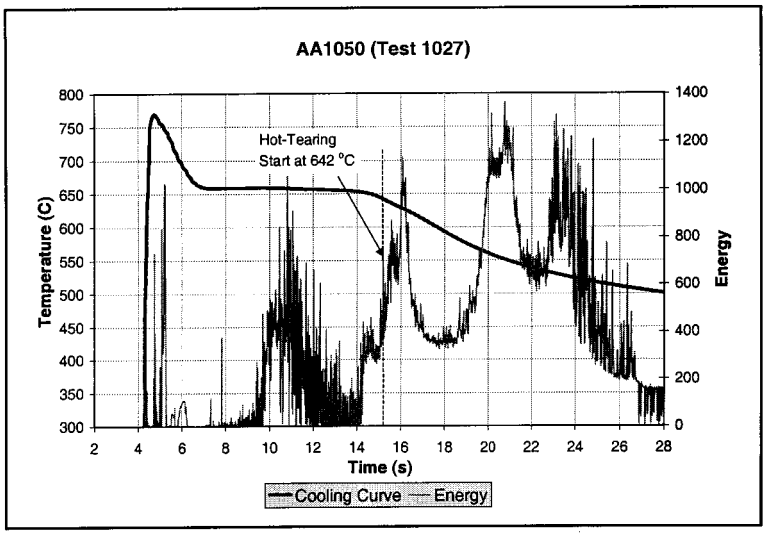
AA1050 (Test 1027)
Hot-Tearing
Start at 642 °C
Temperature (C)
Energy
Time (s)
Cooling Curve
Energy

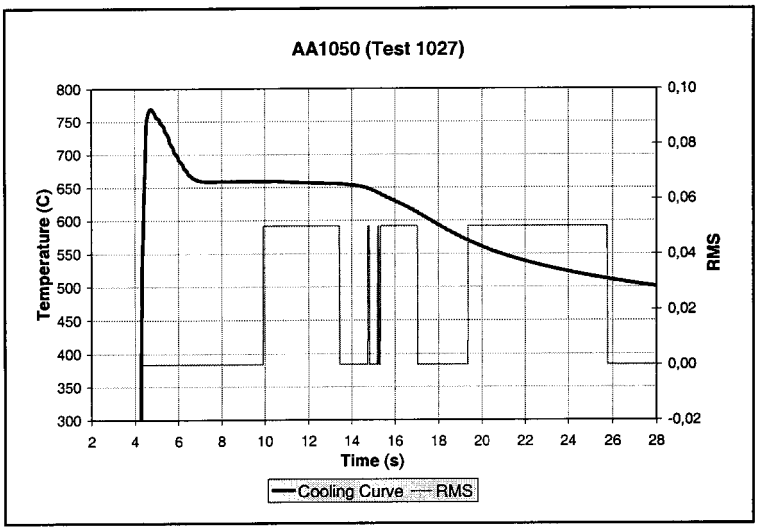
AA1050 (Test 1027)
Temperature (C)
RMS
Time (s)
Cooling Curve
RMS

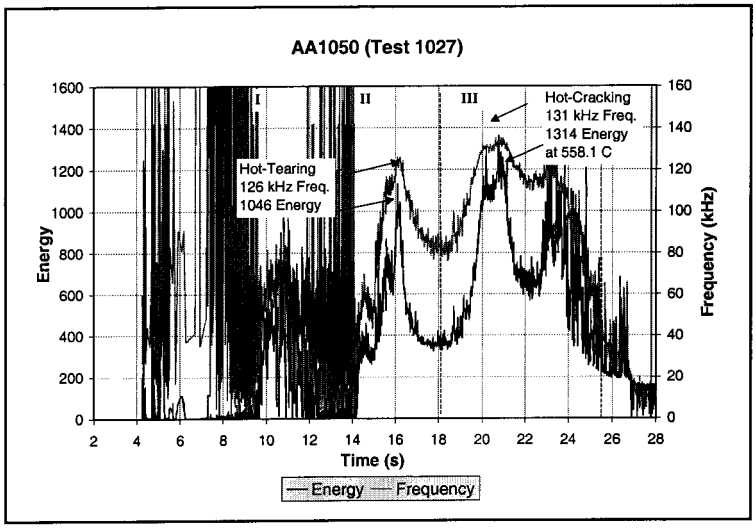
AA1050 (Test 1027)
I
II
III
Hot-Tearing
126 kHz Freq.
1046 Energy
Hot-Cracking
131 kHz Freq.
1314 Energy
at 558.1 C
Energy
Frequency (kHz)
Time (s)
Energy
Frequency

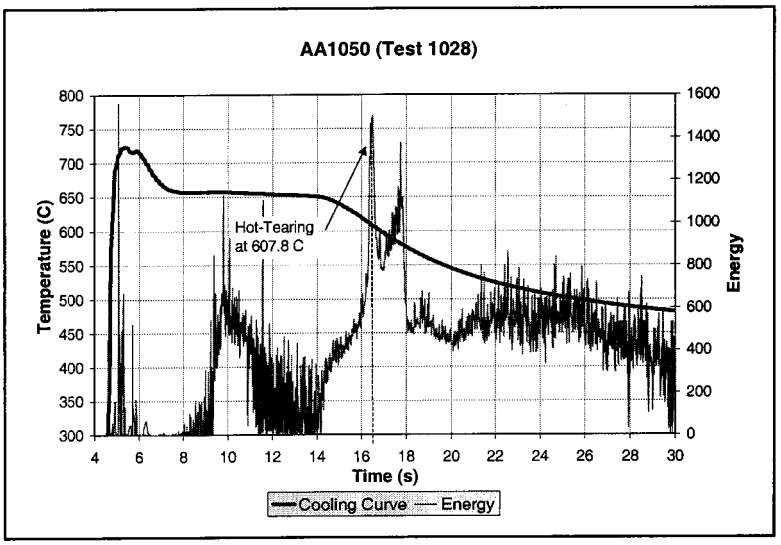
AA1050 (Test 1028)
Temperature (C)
Energy
Time (s)
Hot-Tearing
at 607.8 C
Cooling Curve
Energy

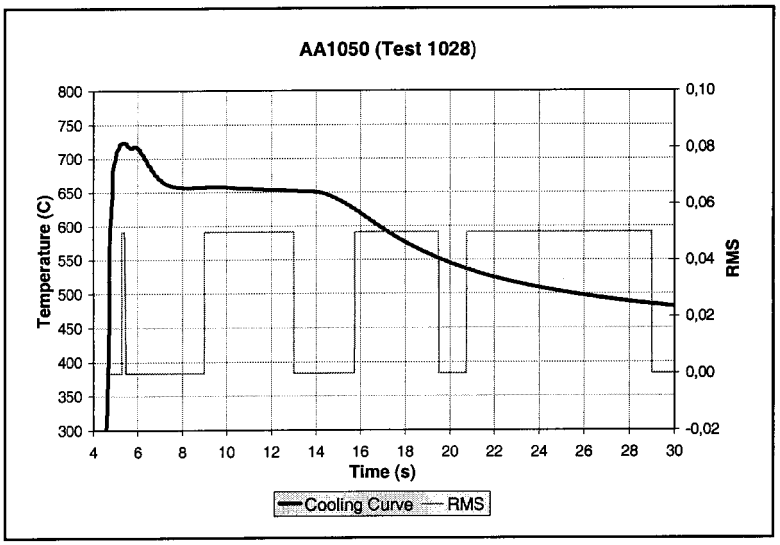
AA1050 (Test 1028)
Temperature (C)
RMS
Time (s)
Cooling Curve
RMS

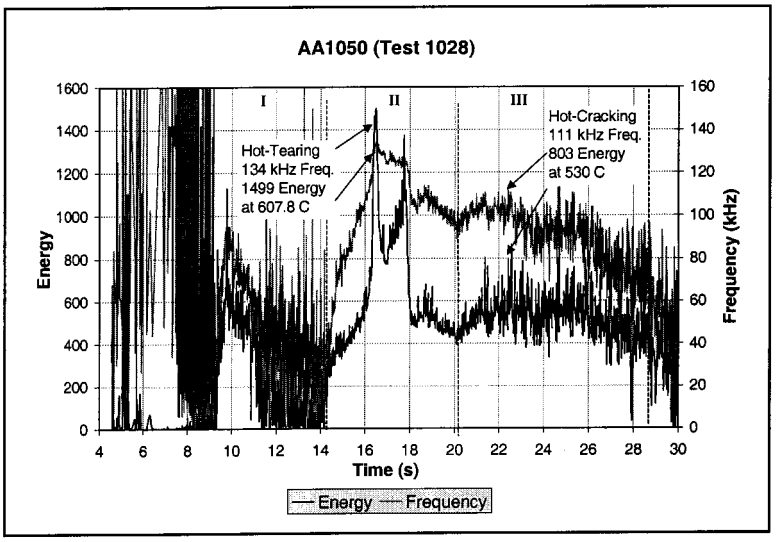
AA1050 (Test 1028)
I
II
III
Hot-Tearing
134 kHz Freq.
1499 Energy
at 607.8 C
Hot-Cracking
111 kHz Freq.
803 Energy
at 530 C
Energy
Frequency (kHz)
Time (s)
Energy
Frequency

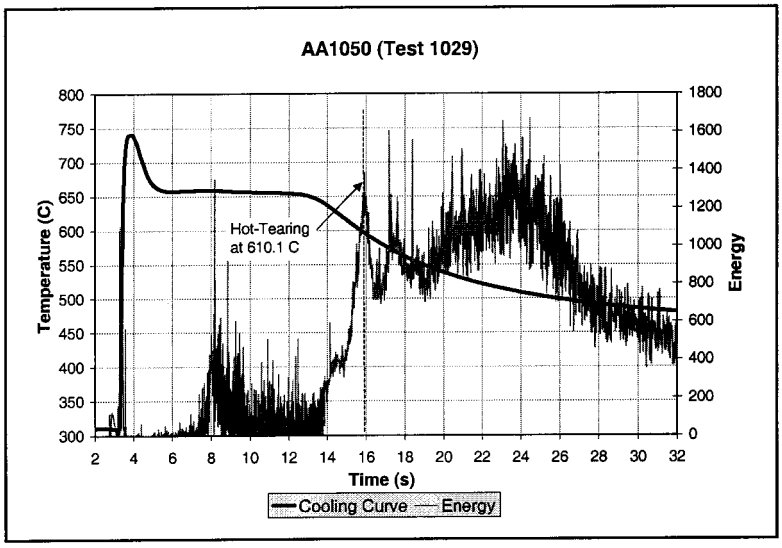
AA1050 (Test 1029)
Temperature (C)
Energy
Time (s)
Hot-Tearing
at 610.1 C
Cooling Curve
Energy

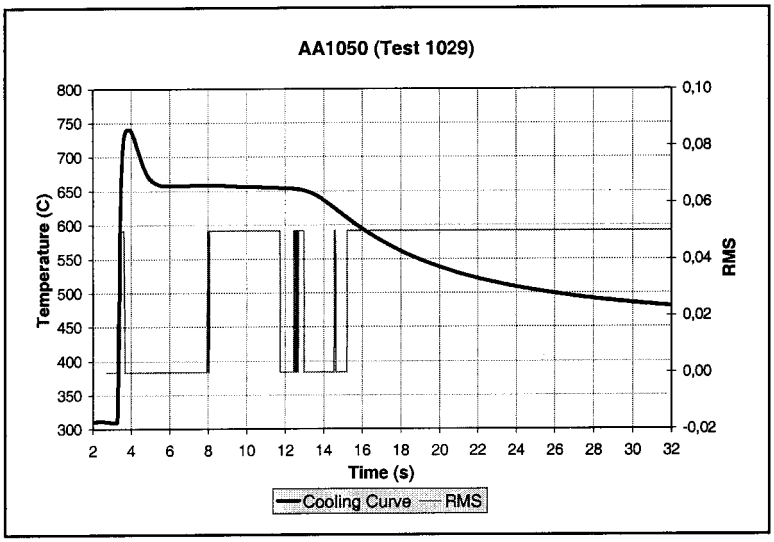
AA1050 (Test 1029)
Temperature (C)
RMS
Time (s)
Cooling Curve
RMS

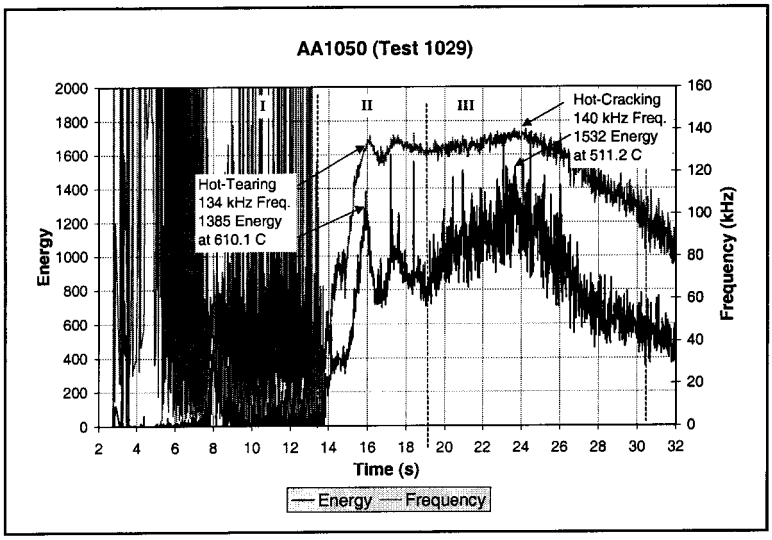
AA1050 (Test 1029)
Energy
Frequency (kHz)
Time (s)
I
II
III
Hot-Tearing
134 kHz Freq.
1385 Energy
at 610.1 C
Hot-Cracking
140 kHz Freq.
1532 Energy
at 511.2 C
Energy
Frequency

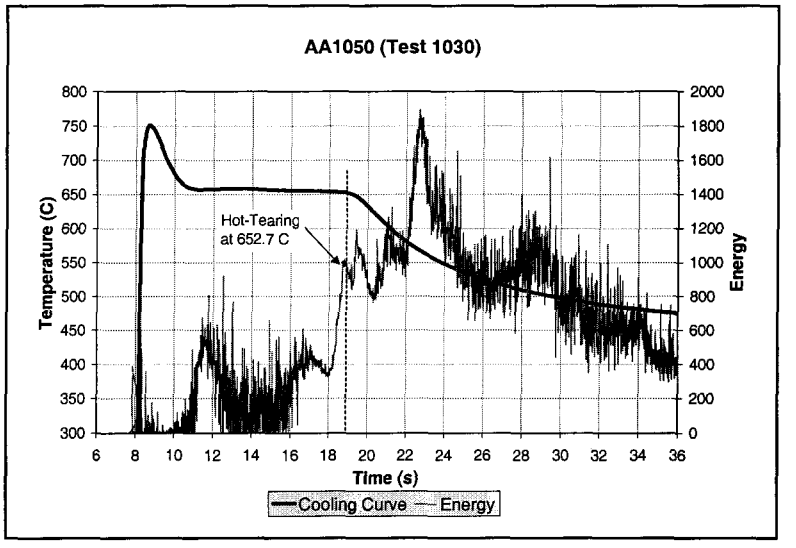
AA1050 (Test 1030)
Temperature (C)
Energy
Hot-Tearing
at 652.7 C
Time (s)
Cooling Curve
Energy

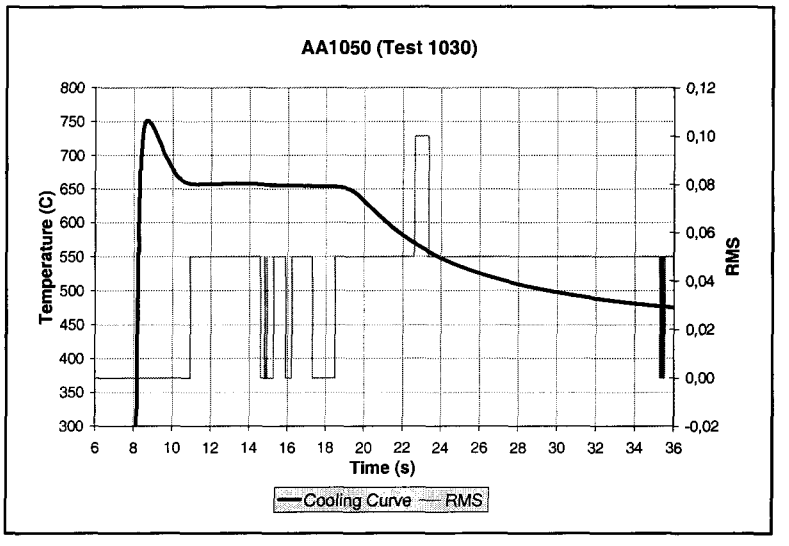
AA1050 (Test 1030)
Temperature (C)
RMS
Time (s)
Cooling Curve
RMS

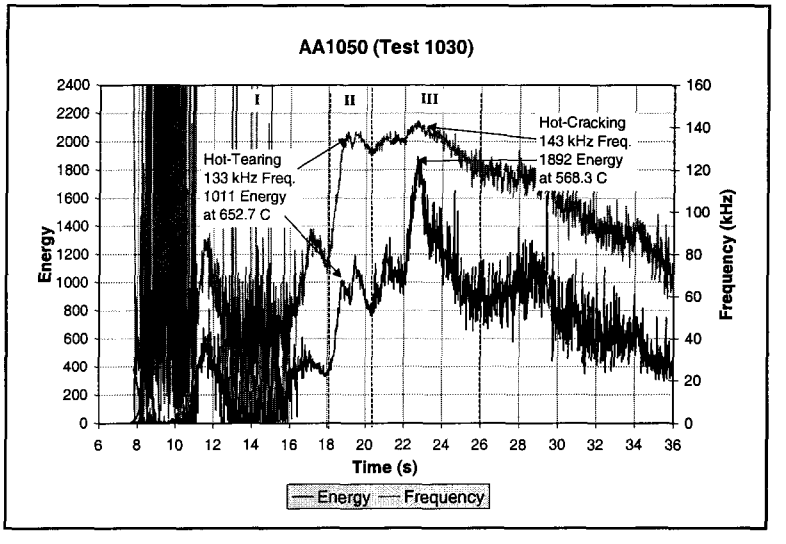
AA1050 (Test 1030)
I
II
III
Hot-Tearing
133 kHz Freq.
1011 Energy
at 652.7 C
Hot-Cracking
143 kHz Freq.
1892 Energy
at 568.3 C
Energy
Frequency (kHz)
Time (s)
Energy
Frequency

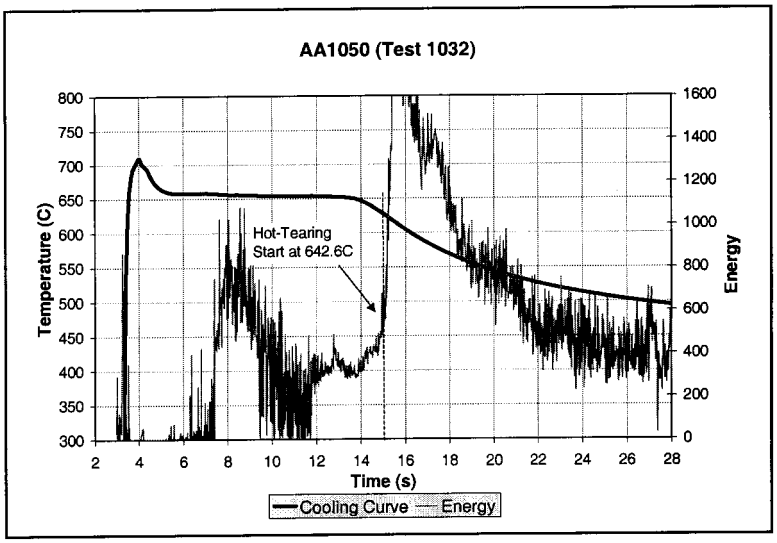
AA1050 (Test 1032)
Temperature (C)
Energy
Hot-Tearing
Start at 642.6C
Time (s)
Cooling Curve
Energy

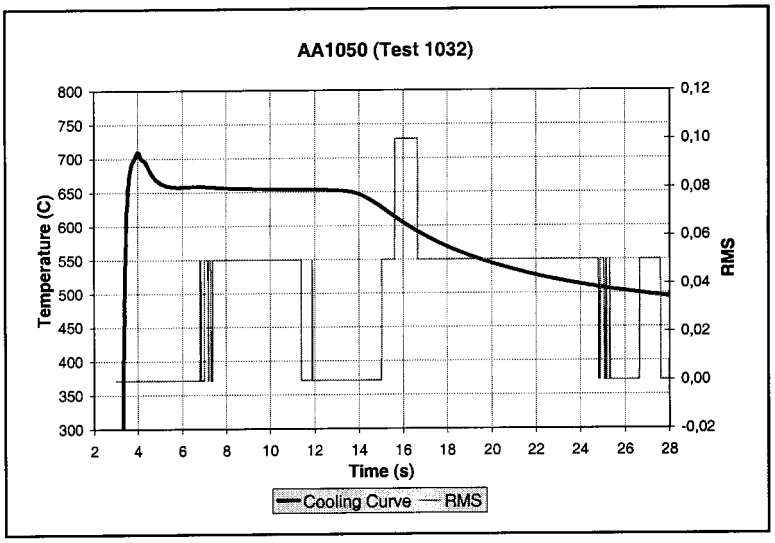
AA1050 (Test 1032)
Temperature (C)
RMS
Time (s)
Cooling Curve
RMS

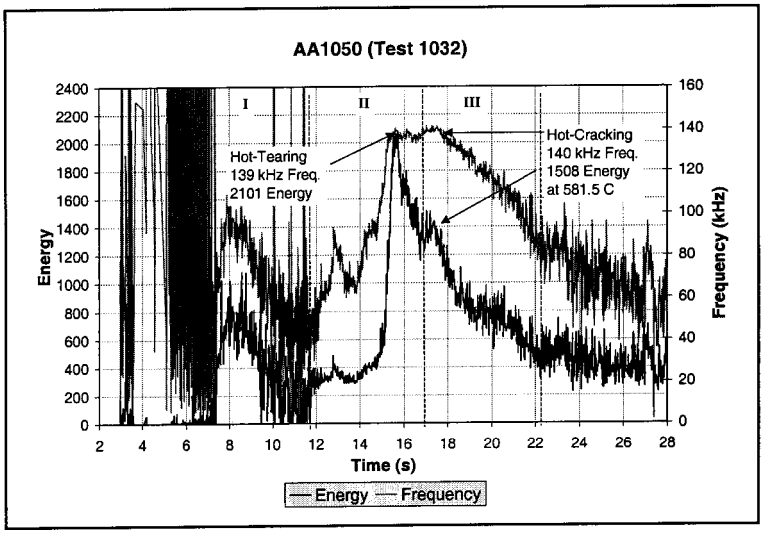
AA1050 (Test 1032)
I
II
III
Hot-Tearing
139 kHz Freq.
2101 Energy
Hot-Cracking
140 kHz Freq.
1508 Energy
at 581.5 C
Energy
Frequency (kHz)
Time (s)
Energy
Frequency

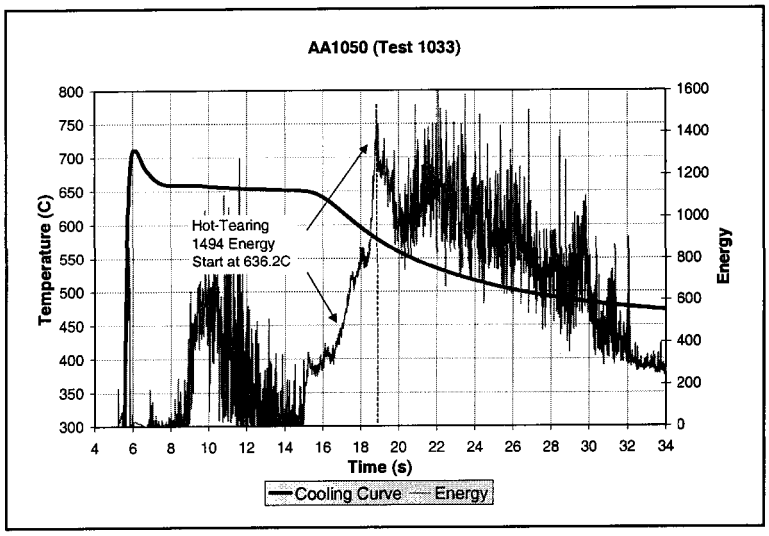
AA1050 (Test 1033)
Temperature (C)
Energy
Time (s)
Hot-Tearing
1494 Energy
Start at 636.2C
Cooling Curve
Energy

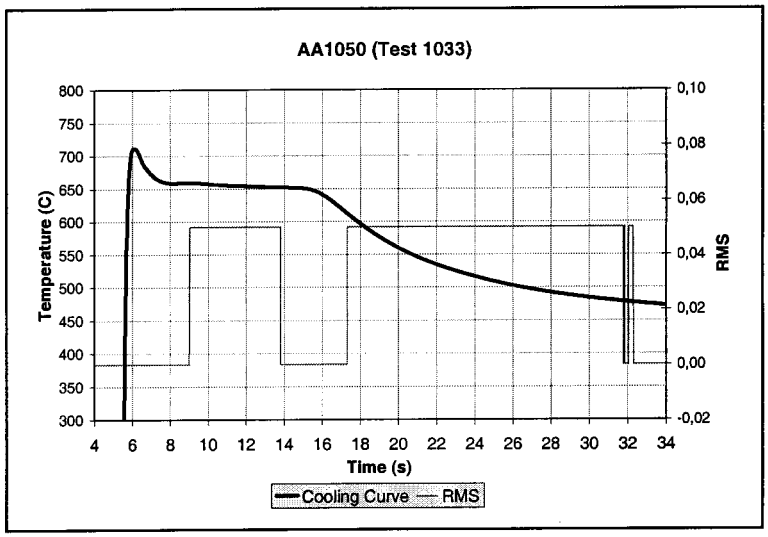
AA1050 (Test 1033)
Temperature (C)
RMS
Time (s)
Cooling Curve
RMS

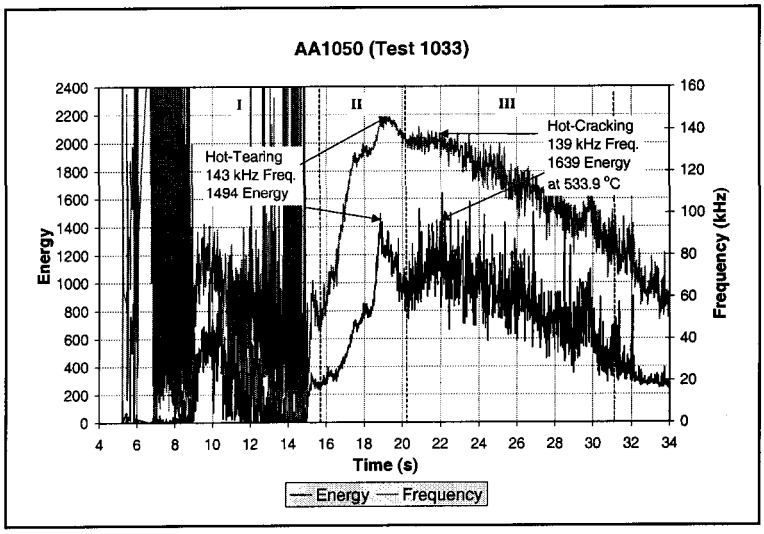
AA1050 (Test 1033)
Energy
Frequency (kHz)
Time (s)
I
II
III
Hot-Tearing
143 kHz Freq.
1494 Energy
Hot-Cracking
139 kHz Freq.
1639 Energy
at 533.9 °C
Energy
Frequency

Appendix II

Grain refiner test results of the superposition graphs of AE signals and the cooling/solidification curves (14 test results) :

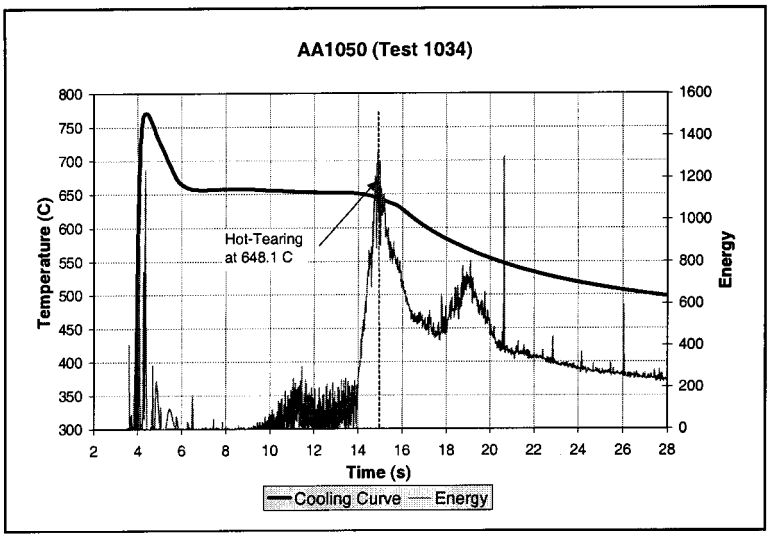
AA1050 (Test 1034)
Temperature (C)
Energy
Hot-Tearing
at 648.1 C
Time (s)
Cooling Curve
Energy

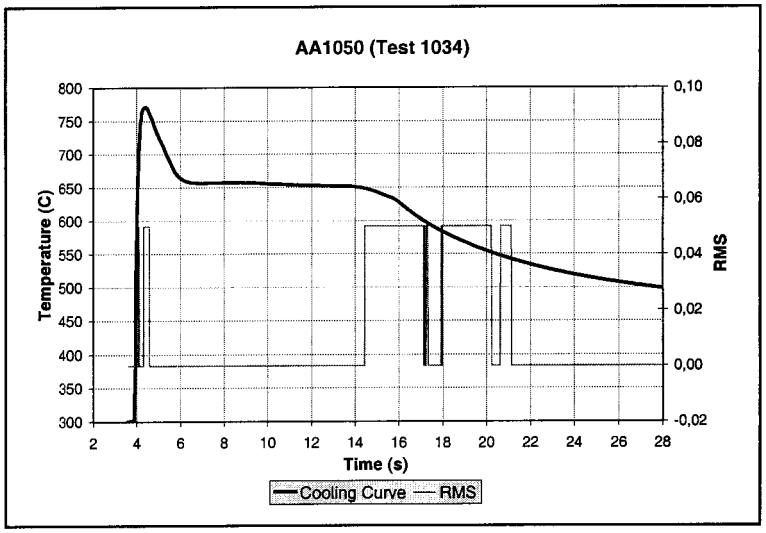
AA1050 (Test 1034)
Temperature (C)
RMS
Time (s)
Cooling Curve
RMS

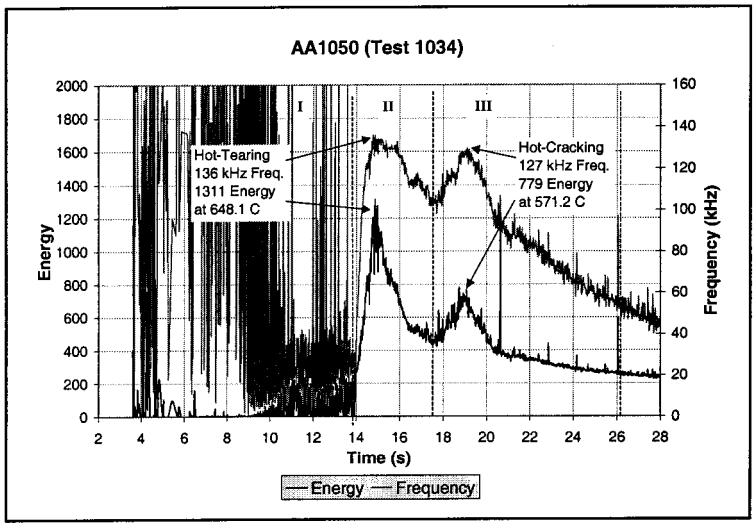
AA1050 (Test 1034)
I
II
III
Hot-Tearing
136 kHz Freq.
1311 Energy
at 648.1 C
Hot-Cracking
127 kHz Freq.
779 Energy
at 571.2 C
Energy
Frequency (kHz)
Time (s)
Energy
Frequency

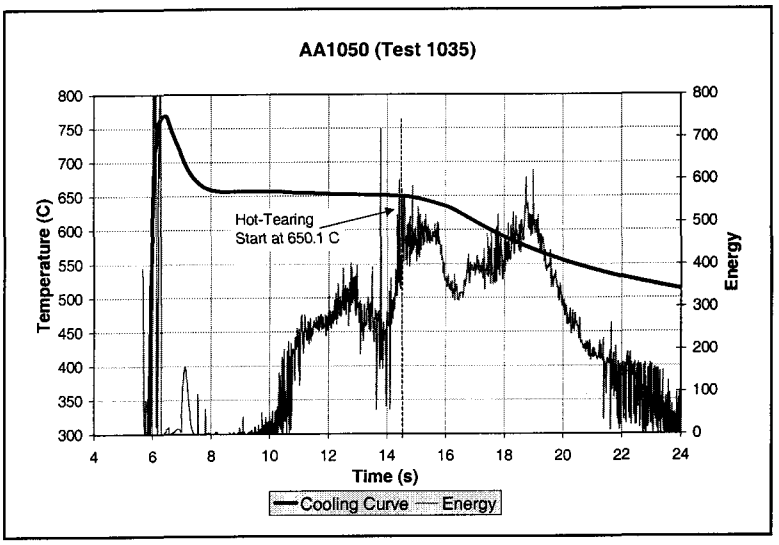
AA1050 (Test 1035)
Temperature (C)
Energy
Time (s)
Hot-Tearing
Start at 650.1 C
Cooling Curve
Energy

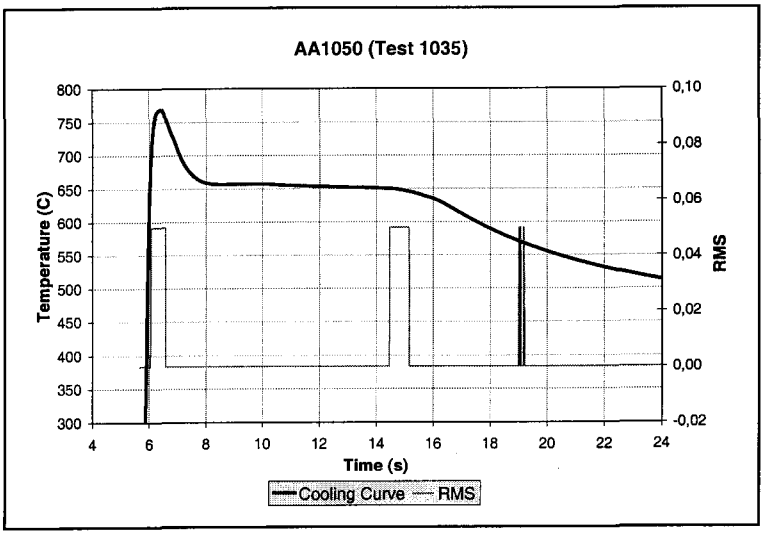
AA1050 (Test 1035)
Temperature (C)
RMS
Time (s)
Cooling Curve
RMS

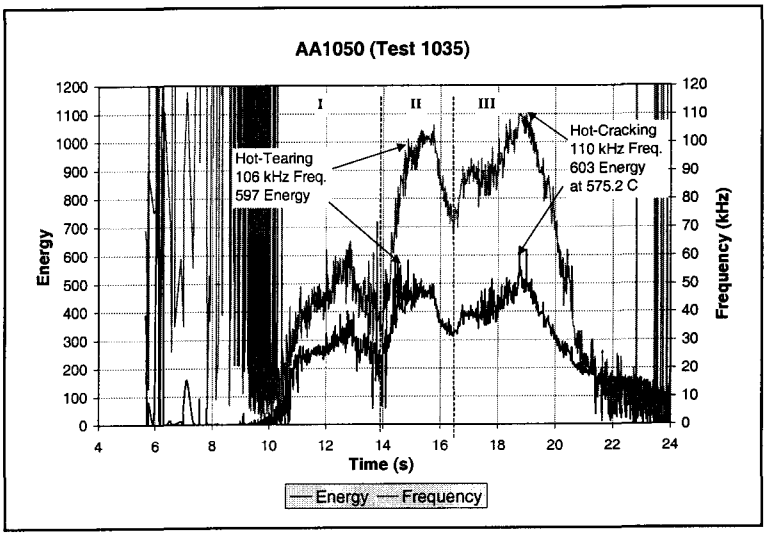
AA1050 (Test 1035)
Energy
Frequency (kHz)
Time (s)
I
II
III
Hot-Tearing
106 kHz Freq.
597 Energy
Hot-Cracking
110 kHz Freq.
603 Energy
at 575.2 C
Energy
Frequency

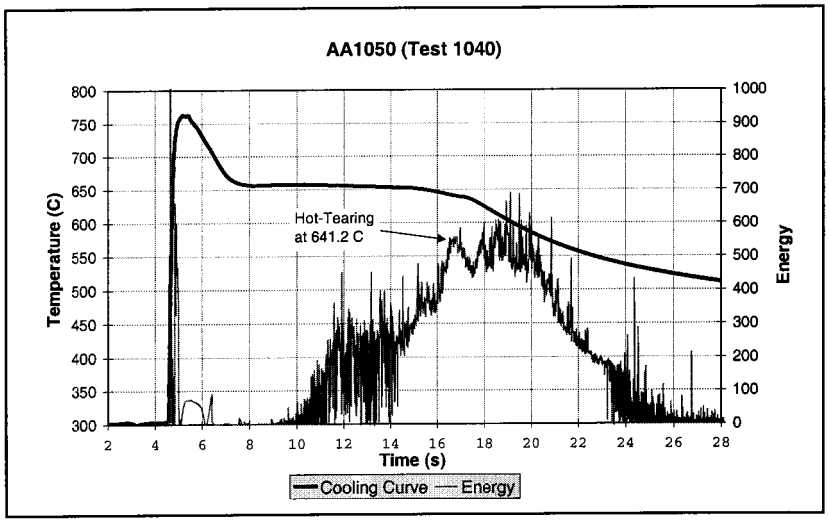
AA1050 (Test 1040)
Temperature (C)
Energy
Time (s)
Hot-Tearing
at 641.2 C
Cooling Curve
Energy

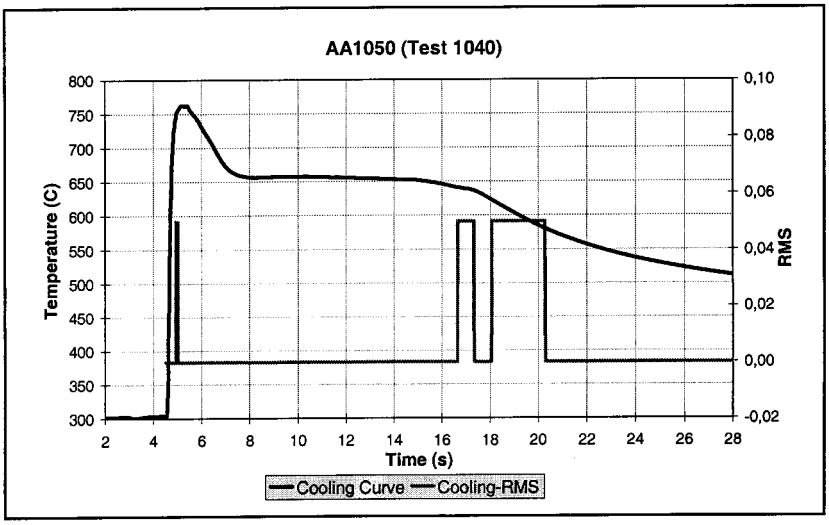
AA1050 (Test 1040)
Temperature (C)
RMS
Time (s)
Cooling Curve
Cooling-RMS

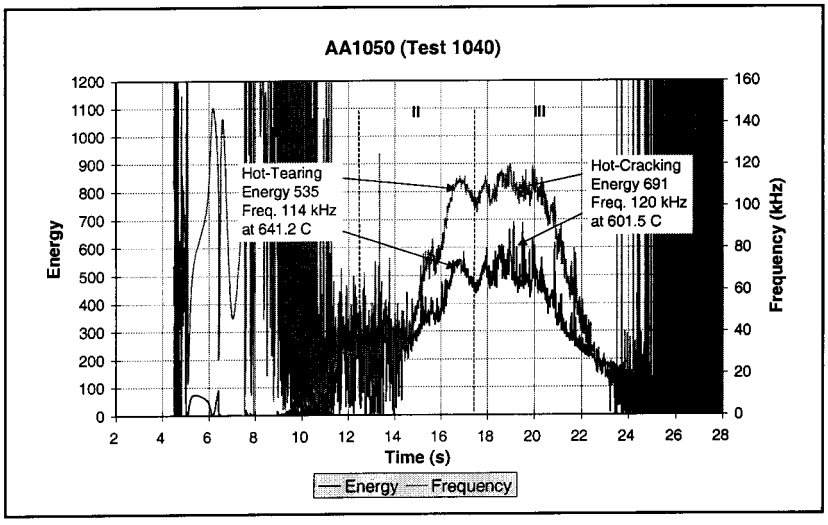
AA1050 (Test 1040)
Energy
Frequency (kHz)
Time (s)
II
III
Hot-Tearing
Energy 535
Freq. 114 kHz
at 641.2 C
Hot-Cracking
Energy 691
Freq. 120 kHz
at 601.5 C
Energy
Frequency

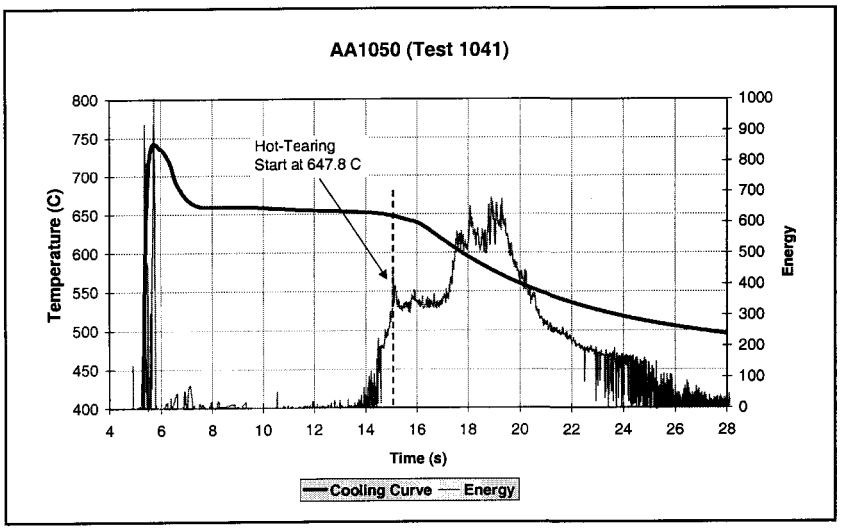
AA1050 (Test 1041)
Hot-Tearing
Start at 647.8 C
Temperature (C)
Energy
Time (s)
Cooling Curve
Energy

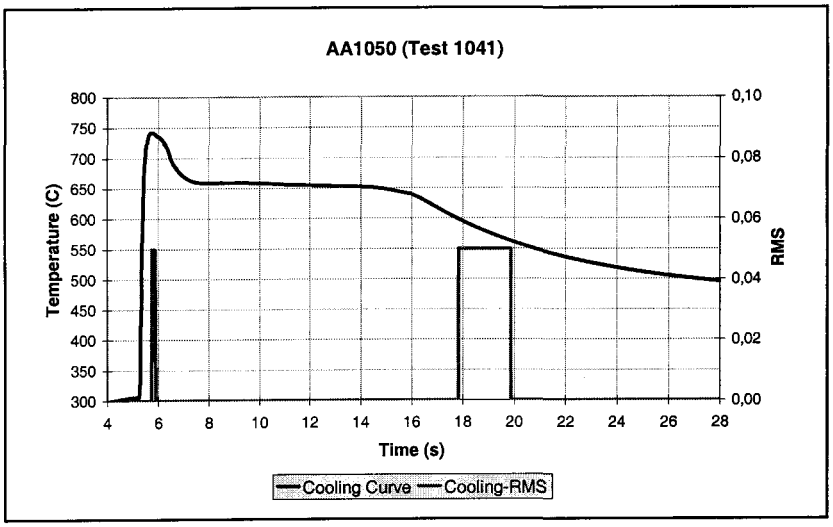
AA1050 (Test 1041)
Temperature (C)
RMS
Time (s)
Cooling Curve
Cooling-RMS

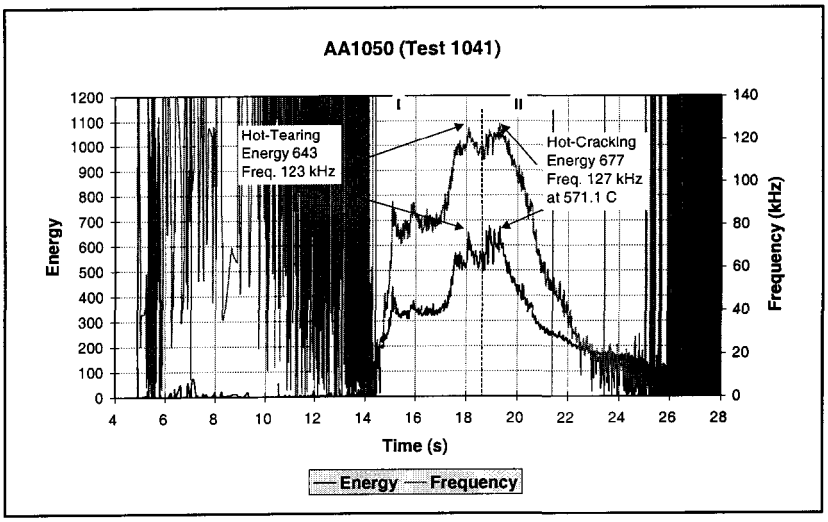
AA1050 (Test 1041)
Hot-Tearing
Energy 643
Freq. 123 kHz
Hot-Cracking
Energy 677
Freq. 127 kHz
at 571.1 C
I
II
Energy
Frequency (kHz)
Time (s)
Energy
Frequency

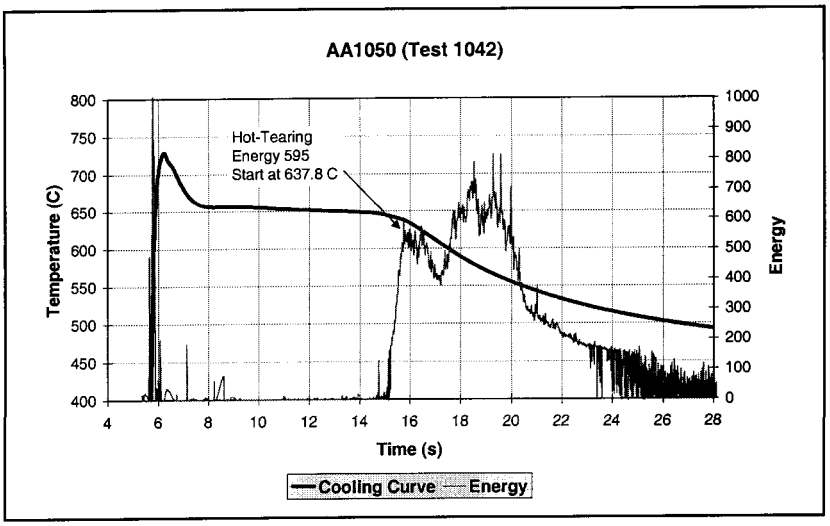
AA1050 (Test 1042)
Hot-Tearing
Energy 595
Start at 637.8 C
Temperature (C)
Energy
Time (s)
Cooling Curve
Energy

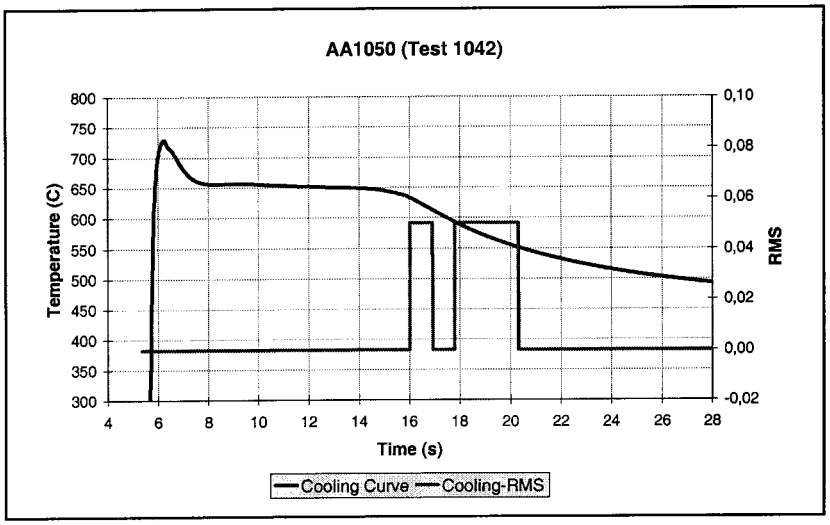
AA1050 (Test 1042)
Temperature (C)
RMS
Time (s)
Cooling Curve
Cooling-RMS

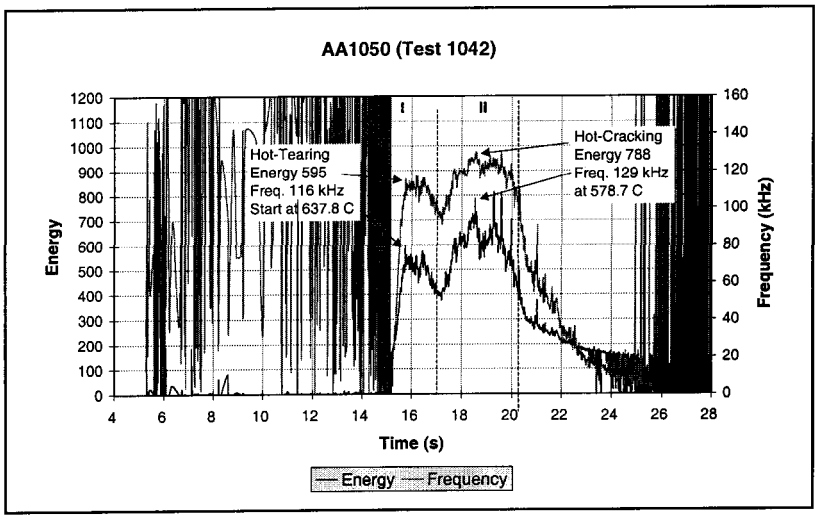
AA1050 (Test 1042)
I
II
Hot-Tearing
Energy 595
Freq. 116 kHz
Start at 637.8 C
Hot-Cracking
Energy 788
Freq. 129 kHz
at 578.7 C
Energy
Frequency (kHz)
Time (s)
Energy
Frequency

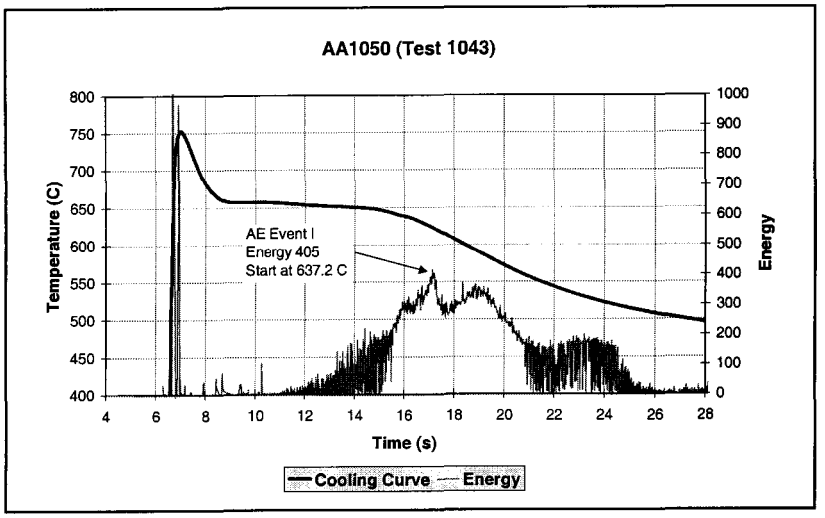
AA1050 (Test 1043)
Temperature (C)
Energy
Time (s)
AE Event I
Energy 405
Start at 637.2 C
Cooling Curve
Energy

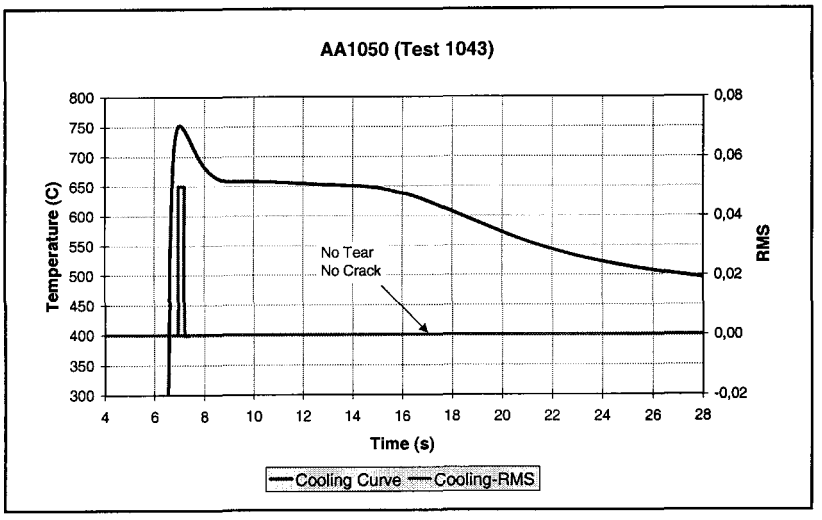
AA1050 (Test 1043)
Temperature (C)
RMS
Time (s)
No Tear
No Crack
Cooling Curve
Cooling-RMS

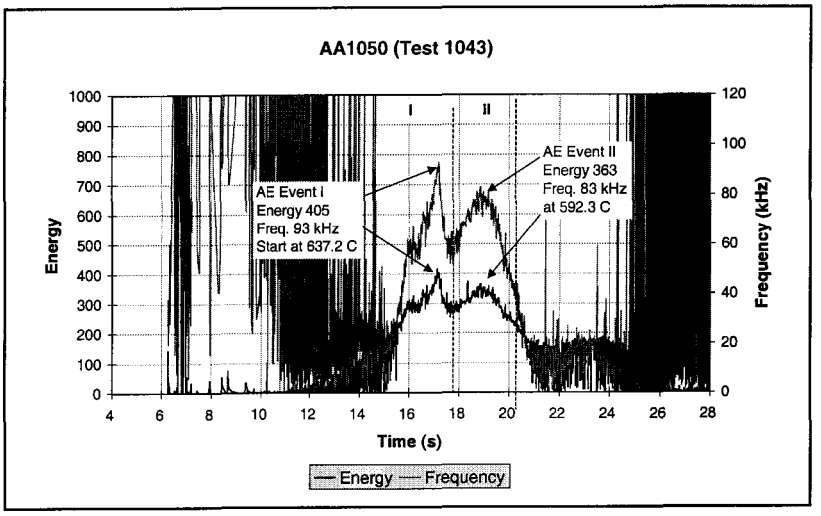
AA1050 (Test 1043)
Energy
Frequency (kHz)
Time (s)
I
II
AE Event I
Energy 405
Freq. 93 kHz
Start at 637.2 C
AE Event II
Energy 363
Freq. 83 kHz
at 592.3 C
Energy
Frequency

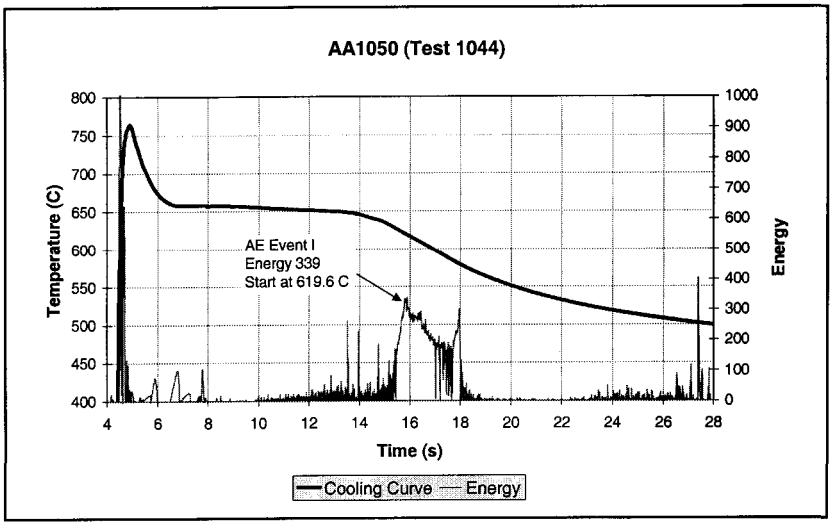
AA1050 (Test 1044)
Temperature (C)
Energy
Time (s)
AE Event I
Energy 339
Start at 619.6 C
Cooling Curve
Energy

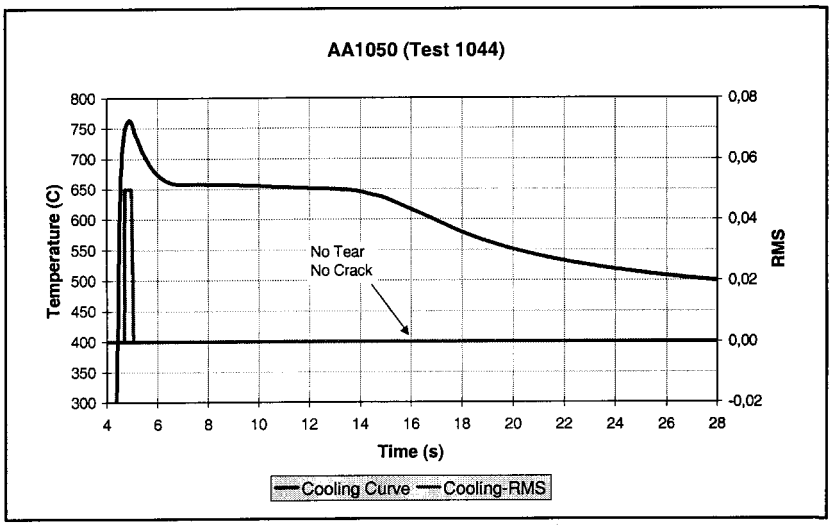
AA1050 (Test 1044)
Temperature (C)
RMS
Time (s)
No Tear
No Crack
Cooling Curve
Cooling-RMS

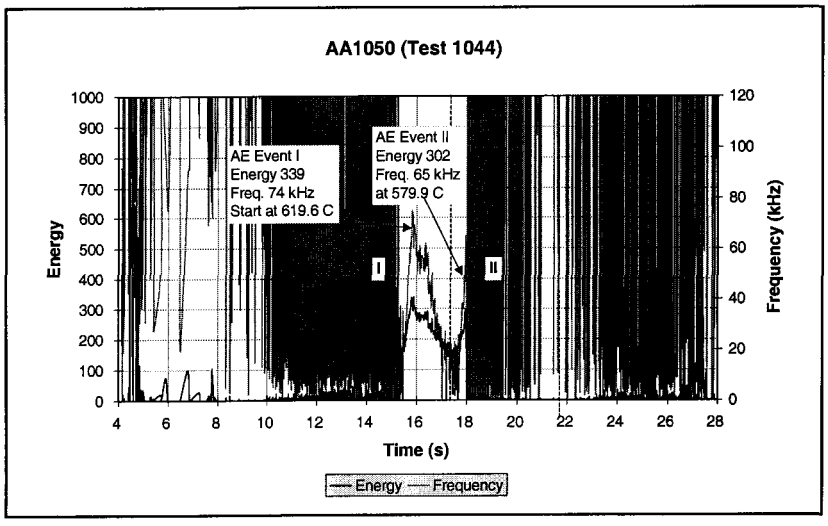
AA1050 (Test 1044)
Energy
Frequency (kHz)
Time (s)
AE Event I
Energy 339
Freq. 74 kHz
Start at 619.6 C
AE Event II
Energy 302
Freq. 65 kHz
at 579.9 C
I
II
Energy
Frequency

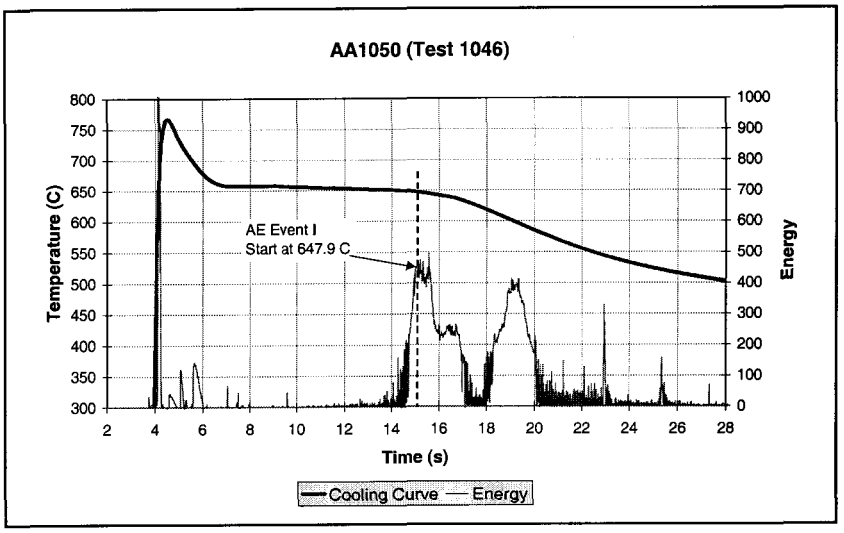
AA1050 (Test 1046)
Temperature (C)
Energy
AE Event I
Start at 647.9 C
Time (s)
Cooling Curve
Energy

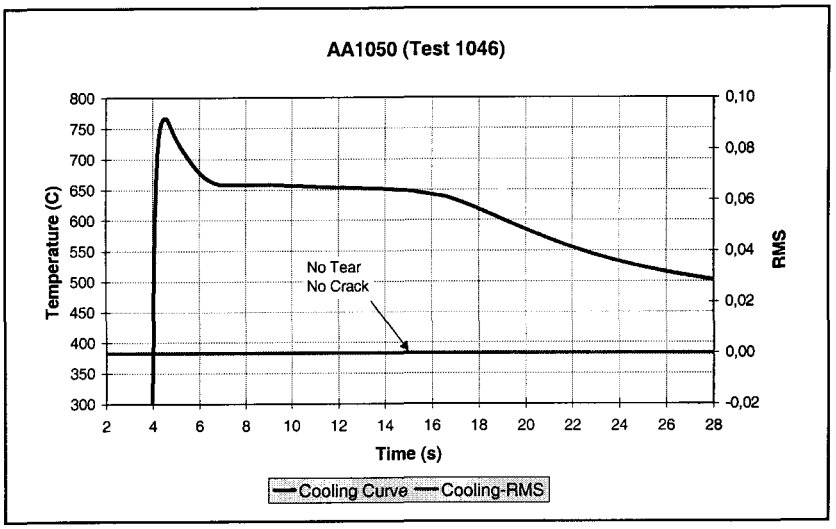
AA1050 (Test 1046)
Temperature (C)
RMS
No Tear
No Crack
Time (s)
Cooling Curve
Cooling-RMS

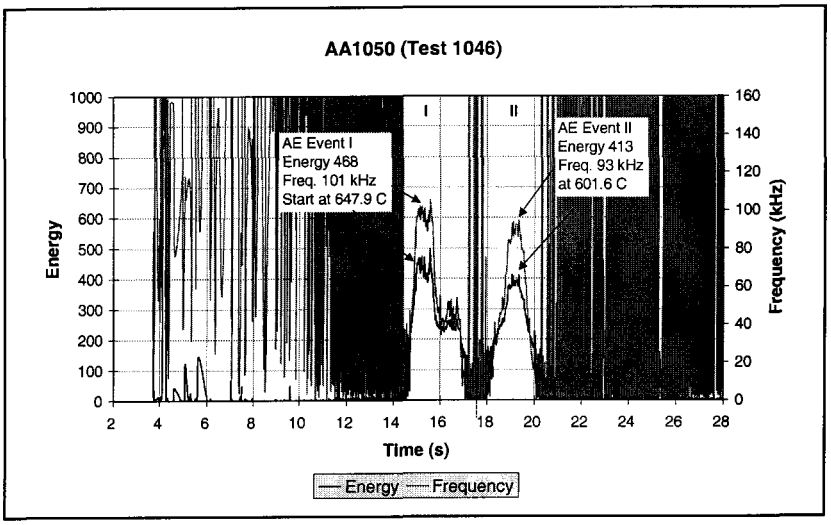
AA1050 (Test 1046)
Energy
Frequency (kHz)
I
II
AE Event I
Energy 468
Freq. 101 kHz
Start at 647.9 C
AE Event II
Energy 413
Freq. 93 kHz
at 601.6 C
Time (s)
Energy
Frequency

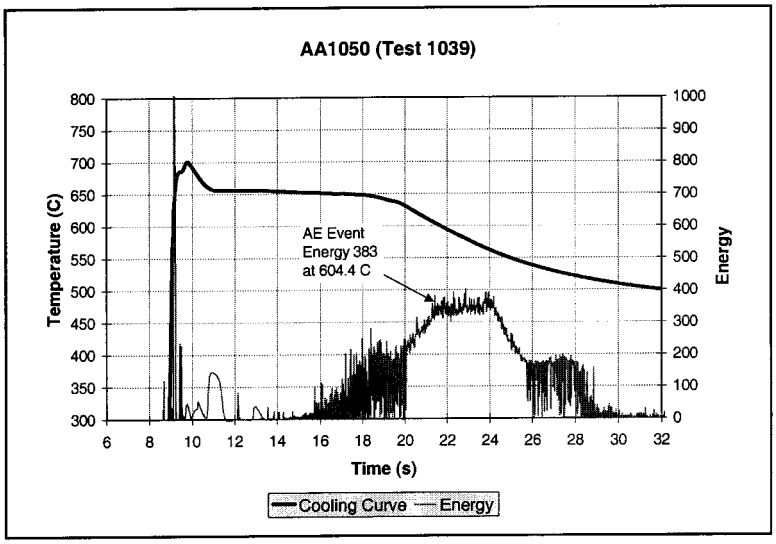
AA1050 (Test 1039)
Temperature (C)
Energy
AE Event
Energy 383
at 604.4 C
Time (s)
Cooling Curve
Energy

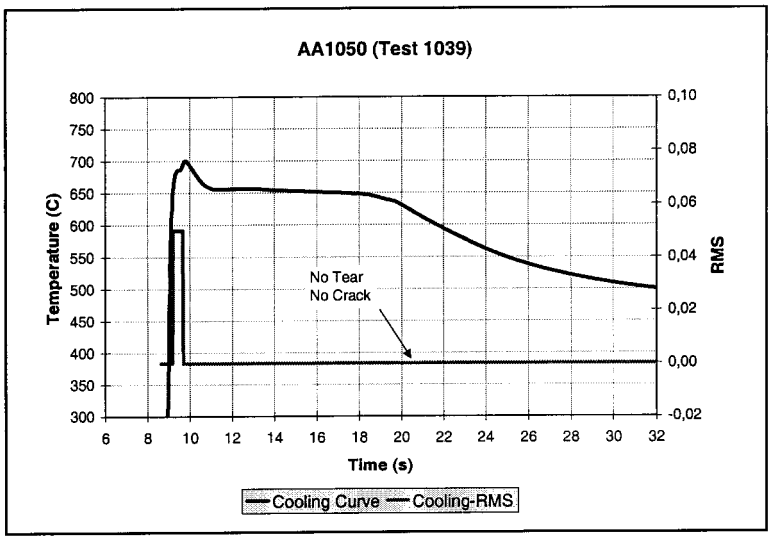
AA1050 (Test 1039)
Temperature (C)
RMS
No Tear
No Crack
Time (s)
Cooling Curve
Cooling-RMS

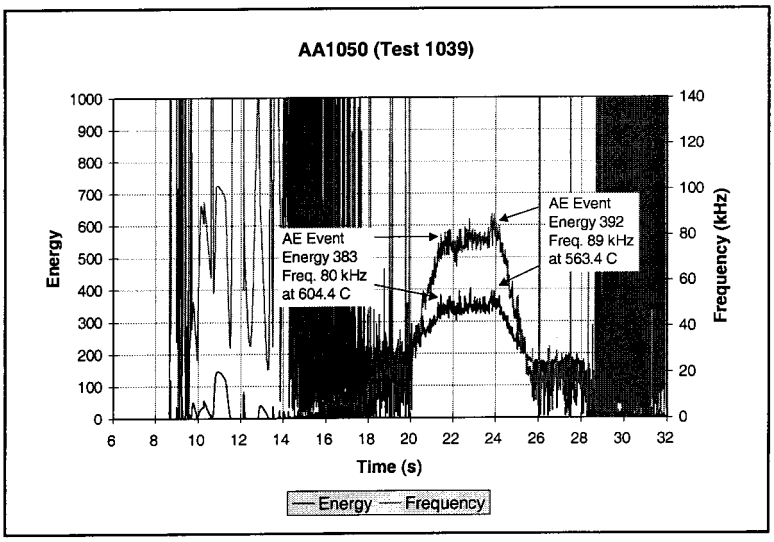
AA1050 (Test 1039)
Energy
Frequency (kHz)
AE Event
Energy 383
Freq. 80 kHz
at 604.4 C
AE Event
Energy 392
Freq. 89 kHz
at 563.4 C
Time (s)
Energy
Frequency

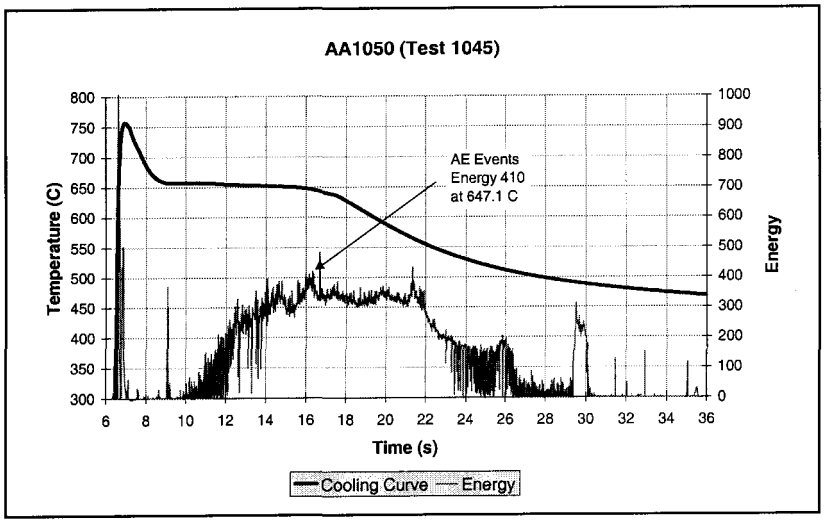
AA1050 (Test 1045)
Temperature (C)
Energy
Time (s)
AE Events
Energy 410
at 647.1 C
Cooling Curve
Energy

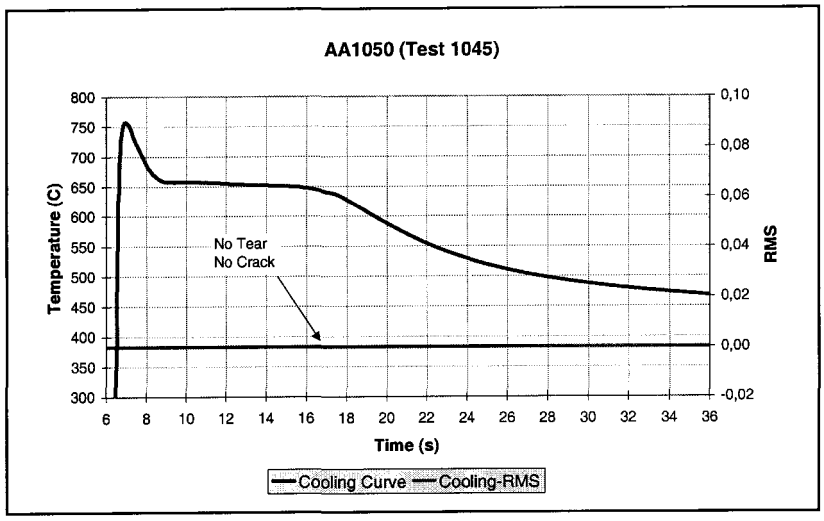
AA1050 (Test 1045)
Temperature (C)
RMS
Time (s)
No Tear
No Crack
Cooling Curve
Cooling-RMS

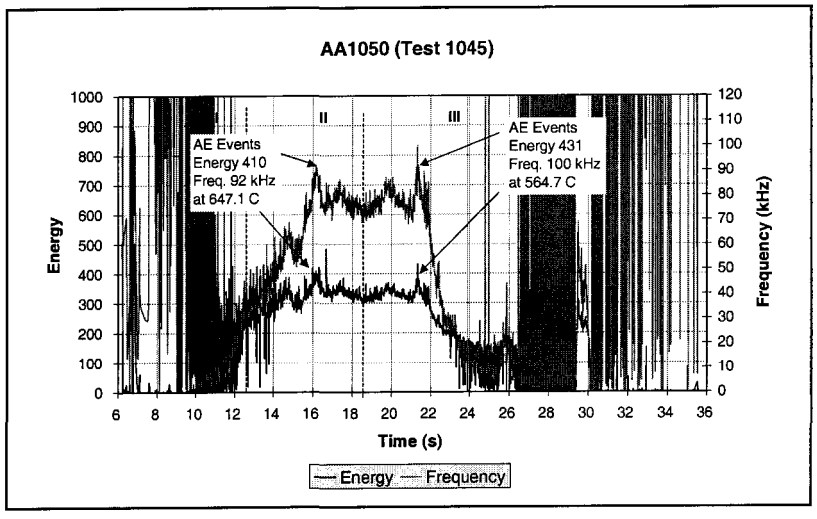
AA1050 (Test 1045)
Energy
Frequency (kHz)
Time (s)
II
III
AE Events
Energy 410
Freq. 92 kHz
at 647.1 C
AE Events
Energy 431
Freq. 100 kHz
at 564.7 C
Energy
Frequency

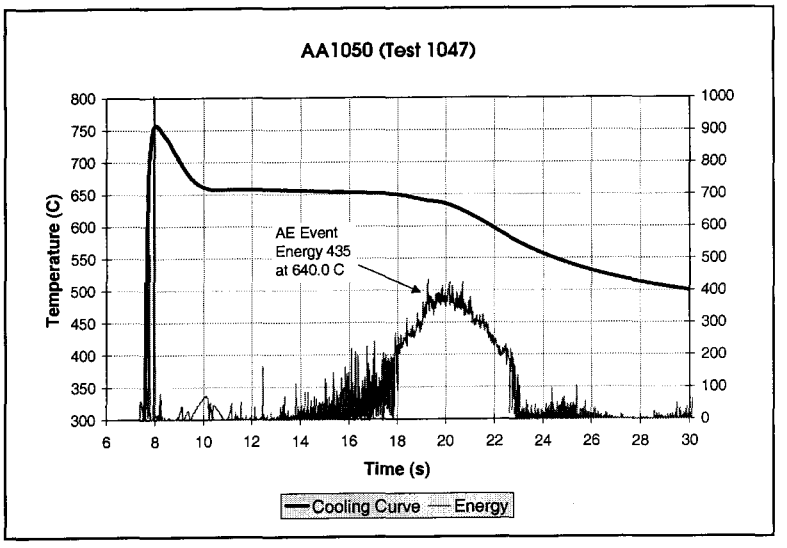
AA1050 (Test 1047)
Temperature (C)
Time (s)
AE Event
Energy 435
at 640.0 C
Cooling Curve
Energy

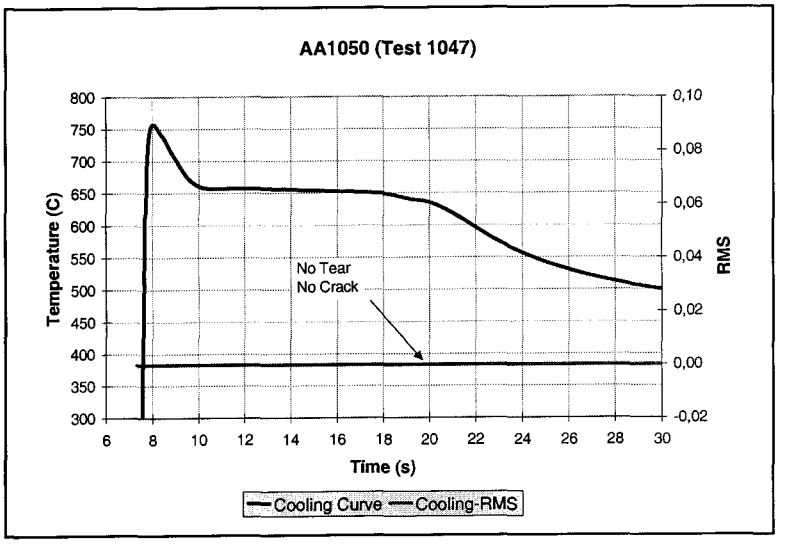
AA1050 (Test 1047)
Temperature (C)
RMS
Time (s)
No Tear
No Crack
Cooling Curve
Cooling-RMS

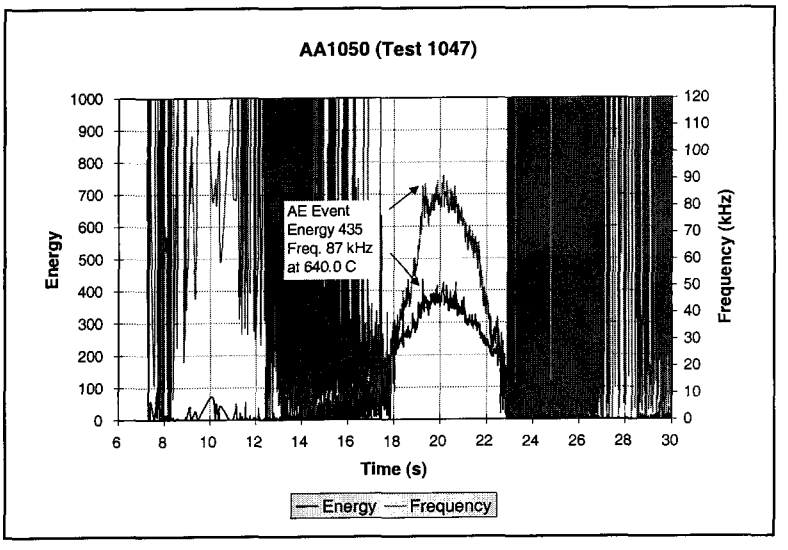
AA1050 (Test 1047)
Energy
Frequency (kHz)
Time (s)
AE Event
Energy 435
Freq. 87 kHz
at 640.0 C
Energy
Frequency

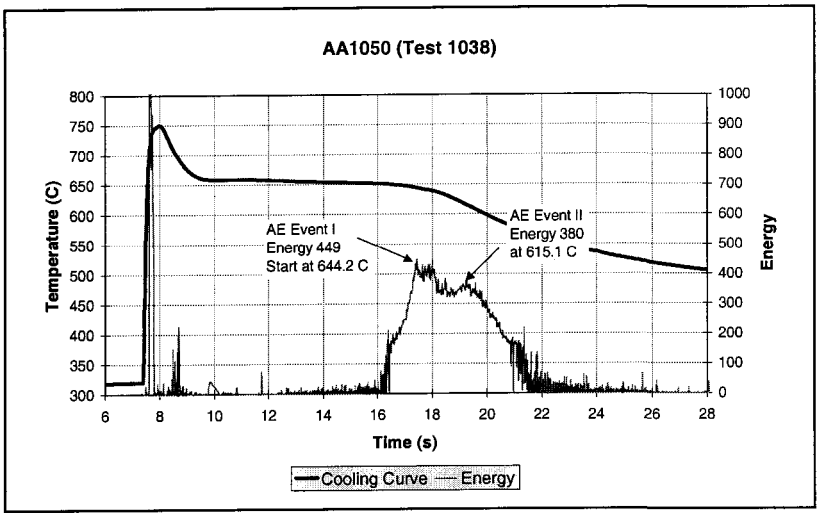
AA1050 (Test 1038)
Temperature (C)
Energy
Time (s)
AE Event I
Energy 449
Start at 644.2 C
AE Event II
Energy 380
at 615.1 C
Cooling Curve
Energy

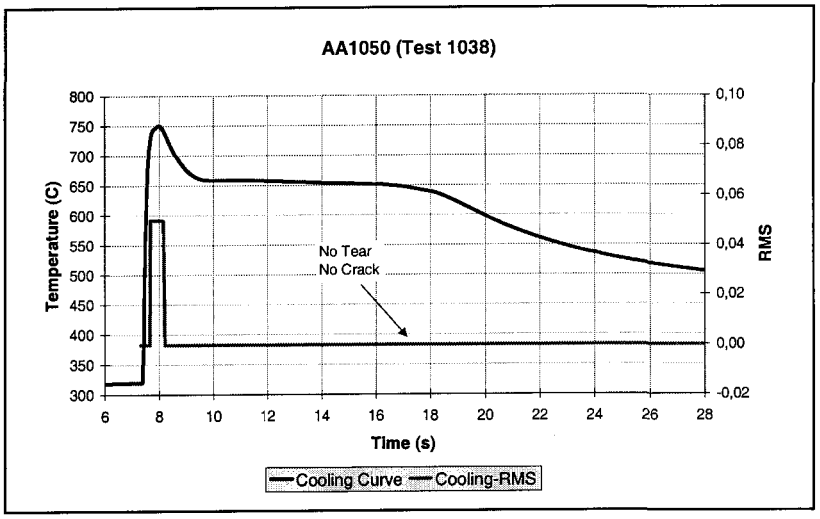
AA1050 (Test 1038)
Temperature (C)
RMS
Time (s)
No Tear
No Crack
Cooling Curve
Cooling-RMS

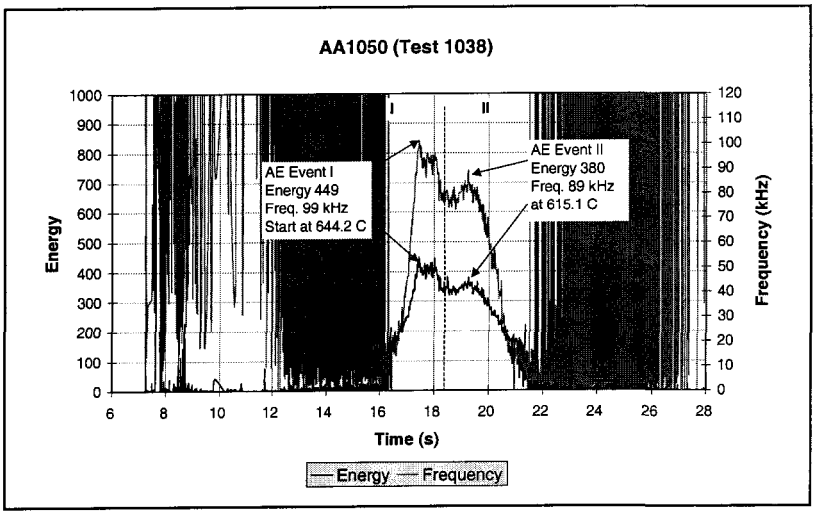
AA1050 (Test 1038)
Energy
Frequency (kHz)
Time (s)
I
II
AE Event I
Energy 449
Freq. 99 kHz
Start at 644.2 C
AE Event II
Energy 380
Freq. 89 kHz
at 615.1 C
Energy
Frequency

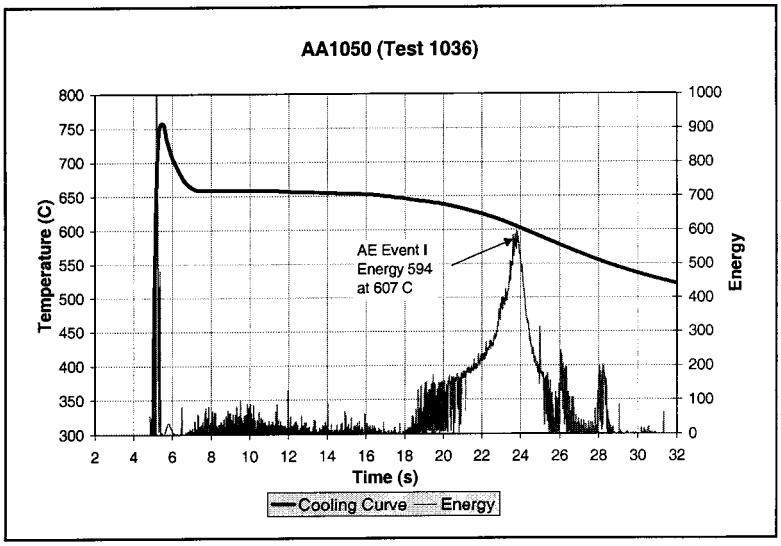
AA1050 (Test 1036)
Temperature (C)
Energy
AE Event I
Energy 594
at 607 C
Time (s)
Cooling Curve
Energy

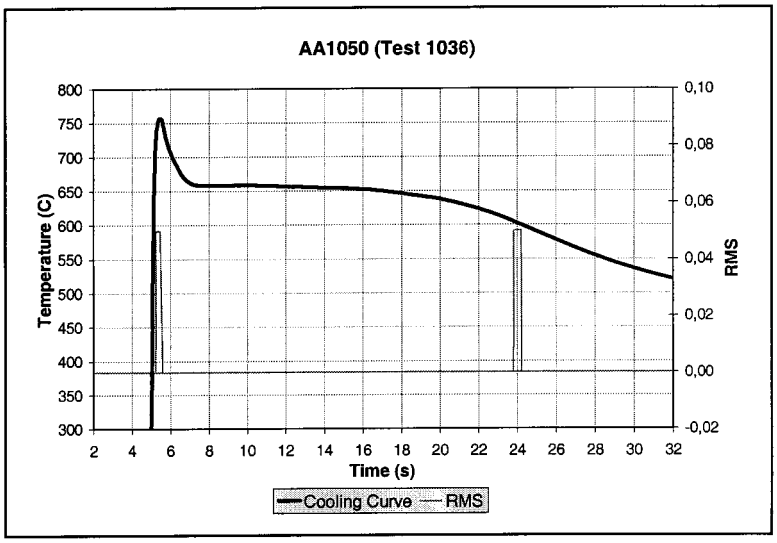
AA1050 (Test 1036)
Temperature (C)
RMS
Time (s)
Cooling Curve
RMS

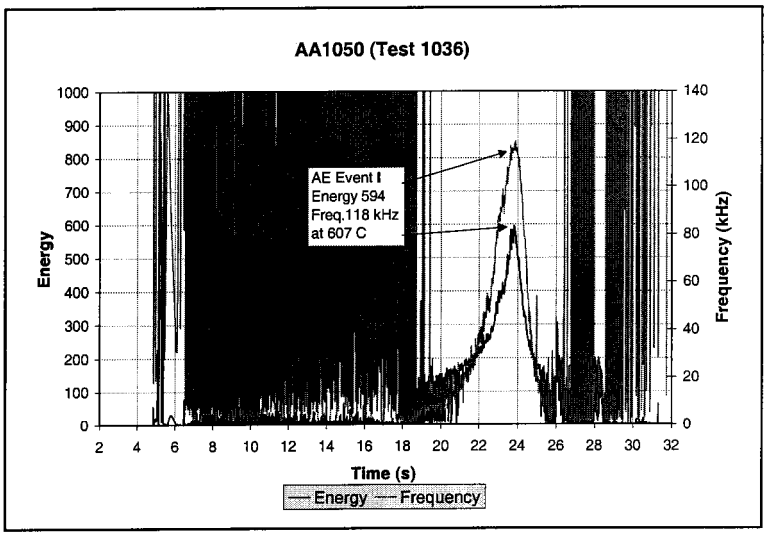
AA1050 (Test 1036)
Energy
Frequency (kHz)
AE Event I
Energy 594
Freq.118 kHz
at 607 C
Time (s)
Energy
Frequency

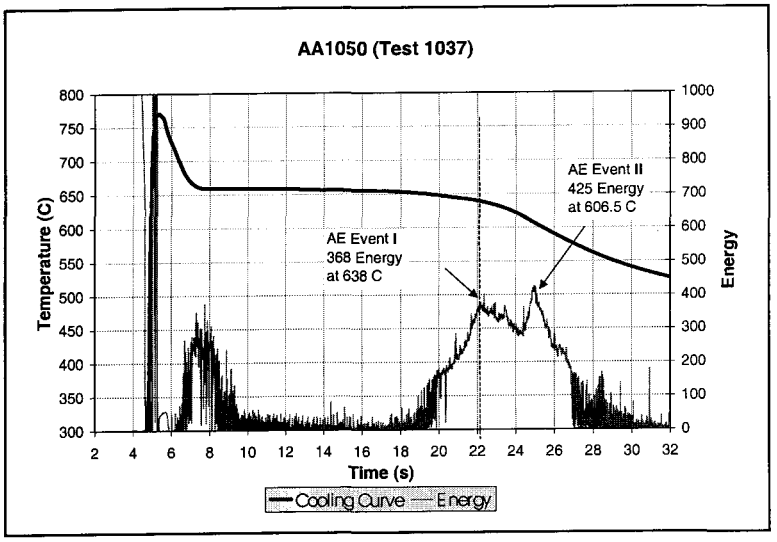
AA1050 (Test 1037)
Temperature (C)
Energy
Time (s)
AE Event I
368 Energy
at 638 C
AE Event II
425 Energy
at 606.5 C
Cooling Curve
Energy

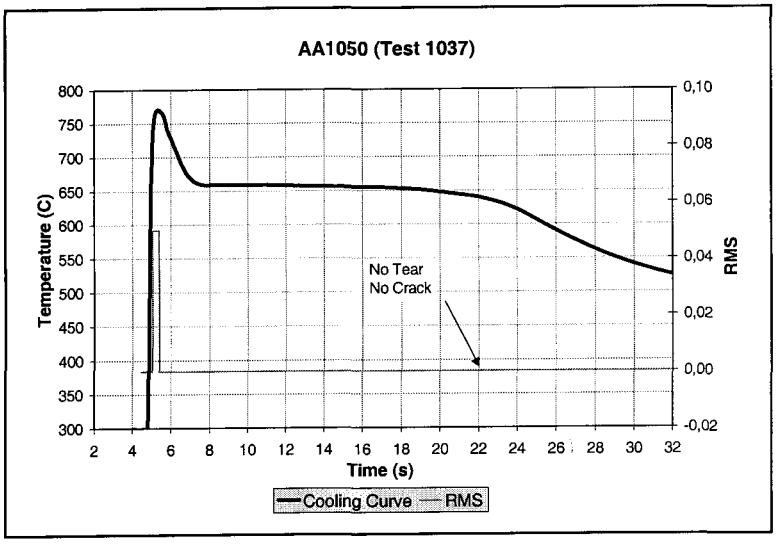
AA1050 (Test 1037)
Temperature (C)
RMS
Time (s)
No Tear
No Crack
Cooling Curve
RMS

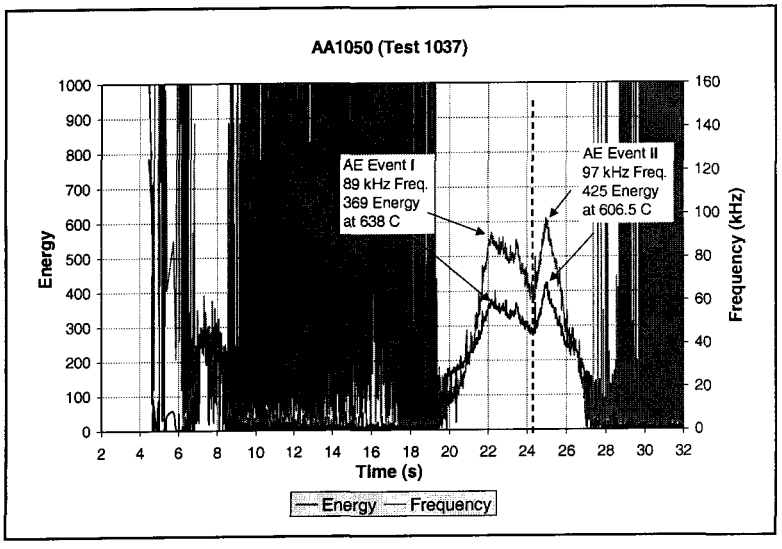
AA1050 (Test 1037)
Energy
Frequency (kHz)
Time (s)
AE Event I
89 kHz Freq.
369 Energy
at 638 C
AE Event II
97 kHz Freq.
425 Energy
at 606.5 C
Energy
Frequency